

# Advances in Rehabilitation and Assistive Robots for Restoring Limb Function in Persons with Movement Disorders

Guest Editors: Fan Gao, Guanglin Li, Huapeng Wu, Qining Wang, Jie Liu, and Justin Keogh





---

**Advances in Rehabilitation and  
Assistive Robots for  
Restoring Limb Function in  
Persons with Movement Disorders**

Applied Bionics and Biomechanics

---

**Advances in Rehabilitation and  
Assistive Robots for  
Restoring Limb Function in  
Persons with Movement Disorders**

Guest Editors: Fan Gao, Guanglin Li, Huapeng Wu,  
Qining Wang, Jie Liu, and Justin Keogh



---

Copyright © 2016 Hindawi Publishing Corporation. All rights reserved.

This is a special issue published in “Applied Bionics and Biomechanics.” All articles are open access articles distributed under the Creative Commons Attribution License, which permits unrestricted use, distribution, and reproduction in any medium, provided the original work is properly cited.

## Editor-in-Chief

Rene V. Mayorga, University of Regina, Canada

## Editorial Board

Saverio Affatato, Italy  
Seungik Baek, USA  
Lucia Beccai, Italy  
Sabine F. Bensamoun, France  
Ulrike Böer, Germany  
Andrea Cereatti, Italy  
Young-Hui Chang, USA  
Laurence Cheze, France  
Christian Cipriani, Italy  
Jose L. Contreras-Vidal, USA  
Marco Controzzi, Italy  
Ugo Della Croce, Italy  
Agnès Drochon, France  
Alicia El Haj, UK  
Fabio Esposito, Italy  
Toshio Fukuda, Japan  
Mark D. Geil, USA  
Ángel Gil-Agudo, Spain

Philippe Gorce, France  
Luis Gracia, Spain  
Eugenio Guglielmelli, Italy  
E. M. Gutierrez-Farewik, Sweden  
Kozaburo Hayashi, Japan  
Hiroaki Hobara, Japan  
Serkan Inceoglu, USA  
Hoon Eui Jeong, Republic of Korea  
Zhongmin Jin, China  
Kiros Karamanidis, Germany  
Justin Keogh, Australia  
Jan Harm Koolstra, Netherlands  
Thibault Lemaire, France  
Le Ping Li, Canada  
Francisco Lopez-Valdes, Spain  
Andrea Marinozzi, Italy  
Craig P. McGowan, USA  
Kenneth Meijer, Netherlands

Carlo Menon, Canada  
Jose Merodio, Spain  
Joseph Mizrahi, Israel  
Juan C. Moreno, Spain  
Estefanía Peña, Spain  
Bernardo Requena, Spain  
Hossein Rouhani, Canada  
Simo Saarakkala, Finland  
Jean Slawinski, France  
Hanno Steinke, Germany  
Fong-Chin Su, Taiwan  
Wei Tan, USA  
Amir A. Zadpoor, Netherlands  
Stefano Zaffagnini, Italy  
Li-Qun Zhang, USA  
Yanzhong Zhang, China  
Nigel Zheng, USA

# Contents

---

**Advances in Rehabilitation and Assistive Robots for Restoring Limb Function in Persons with Movement Disorders**

Fan Gao, Guanglin Li, Huapeng Wu, Qining Wang, Jie Liu, and Justin Keogh

Volume 2016, Article ID 3864728, 2 pages

**SEFRE: Semiexoskeleton Rehabilitation System**

Winai Chonnaparamutt and Witsarut Supsi

Volume 2016, Article ID 8306765, 12 pages

**Design of a Reconfigurable Robotic System for Flexoextension Fitted to Hand Fingers Size**

J. Felipe Aguilar-Pereyra and Eduardo Castillo-Castaneda

Volume 2016, Article ID 1712831, 10 pages

**Optical Enhancement of Exoskeleton-Based Estimation of Glenohumeral Angles**

Camilo Cortés, Luis Unzueta, Ana de los Reyes-Guzmán, Oscar E. Ruiz, and Julián Flórez

Volume 2016, Article ID 5058171, 20 pages

**The Effect of Mechanical Vibration Stimulation of Perception Subthreshold on the Muscle Force and Muscle Reaction Time of Lower Leg**

Huigyun Kim, Kiyoun Kwak, and Dongwook Kim

Volume 2016, Article ID 8794363, 7 pages

**Robust Sliding Mode Control Based on GA Optimization and CMAC Compensation for Lower Limb Exoskeleton**

Yi Long, Zhi-jiang Du, Wei-dong Wang, and Wei Dong

Volume 2016, Article ID 5017381, 13 pages

**Kinematics and Mechanical Properties of Knees following Patellar Replacing and Patellar Retaining Total Knee Arthroplasty**

Rongying Huang, Yanqiang Liu, and Jun Zhu

Volume 2015, Article ID 391450, 10 pages

## Editorial

# Advances in Rehabilitation and Assistive Robots for Restoring Limb Function in Persons with Movement Disorders

Fan Gao,<sup>1</sup> Guanglin Li,<sup>2</sup> Huapeng Wu,<sup>3</sup> Qining Wang,<sup>4</sup> Jie Liu,<sup>5</sup> and Justin Keogh<sup>6</sup>

<sup>1</sup>Department of Health Care Sciences, UT Southwestern Medical Center at Dallas, Dallas, TX 75390, USA

<sup>2</sup>Research Center for Neural Engineering, The Institute of Biomedical and Health Engineering, Shenzhen Institutes of Advanced Technology, Shenzhen 518055, China

<sup>3</sup>School of Energy Systems, Lappeenranta University of Technology, 53851 Lappeenranta, Finland

<sup>4</sup>The Robotics Research Group, College of Engineering, Peking University, Beijing 100871, China

<sup>5</sup>The Sensory Motor Performance Program, Rehabilitation Institute of Chicago, Chicago, IL 60611, USA

<sup>6</sup>Faculty of Health Sciences and Medicine, Bond University, Robina, QLD 4226, Australia

Correspondence should be addressed to Fan Gao; fan.gao@utsouthwestern.edu

Received 3 July 2016; Accepted 3 July 2016

Copyright © 2016 Fan Gao et al. This is an open access article distributed under the Creative Commons Attribution License, which permits unrestricted use, distribution, and reproduction in any medium, provided the original work is properly cited.

People with movement disorders are plagued with debilitating conditions, which significantly degrade their quality of life. Traditional rehabilitation typically involves intensive interaction between patients and therapists. While effective, traditional rehabilitation cannot keep abreast of the increasing patient population primarily attributed to a higher surviving rate after diseases and/or injuries. Furthermore, patients living in the rural areas have fairly limited access to rehabilitation services. In the past two decades, tremendous efforts have been put into developing rehabilitation and assistive robots to facilitate the rehabilitation training while relieving the physical involvement of therapists and/or lowering the related cost. Most notably, the rehabilitation and assistive robots have been significantly advanced with developments in actuators, sensors, microprocessors, and mobile software platforms. However, unlike traditional robotics, the intimate interaction between robot and human in rehabilitation robots indicates that the success is also closely related to a thorough understanding of the human neuromuscular aspects and human-machine interaction.

This special issue primarily aims to gather the latest achievements in rehabilitation robots, exoskeletons, and prostheses including the following topics: (a) development of rehabilitation robots, exoskeleton, and upper/lower limb prostheses driven by bionics; (b) functional evaluation of rehabilitation robots, exoskeleton, and upper/lower limb

prostheses with an emphasis on human movement biomechanics; (c) musculoskeletal modeling and simulation of human movements while wearing exoskeleton or prostheses; (d) noninvasive human-machine interface based on electromyography and/or electroencephalogram; (e) sensors for monitoring kinematics/kinetics, as well as biological signals in real time; (f) innovative actuators and control algorithms applied to rehabilitation robots, exoskeletons, and prostheses.

In this special issue, collective studies address the aforementioned key elements via both technical and biomechanical approaches. A reconfigurable robotic hand exoskeleton was proposed to meet the fast growing need in hand rehabilitation. A novel control algorithm integrating sliding model control with cerebellar model articulation controller neural network was implemented in lower limb exoskeleton to enhance the coordination between patient and exoskeleton. An upper limb exoskeleton was enhanced with integrated optical cameras to offer more accurate estimation of joint posture than traditional motion capture system. A hybrid upper limb rehabilitation system consisting of a shoulder-elbow-forearm exoskeleton and a robotic manipulator was validated and tested in the clinic. The characteristics of muscle-tendon stimulation such as perception threshold and vibration frequency significantly influenced the muscle forces as well as the reaction time. Patellar retention was found to be superior to patellar replacement in knee arthroplasty

via a comprehensive computer simulation. These collective studies, as part of the latest representative work, offered some new insights into the development and implementation of rehabilitation and assistive robots.

*Fan Gao*  
*Guanglin Li*  
*Huapeng Wu*  
*Qining Wang*  
*Jie Liu*  
*Justin Keogh*

## Research Article

# SEFRE: Semiexoskeleton Rehabilitation System

**Winai Chonnaramutt and Witsarut Supsi**

*National Electronics and Computer Technology Center, 112 Thailand Science Park, Pathum Thani 12120, Thailand*

Correspondence should be addressed to Winai Chonnaramutt; [winai.chonnaramutt@nectec.or.th](mailto:winai.chonnaramutt@nectec.or.th)

Received 15 January 2016; Revised 16 June 2016; Accepted 23 June 2016

Academic Editor: Guanglin Li

Copyright © 2016 W. Chonnaramutt and W. Supsi. This is an open access article distributed under the Creative Commons Attribution License, which permits unrestricted use, distribution, and reproduction in any medium, provided the original work is properly cited.

SEFRE (Shoulder-Elbow-Forearm Robotics Economic) rehabilitation system is presented in this paper. SEFRE Rehab System is composed of a robotic manipulator and an exoskeleton, so-called Forearm Supportive Mechanism (FSM). The controller of the system is developed as the Master PC consisting of five modules, that is, Intelligent Control (IC), Patient Communication (PC), Training with Game (TG), Progress Monitoring (PM), and Patient Supervision (PS). These modules support a patient to exercise with SEFRE in six modes, that is, Passive, Passive Stretching, Passive Guiding, Initiating Active, Active Assisted, and Active Resisted. To validate the advantages of the system, the preclinical trial was carried out at a national rehabilitation center. Here, the implement of the system and the preclinical results are presented as the verifications of SEFRE.

## 1. Introduction

Aging era is now. Based on Thai Aging Status Report, now the elders are around 12% of Thai population, and the percentage can be double in year 2030 [1]. More elderly require more caretakers to support their declined physical abilities, for example, low vision, hearing problem, and weakened muscles. Regarding these physical impairments, there is not only dysfunction from the aging phenomena, but also the disability that is caused by chronic diseases or an accident which must be concerned. In most cases, unusable limbs might be a result for all.

An impaired ability plagues their daily life. Thus relieving any of those impairments is always a great help for them. In general, recovering functions of limbs are practicable. Therefore we focus our research on the rehabilitation of arm and leg. Since recently there are an inadequate number of caretakers, so we believe that employing robotic systems in the rehabilitation process is a must.

Robotics enhances a simple device to be the super power tool. Extra enrichments include repeatability, high precision, and customizable movement. A number of medical and rehabilitation robotic systems have been on trial, while some of them are accepted in a certain level [2–5].

On one hand, numerous robotic rehabilitation systems have been developed around the globe as some examples are listed in Table 1. Many more existing systems have been also collected by Maciejasz et al. [6]. On the other hand, putting one on the market might be burdensome due to several factors, for example, overlarge size and weight or less benefit-to-cost ratio. Another burden is the complication of utilizing the device by a patient or a caretaker. Also, the cost of the systems and services put them too far to be reached.

Thus a device that is bearable in price and competent in features is needed to expand the deployment of robotics in the rehabilitation process. Setting this as our motto, WEFRE (Wrist-Elbow-Forearm Robotic Economic) Rehab System was firstly developed. This system is aimed at being employed as a household tool [7]. Successively, SEFRE (Shoulder-Elbow-Forearm Robotics Economic) Rehab System has been developed as an innovative machine for providing the rehabilitation service in a hospital [8]. SEFRE is designed to let everybody earn the benefits from the system, for example, a patient who has an impaired arm or a healthy person with a problem of muscle deficiency. In this paper, the development of SEFRE is thoroughly explained in Section 2. Then, Section 3 presents the preclinical trial of the system and is followed by the conclusion in Section 4.

TABLE I: Examples of robotic rehabilitation.

Reference	Target	Key concept
Lum et al. [9]	Hand	A rehabilitator in bimanual lifting
Chiri et al. [10]	Hand	A novel wearable multiphalanges device
Mao and Agrawal [11]	Hand	A cable driven arm exoskeleton
Takahashi et al. [12]	Wrist	Robotic device for hand motor therapy
Krebs et al. [13]	Wrist	A robot for wrist rehabilitation
Zhang et al. [14]	Elbow	A curved pneumatic muscle based exoskeleton
Wiegand et al. [15]	Elbow	A lightweight, portable, and active orthosis
O'Malley et al. [16]	Wrist & forearm	An exoskeleton rehabilitation robot
Oblak et al. [17]	Wrist & forearm	A universal haptic drive (UHD)
Hesse et al. [18]	Elbow & wrist	A robotic arm for bilateral training
Perry et al. [19]	Upper limb	A cable-actuated dexterous powered arm exoskeleton
Howard et al. [20]	Upper limb	A modular 2D planar manipulandum
Lam et al. [21]	Upper limb	A haptic device with postural sensors

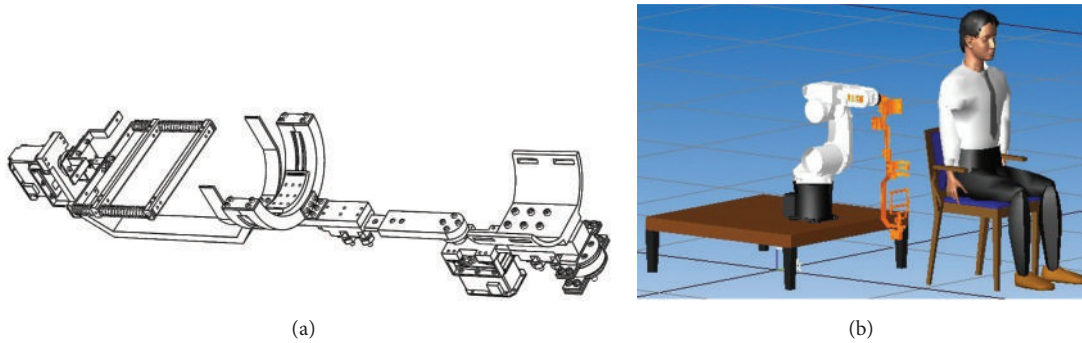


FIGURE 1: The first prototype of FMS (a) and the configuration of SEFRE Rehab System with a user (b).

## 2. SEFRE Rehab System

SEFRE Rehab System is created as a robotic rehabilitation system for all and sundry. The system is composed of three key components: a Shoulder-Elbow-Forearm Rehabilitating Mechanism, an Intelligent Controller, and a Friendly Graphic User Interface. To expedite the development process, a small industrial robot (KUKA KR5 sixx850) is used for motioning shoulder joint. Then a novel exoskeleton so-called “Forearm Supportive Mechanism (FSM)” is integrated to the system. FSM is responsible for moving elbow and forearm. This section provides the understanding of SEFRE in the details of FSM, rehabilitation protocol, control scheme and implementation, and games. (Details of control design in this section was presented at ECTI 2013, Thailand [8].)

**2.1. FSM.** While the main task of KUKA is to restore the shoulder motions, FSM is deployed as elbow-forearm trainer. FSM has been created as an independent module that can either work on its own or be controlled by other systems. The control program of FSM thus has been developed separately from the main controller, called “sFSM” (Section 2.4.3). FSM has been designed as a lightweight mechanism equipping with a maximum raising power to motion 4 kg of load. To simplify the system, two on-the-shelf servomotors

(Dynamixel EX-106+) were integrated to provide the movements of elbow and forearm.

Since FSM must be attached to the patient arm, several criteria need to be considered. These include, for examples, form and material causing no pain or irritation, weight being light to minimize an additional payload to KUKA, and the mechanism suiting for both left and right arms.

As a result, an exoskeleton is a desired form of FSM. This leads SEFRE Rehab System to be a semiexoskeleton robotic rehabilitation system. The first prototype of FSM is shown in Figure 1(a).

After integrating FSM to the robotic manipulator, SEFRE Rehab System is ready to provide an arm therapy to the patient. Figure 1(b) shows the system configuration when a patient is positioned in front of SEFRE Rehab System.

**2.2. Rehabilitation Protocol.** Since we were born, our upper limbs are crucial parts for manipulating things all day and night. Dispossessing the ability to move an arm freely is alike of having no arm. Thus one who loses the limb functions needs to reinstate the features. There are several levels of arm disability based on the residue muscle strength. SEFRE is designed to service the patient in any level of muscle weakness. The system also provides the exercise in two types: the individual joint exercise that let the patient to rehabilitate

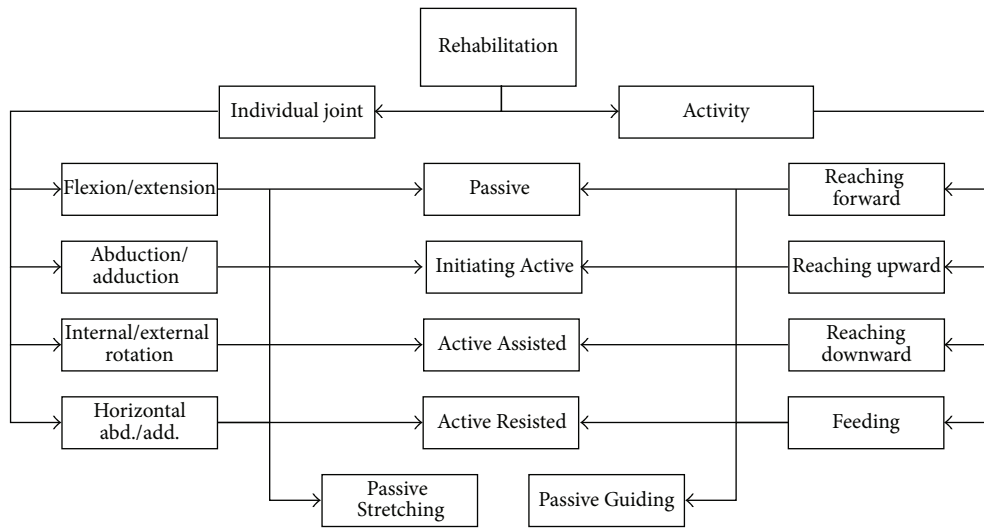


FIGURE 2: Rehabilitation protocol.

any dysfunction joint, that is, shoulder, elbow, or forearm, separately one by one, and the combined joints exercise, that is, Functional Activity Rehabilitation, that allows the patient to move the arm in a pattern of an activity in a daily life. Figure 2 presents the complete rehabilitation protocol of SEFRE Rehab System.

In the individual joint exercise, five therapy modes are provided based on each Muscle Strength Level (MSL).

**2.2.1. Passive (P).** Passive mode provides complete support to produce a joint motion of the target joint within the selected range of motion (ROM). The movement is carried out by SEFRE without any effort from the patient.

This mode is used for the patient with MSL 0 who does not have any residue muscle strength, that is, any patient who completely lost the muscle strength by a disease or an accident.

**2.2.2. Initiating Active (IA).** In this mode, a joint motion must be initiated by an acting force from the patient; then the motion is carried out by SEFRE as in Passive mode. This is a motivation mode that encourages the patient to try to use the regain muscle force.

This mode is used for the patient with MSL 1-2 who begins to recover some muscle strength. This could be a next step of rehabilitation process after the patient did exercises of the Passive mode in a period of time.

**2.2.3. Active Assisted (AA).** The AA mode provides for a patient who can insert a target guiding force to the system in some period of time. After the guiding force is less than the target level, SEFRE continues the motion as in Passive mode.

This mode is used for the patient who recovers and reaches the muscle strength in level 3 who wishes to train oneself to gain more and more strength.

**2.2.4. Active Resisted (AR).** This mode is similar to AA except that SEFRE only moves when the guiding force is more than or equal to the target level. This is a weight-training for the patient who almost completely recovers oneself.

This mode is used for the patients with MSL 4-5 who has high level of muscle strength. The patient who practices in this mode has ability to do the daily activities almost similar to a healthy person.

**2.2.5. Passive Stretching (PS).** This is a special mode that is available only for the individual joint exercise. In this mode, a joint motion is carried out by SEFRE as in Passive mode. The additional step is a pause for a short period of time at either end of the desired path. This mode let ROM of the joint be increased by stretching the joint at either end.

This mode is used for the patients with MSL 0-5 who has a spastic problem.

**2.2.6. Passive Guiding (PG).** This is a special mode that is available only for the functional activity exercise. For the functional activity option, the patient can exercise based on a typical arm movement, for example, reaching forward or feeding oneself. Four first therapy modes are provided the same as in the previous exercise type, that is, P, IA, AA, and AR. And in PG mode, a desired moving path is defined by a doctor or a caretaker, that is, a special reaching pattern; then this new customized path can be added for practicing in Passive mode.

This mode is used for the patient with MSL 0 who does not have any residue muscle strength who requires additional special movement paths.

**2.3. Control Scheme.** SEFRE is targeted as an intelligent device that any caretaker or even patients themselves can use the tool enjoyably with no sweat. A number of key components thus have been evolved: Intelligent Control System providing effective rehabilitation to all, Friendly GUI and

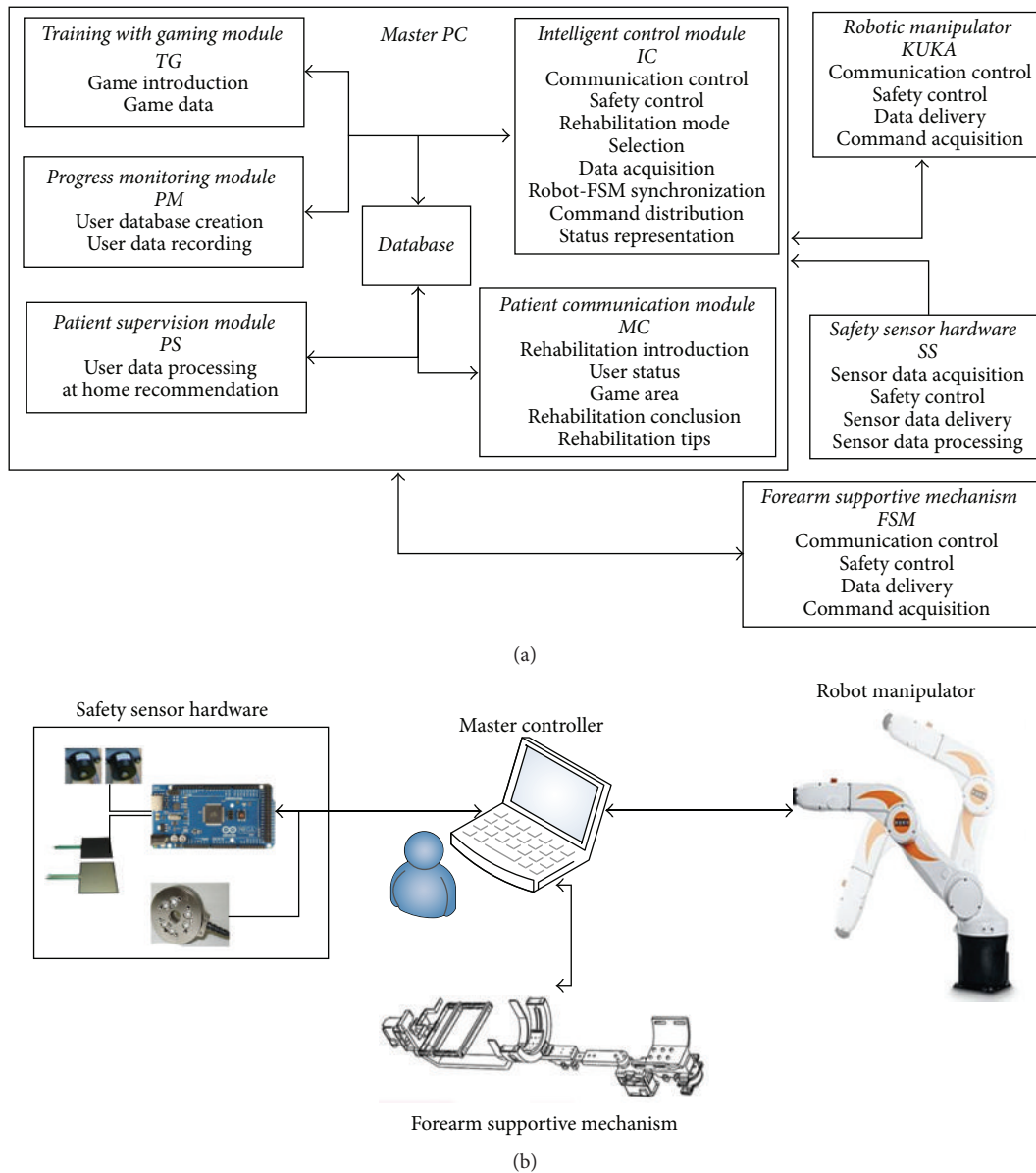


FIGURE 3: Overview of control system for SEFRE Rehab System: (a) scheme and (b) layout.

Games pleasing and entertaining the patients (Section 2.5), and Database Modules collecting and providing the fruitful data for the doctors and therapists. The overview of control system is shown in Figure 3(a).

The control system is divided into four modules: Master PC, Robot Manipulator (KUKA), Safety Sensor Hardware (SS), and FSM (Figure 3). As defined by its name, Master PC is the primary unit to administer the activities of the rest, especially keeping an eye on SS. SS module is the Interpol of error monitoring units in the system. These include User Ready signal, End-Effector Motion signal, Robot Range Motion signal, Enabling Switch signal, and Emergency Stop signal. Every fault signal is delivered to both the manipulator and Master PC to halt the system till the error is acknowledged, clarified, and solved. To conduct an exercise for the patient

based on rehabilitation protocol, the control scheme of the system is divided into high and low level controls. The high level control tasks are managed by Master PC, while the manipulator and FSM operate the low level control. All tasks are carried out after rehabilitating options are fulfilled.

**2.4. Control System Implementation.** The Master PC has been developed as an Intelligent Controller. The controller is decomposed into five submodules: Intelligent Control (IC), Patient Communication (PC), Training with Game (TG), Progress Monitoring (PM), and Patient Supervision (PS). Each has a key task as follows:

IC: the intelligent control unit,

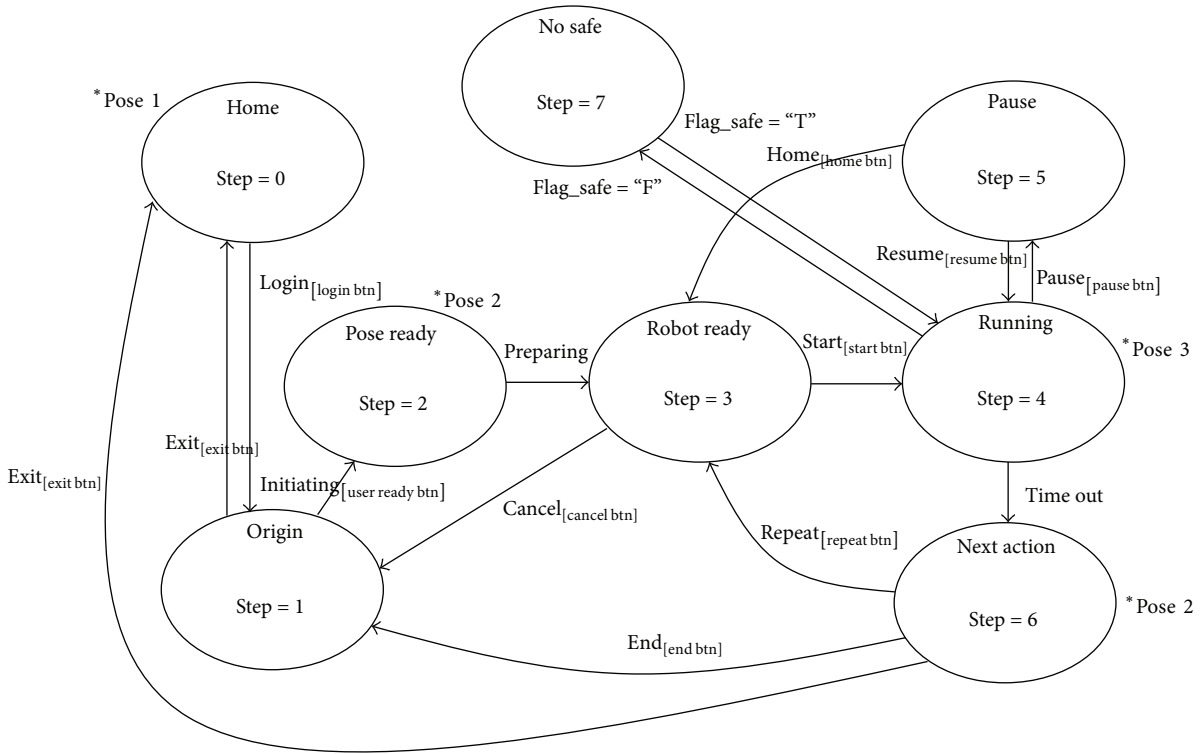


FIGURE 4: SEFRE state diagram.

PC: the interface unit between the patient and the system,

TG: the games management unit,

PM: the rehabilitation monitoring unit,

PS: the analyzing and supervising unit.

IC is responsible for generating commands based on the configured rehabilitation options. To conduct such a task, the communication protocol between IC and other modules, that is, KUKA, FSM, GUI, and Games, is executed as shown in Figure 4.

The protocol has four components: Robot Pose, Robot State, Changing State, and Clicked Button. To change the robot state when a button on the GUI is clicked, IC must send a corresponding signal to the robot after receiving the signal based on the Clicked Button. Consequently, this results in a new pose of the manipulator; that is, Robot Pose and Robot State are changed. This concept opens the door for assembling the other modes to the system by modifying IC only; neither KUKA nor FSM needs to be reprogrammed.

*2.4.1. Communication.* There are five communication paths to be managed by IC for conducting the rehabilitation process.

*The Manipulator Communication.* This protocol lets IC control the manipulator state as shown in Figure 4. The diagram shows eight major states of SEFRE for conducting the rehabilitation process. For examples, the Home state is the state of KUKA Home position, which allows the manipulator

to be safely relocated. Or the Pose Ready state is the state that lets the patient attach the arm to FSM. Or the patient is exercised based on the prior configuration when IC is in the Running state. Therefore, the Running state is a special one that varies the movement of the manipulator. To change the state, transition conditions are controlled by IC exclusively. For instance, after the patient has initiated the rehabilitation via GUI, IC sends an initiating signal to change the robot state from Origin state to Pose Ready state. Then the manipulator adjusts its position to allow the patient to attach the arm properly.

*sFSM Communication.* The communication between IC and FSM controller is similar to the manipulator communication as mentioned above. This allows IC to control KUKA and FSM to change their states simultaneously.

*Force Sensing Communication.* IC communicates with force sensing as essential inputs of the system. Force sensing communication aims to sense force of muscle strength at any joints in Active modes. A variety of force sensing in the system and the purposes of each sensor are deepened in the next topic.

*GUI and Game Communication.* GUI and Game (GG) module is responsible for interacting with the patient in attractive and friendly way. Even though GG seemingly lets the patient give a command directly to the system, the module is not able to understand and execute the patient desire. The information is forwarded to IC for identifying the request and executing the inquiry in an effective way. Also, IC transfers the position

of the manipulator back to GG for maneuvering an animation in the game.

*Database Communication.* IC transfers all needed practical data to be recorded in database through Database communication.

*2.4.2. Safety Control.* IC inspects safety of the system in different patterns based on the state in Figure 4. This task is done by considering signal values from several sensors such as an emergency stop, load cells, or limit switches. For examples, before the rehabilitation begins, IC checks the limit switches whether the patient arm is positioned properly and consistent with the configured side. Or before terminating the rehabilitation process, IC rechecks the limit switches whether the arm has already been detached from FSM. Furthermore, force values from the sensors are determined by IC to judge whether muscle strength exceeding the safety level.

*2.4.3. sFSM.* sFSM is an autonomous controller to control only FSM module, which is created separately from IC. Two servomotors that are deployed for FSM have two operation modes. Both are joint mode and wheel mode, which are used for controlling motor position and velocity, respectively. Due to mechanical design of FSM, one motor is operated in wheel mode, which requires an additional control algorithm. The algorithm composed of a round-counting function as an encoder and PID (Proportional-Integral-Derivative) control function. This customized algorithm supports sFSM to control the position of the joint while the motor is operated in wheel mode.

*2.4.4. Force Sensing.* Force Sensing is an essential part of the system because the sensors empower SEFRE to sense any effort from the patient. Each force sensor is selected based on its special properties that are consistent with the sensing task. Three types of force sensors, namely, six-axis force torque sensor, load cell, and Force Sensing Resistor (FSR), are integrated with SEFRE.

*Six-Axis Force Torque Sensor.* A 6-axis force/torque sensor (ATI mini45) is applied for monitoring the motions of shoulder, that is, by sensing the force magnitude and direction exerted by shoulder, which is the most complicated joint of the arm. A high-precision-high-cost sensor is deployed due to the complicated movement of shoulder in six degrees of freedom.

*Load Cell.* Two load cells are applied to measure the force magnitude and direction of elbow: flexion and extension.

*Force Sensing Resistor (FSR).* Two square FSRs are applied to measure the force magnitude and direction of forearm: supination and pronation.

As a remark, since forearm and elbow rotate around their own axis, so we simplified our system by using load cell and FSR instead of other complicated sensors.

*2.4.5. Synchronization.* In every state, IC plays a vital role in synchronizing between KUKA and FSM to make various desired motions, for example, reaching forward, to be a concurrent and natural motion. This section informs the synchronization process between both modules of each rehab mode.

According to the synchronization flowchart in Figure 5, IC appoints the velocities of the manipulator and FSM before outsets of their motions concurrently. The tempos are determined based on the exercise speed setting by the patient. Then IC signals to the manipulator and FSM to start moving. In each round, when both are nearly getting back to the beginning point, IC checks whether they reach to the position simultaneously. If so, IC continuously lets them onward, otherwise, the module that has arrived at the point first is paused to wait for the other by IC. After that IC considers the different time interval between two arrival times of KUKA and FSM. The difference is compared with the acceptable time interval, which is 3 seconds based on trial and error. If the different interval is less than or equal to the acceptable interval, IC allows them to move with the current velocities. Otherwise, IC tries to concurrent both modules by adjusting a new velocity for each before starting the next round. The process continues till the end of the session.

Synchronization can be classified based on two major modes: Passive and Active.

*Passive Mode.* IC synchronizes the manipulator and FSM together excluding force sensing communication for arm motions. The force sensing is incorporated only for the safety purpose.

*Active Mode.* IC synchronizes the manipulator and FSM based on the force sensing. So the patient needs to exert force to the system to do an exercise with a preprogrammed path.

*2.5. Games.* To serve various patients who have different conditions of muscle weakness, the exercises are also grouped into two modes: Passive and Active, as explained in the rehabilitation protocol. Therefore, games are designed deliberately to match the patient condition in each mode.

Games nowadays are mostly suitable for Active mode due to they must allow the players to experience the social interactions [22]. This means a player can move actors or objects in the games in any direction any time freely. But this type of game is definitely not suitable for the patient who has no muscle strength. Also, in Passive mode, the robot is moved automatically and disregards any interaction between the system and the patient. Our games thus are studiously designed to be consistent with the movement types and to let the patients enjoy the game in this mode.

*2.5.1. Passive Game Design for Rehabilitation.* The crucial factors that separate games in Passive mode from the others are the event conditions and scoring.

*Event Conditions Design of Passive Games.* In this game type, the game events occurred only when the joint reaches either end of ROM. For example, to exercise the elbow joint between

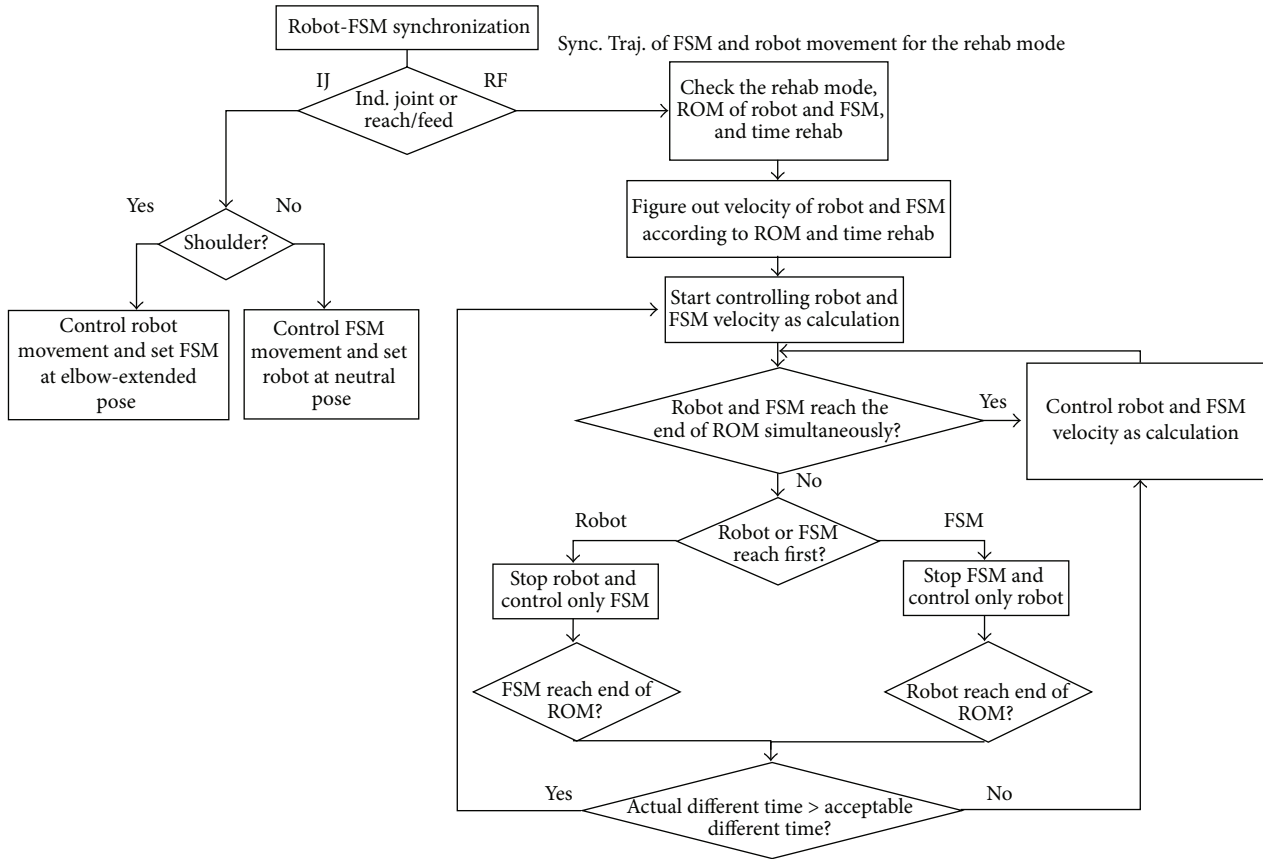


FIGURE 5: Synchronization procedures between IC, FSM, and KUKA.

extension of 0 degrees and flexion of 80 degrees, there is an key object following the elbow motion in the game. So an event in the game only happened if the object is located nearly or exactly at either the position of extension of 0 degrees or flexion of 80 degrees.

To play the transportation game in Figure 6(a), the patient must slide the pushcart to the left side to pick up the freight. Then the pushcart must be moved to the other side to deliver the freight. After reaching the right side, the freight randomly becomes a valuable or worthless object, which indicates the score for each round. There is no reward or obstacle that can be interacted with the patient during the motion between both sides.

For the fruit collection game in Figure 6(b), each fruit has a different score. A patient should move the basket to either side to collect a piece of desired fruit and to avoid useless stuff. When matching this game for Passive mode, patients have no chance to move freely to collect any desired fruit. Therefore, it is not appropriate for Passive mode undoubtedly.

*Scoring Design for Passive Games.* To hold attraction for the patients based on the random-value objects, the high score objects should appear less frequent than the lower ones. This strategy makes the games to be more challenging and enjoyable.

Also, there should not be any negative score because this condition might discourage the patients from playing the game.

*2.5.2. Game Design for Pre-Active Mode.* Pre-Active mode is an Active mode with an assigned path. This mode suits anyone who has enough muscle strength to motion a decayed arm along a preprogrammed path.

*Event Conditions Design of Pre-Active Games.* In Pre-Active games, the event conditions are similar to those in the Passive games. However, the main difference is an additional condition of acting force. To do the exercise in Pre-Active mode, the patient has to exert an amount of force to the system continuously (Section 2.2). So we can create an incentive for this mode. For example, an extra reward appeared near the end just only a few seconds before the key object reaches the point. This bait stimulates the patient to continuously make an effort to play with the system.

Pre-Active Transportation game is derived from a game in Passive mode. Due to the fact that patient may not notice the magnitude of acting force, it is necessary to add a force indicator in every Active game. The indicators, which represent the force magnitudes in colors,



FIGURE 6: Games for Passive mode.

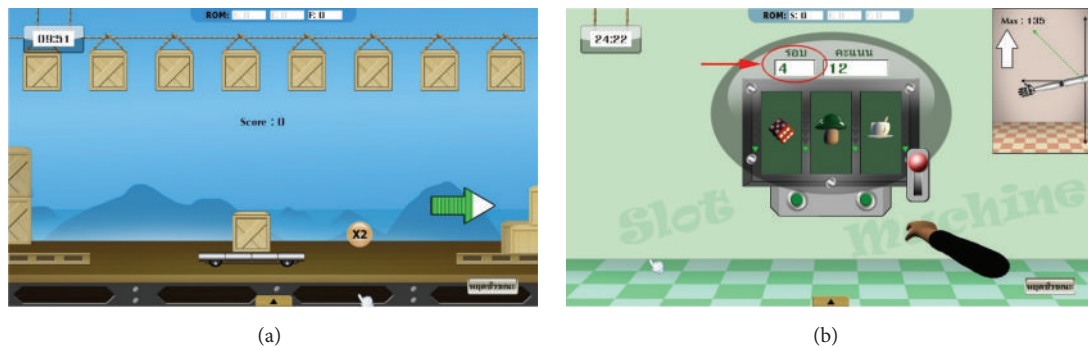


FIGURE 7: Games for Active mode.

are shown as arrows at both sides of the window in Figure 7(a).

*Scoring Design for Pre-Active Games.* Managing the score in Pre-Active games is almost identical to those games in Passive mode. Anyhow, the random-score method cannot be analyzed directly for verifying the performance of the player in the Pre-Active mode. Therefore scoring based on a number of movement cycles is implemented to evaluate the performance of each patient. The patient who has more power must be able to exercise more cycles. This can be the result of higher score. Thus the final score can imply how much effort the patient has done for each session.

For the Slot Machine Game in Figure 7(b), a number of movement cycles, which are shown in a box with a red circle, are used for calculating the score and analyzing the performance at the end of the game.

### 3. Preclinical Trial

To verify the advantages of SEFRE, we have carried out an intensive clinical trial at the national rehabilitation center of Thailand.

*3.1. Protocol.* The main objective of the preclinical trial is to validate the operation and the safety of the system through the rehabilitation in Passive mode. Since a small group of subjects can give a preliminary result to forward the work

[23–25]. Thus, the three subjects who aged 40–68 years were recruited to proceed with the following trial steps:

- (i) Before they began the trial and signed the contract, the details of the trial protocol were precisely explained. Then the personal information and medical background were recorded.
- (ii) During the 5-day trial, the subjects received the conventional therapy for two hours per session, one session per day. In each session, they must be rehabilitated by SEFRE for 15 minutes.
- (iii) In this trial, every subject was verified with two assessments, namely, the muscle tone assessment and Passive ROM (PROM) assessment. Both assessments were carried out two times: before the first day and after the fifth day.

Also, the subjects must fill in the questionnaire to evaluate the impression of SEFRE Rehab System. The actual trial period of all subjects for each day is shown in Figure 8.

*3.2. Movements.* SEFRE provides the exercise for the patients in several movements as shown in Figures 9–12. Nevertheless, to optimize the trial process, three activities were set as verifying motions: shoulder flexion-extension, elbow flexion-extension, and forearm pronation-supination.

*3.3. Trial Result.* Examples of subjects for the preclinical trial are shown in Figure 13. Based on the results of our intensive

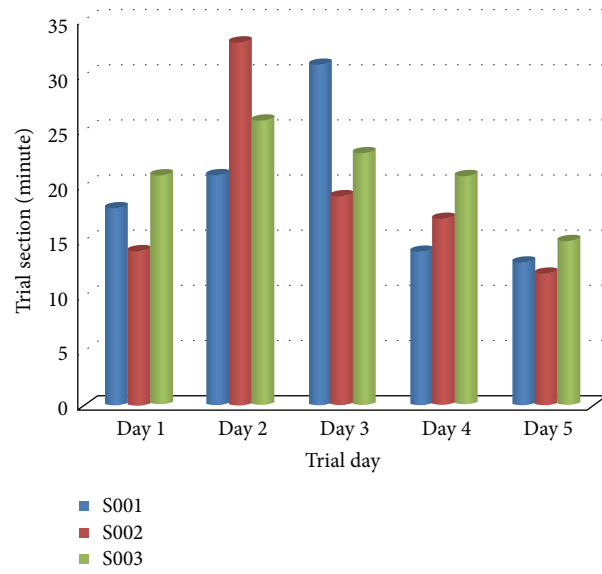


FIGURE 8: Trial period of all subjects on each day.

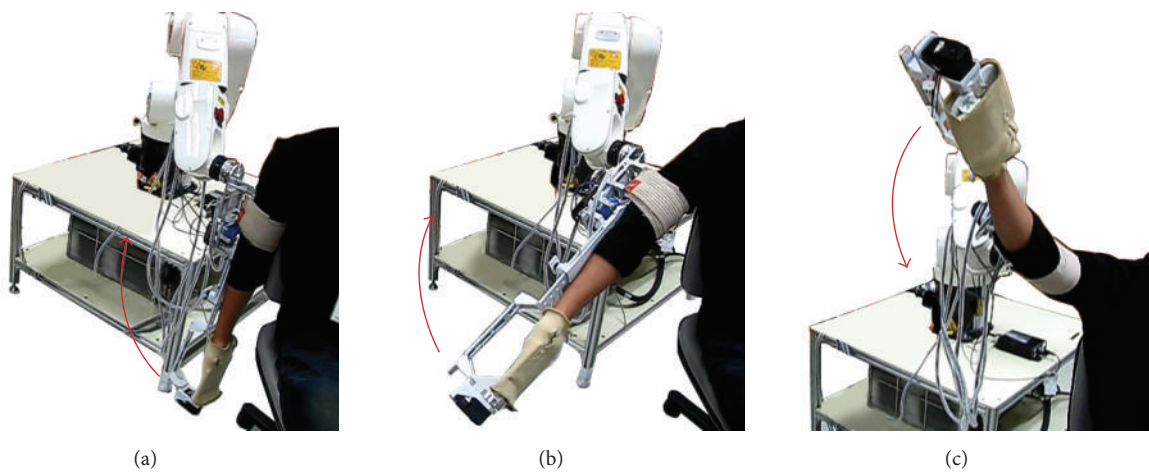


FIGURE 9: Example movements of SEFRE Rehab System: shoulder extension-flexion.

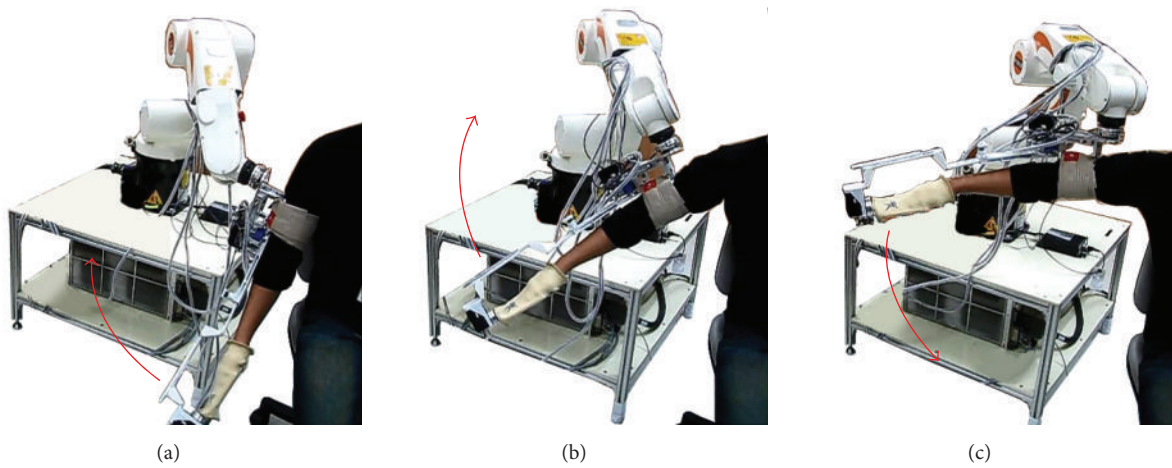


FIGURE 10: Example movements of SEFRE Rehab System: shoulder abduction-adduction.

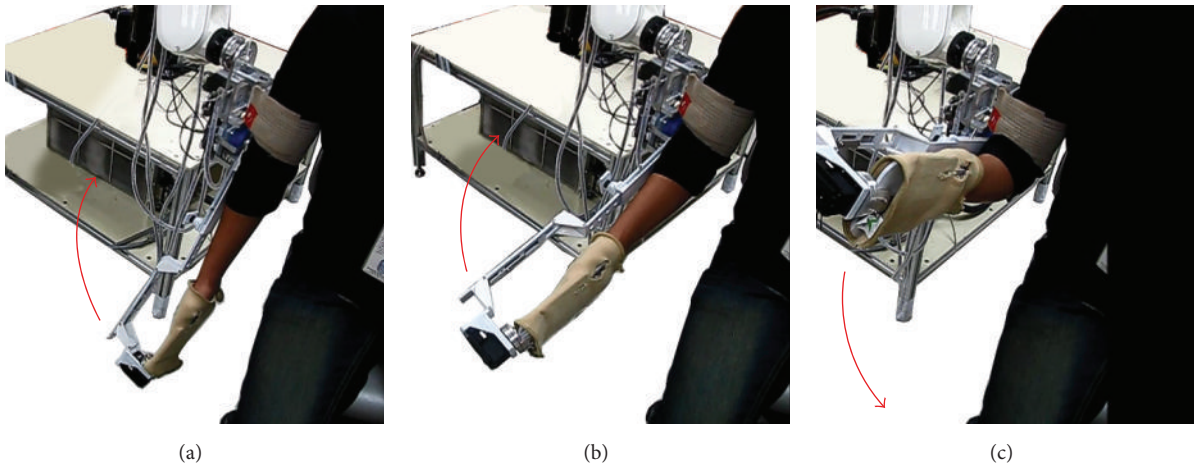


FIGURE 11: Example movements of SEFRE Rehab System: elbow extension-flexion.

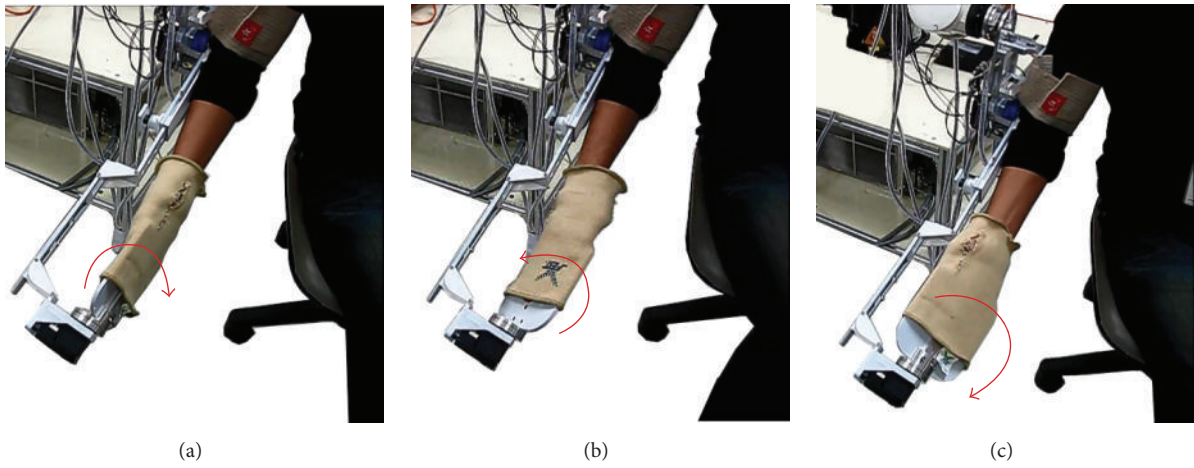


FIGURE 12: Example movements of SEFRE Rehab System: forearm pronation-supination.

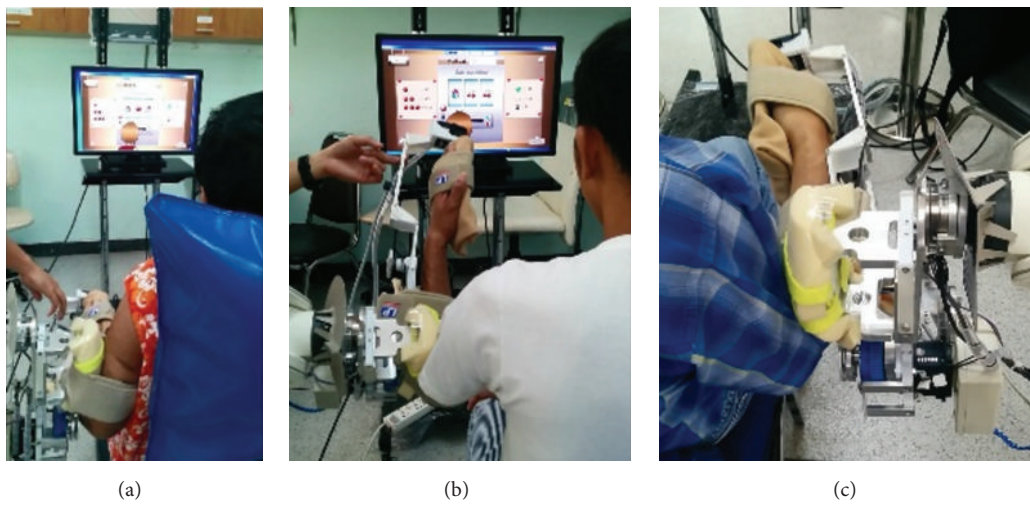


FIGURE 13: Examples of SEFRE clinical trial.

TABLE 2: SEFRE clinical trial result of 3 subjects: PROM.

Day	Shoulder E-F	Elbow E-F	Forearm P-S
1st	WNL	WNL	WNL
5th	WNL	WNL	WNL

TABLE 3: SEFRE clinical trial result of 3 subjects: muscle tone.

Day	S001	S002	S002
1st	1	1	1
5th	1	1	1

trial, we believe that the benefits of SEFRE have been verified. First of all, all subjects and relatives felt safe when they were rehabilitated by SEFRE. Also, results of the muscle tone and PROM assessments were evidences that SEFRE can retain the physical condition of the upper limb (Tables 2 and 3). Furthermore, the system allows the caretaker to spend the precious time on other patients without full attention to SEFRE.

Based on these results, the next phase is to certify the system in Active mode. Also, the number of subjects and the trial period must be extended. Moreover, to assure that the system can support and unite with the conventional therapy protocol, the subjects must be divided into two groups, that is, the control and experiment groups. Thus, the work we present here is still in an initiating step; nevertheless, we believe that our research must be a great achievement to rehabilitation domain when SEFRE is accomplished.

#### 4. Conclusion

SEFRE Rehab System is composed of a robotic manipulator and an exoskeleton, that is, FSM (Forearm Supportive Mechanism). The main controller of the system is the Master PC that consists of five modules, that is, Intelligent Control (IC), Patient Communication (PC), Training with Game (TG), Progress Monitoring (PM), and Patient Supervision (PS). Based on these modules, SEFRE Rehab System is able to provide six arm therapy modes: Passive (P), Passive Stretching (PS), Passive Guiding (PG), Initiating Active (IA), Active Assisted (AA), and Active Resisted (AR). These allow SEFRE to be the robotic rehabilitation system for everybody, for example, a patient without any residue muscle strength or a healthy person who has temporary muscle deficiency problem. To validate the advantages of the system, the preclinical trial was carried out by providing the rehabilitation in Passive mode for three subjects who aged 40–68 years. The results of this intensive trial, that is, three subjects were trialed for five sessions, show that all subjects and relatives felt safe when they were rehabilitated by SEFRE. Moreover, the muscle tone and PROM assessments verified the system for retaining the physical condition of the upper limb. Thus the next phase is to validate the system in Active mode, which we believe that this must be a great benefit to the rehabilitation field when the system is completed.

Furthermore, to achieve the motto of SEFRE, an affordable robotics rehabilitation system, a small industrial robot

with ATI mini45 module, must be replaced with a customized novel mechanism that lower the producing cost of the system. This is our next key milestone to complete SEFRE as the Shoulder-Elbow-Forearm Robotics Economic rehabilitation system.

#### Competing Interests

The authors declare that they have no competing interests.

#### Acknowledgments

The authors would like to thank Dr. Wasuwat Kitisomprayoongkul from The Thai Red Cross Rehabilitation Center, Dr. Daranee Suwapan from Sirindhorn National Medical Rehabilitation Center, and their OTs and PTs for allowing them to do an intensive preclinical test of SEFRE Rehab System there and Mr. Nassaree Benalie to support them to complete the trial.

#### References

- [1] Foundation of Thai Gerontology Research and Development Institute, *Thai Aging Status Report*, 2013.
- [2] H. Krebs, L. Dipietro, S. Levy-Tzedek et al., “A paradigm shift for rehabilitation robotics,” *IEEE Engineering in Medicine and Biology Magazine*, vol. 27, no. 4, pp. 61–70, 2008.
- [3] A. A. Timmermans, H. A. Seelen, R. D. Willmann, and H. Kingma, “Technology-assisted training of arm-hand skills in stroke: concepts on reacquisition of motor control and therapist guidelines for rehabilitation technology design,” *Journal of NeuroEngineering and Rehabilitation*, vol. 6, no. 1, article 1, 2009.
- [4] P. Langhorne, F. Coupar, and A. Pollock, “Motor recovery after stroke: a systematic review,” *The Lancet Neurology*, vol. 8, no. 8, pp. 741–754, 2009.
- [5] A. C. Lo, P. D. Guarino, L. G. Richards et al., “Robot-assisted therapy for long-term upper-limb impairment after stroke,” *The New England Journal of Medicine*, vol. 362, no. 19, pp. 1772–1783, 2010.
- [6] P. Maciejasz, J. Eschweiler, K. Gerlach-Hahn, A. Jansen-Troy, and S. Leonhardt, “A survey on robotic devices for upper limb rehabilitation,” *Journal of NeuroEngineering and Rehabilitation*, vol. 11, article 3, 2014.
- [7] W. Chonnaparamutt, E. Chanthabudsi, W. Rungkao, and W. Sapsri, “SEFRE rehab system,” in *Proceedings of the 6th International Convention on Rehabilitation Engineering and Assistive Technology (i-CREATE '12)*, Singapore, July 2012.
- [8] W. Chonnaparamutt, N. Benalie, and W. Sapsri, “Control concept of SEFRE Rehab System,” in *Proceedings of the 10th International Conference on Electrical Engineering/Electronics, Computer, Telecommunications and Information Technology (ECTI-CON '13)*, Krabi, Thailand, May 2013.
- [9] P. S. Lum, S. L. Lehman, and D. J. Reinkensmeyer, “The bimanual lifting rehabilitator: an adaptive machine for therapy of stroke patients,” *IEEE Transactions on Rehabilitation Engineering*, vol. 3, no. 2, pp. 166–174, 1995.
- [10] A. Chiri, N. Vitiello, F. Giovacchini, S. Roccella, F. Vecchi, and M. C. Carrozza, “Mechatronic design and characterization of the index finger module of a hand exoskeleton for post-stroke rehabilitation,” *IEEE/ASME Transactions on Mechatronics*, vol. 17, no. 5, pp. 884–894, 2012.

- [11] Y. Mao and S. K. Agrawal, "Design of a cable-driven arm exoskeleton (CAREX) for neural rehabilitation," *IEEE Transactions on Robotics*, vol. 28, no. 4, pp. 922–931, 2012.
- [12] C. D. Takahashi, L. Der-Yeghiaian, V. H. Le, and S. C. Cramer, "A robotic device for hand motor therapy after stroke," in *Proceedings of the IEEE 9th International Conference on Rehabilitation Robotics (ICORR '05)*, pp. 17–20, July 2005.
- [13] H. I. Krebs, B. T. Volpe, D. Williams et al., "Robot-aided neuro-rehabilitation: a robot for wrist rehabilitation," *IEEE Transactions on Neural Systems and Rehabilitation Engineering*, vol. 15, no. 3, pp. 327–335, 2007.
- [14] J.-F. Zhang, C.-J. Yang, Y. Chen, Y. Zhang, and Y.-M. Dong, "Modeling and control of a curved pneumatic muscle actuator for wearable elbow exoskeleton," *Mechatronics*, vol. 18, no. 8, pp. 448–457, 2008.
- [15] R. Wiegand, B. Schmitz, C. Pylatiuk, and S. Schulz, "Mechanical performance of actuators in an active orthosis for the upper extremities," *Journal of Robotics*, vol. 2011, Article ID 650415, 7 pages, 2011.
- [16] M. K. O'Malley, A. Sledd, A. Gupta, V. Patoglu, J. Huegel, and C. Bugar, "The RiceWrist: a distal upper extremity rehabilitation robot for stroke therapy," in *Proceedings of the 2006 ASME International Mechanical Engineering Congress and Exposition (IMECE '06)*, pp. 1437–1446, Chicago, Ill, USA, November 2006.
- [17] J. Oblak, I. Cikajlo, and Z. Matjačić, "Universal haptic drive: a robot for arm and wrist rehabilitation," *IEEE Transactions on Neural Systems and Rehabilitation Engineering*, vol. 18, no. 3, pp. 293–302, 2010.
- [18] S. Hesse, G. Schulte-Tigges, M. Konrad, A. Bardeleben, and C. Werner, "Robot-assisted arm trainer for the passive and active practice of bilateral forearm and wrist movements in hemiparetic subjects," *Archives of Physical Medicine and Rehabilitation*, vol. 84, no. 6, pp. 915–920, 2003.
- [19] J. C. Perry, J. Rosen, and S. Burns, "Upper-limb powered exoskeleton design," *IEEE/ASME Transactions on Mechatronics*, vol. 12, no. 4, pp. 408–417, 2007.
- [20] I. S. Howard, J. N. Ingram, and D. M. Wolpert, "A modular planar robotic manipulandum with end-point torque control," *Journal of Neuroscience Methods*, vol. 181, no. 2, pp. 199–211, 2009.
- [21] P. Lam, D. Hebert, J. Boger et al., "A haptic-robotic platform for upper-limb reaching stroke therapy: preliminary design and evaluation results," *Journal of NeuroEngineering and Rehabilitation*, vol. 5, article 15, 2008.
- [22] Y. A. W. De Kort and W. A. Ijsselstein, "People, places, and play: player experience in a socio-spatial context," *Computers in Entertainment*, vol. 6, no. 2, article 18, 2008.
- [23] S. Hesse, C. Werner, M. Pohl et al., "A mechanical arm trainer for the treatment of the severely affected arm after stroke: a single-blinded randomized trial in two centres," *Neurologie und Rehabilitation*, vol. 14, no. 6, pp. 307–314, 2008.
- [24] L. Masia, M. Casadio, P. Giannoni, G. Sandini, and P. Morasso, "Performance adaptive training control strategy for recovering wrist movements in stroke patients: a preliminary, feasibility study," *Journal of NeuroEngineering and Rehabilitation*, vol. 6, article 44, 2009.
- [25] P. Staubli, T. Nef, V. Klamroth-Marganska, and R. Riener, "Effects of intensive arm training with the rehabilitation robot ARMin II in chronic stroke patients: four single-cases," *Journal of NeuroEngineering and Rehabilitation*, vol. 6, no. 1, article 46, 2009.

## Research Article

# Design of a Reconfigurable Robotic System for Flexoextension Fitted to Hand Fingers Size

J. Felipe Aguilar-Pereyra<sup>1,2</sup> and Eduardo Castillo-Castaneda<sup>1</sup>

<sup>1</sup>Centro de Investigación en Ciencia Aplicada y Tecnología Avanzada, Instituto Politécnico Nacional, 76090 Querétaro, QRO, Mexico

<sup>2</sup>División de Tecnologías de Automatización e Información, Universidad Tecnológica de Querétaro, Querétaro, QRO, Mexico

Correspondence should be addressed to J. Felipe Aguilar-Pereyra; [faguilar@uteq.edu.mx](mailto:faguilar@uteq.edu.mx)

Received 15 January 2016; Revised 12 April 2016; Accepted 19 May 2016

Academic Editor: Jie Liu

Copyright © 2016 J. F. Aguilar-Pereyra and E. Castillo-Castaneda. This is an open access article distributed under the Creative Commons Attribution License, which permits unrestricted use, distribution, and reproduction in any medium, provided the original work is properly cited.

Due to the growing demand for assistance in rehabilitation therapies for hand movements, a robotic system is proposed to mobilize the hand fingers in flexion and extension exercises. The robotic system is composed by four, type slider-crank, mechanisms that have the ability to fit the user fingers length from the index to the little finger, through the adjustment of only one link for each mechanism. The trajectory developed by each mechanism corresponds to the natural flexoextension path of each finger. The amplitude of the rotations for metacarpophalangeal joint (MCP) and proximal interphalangeal joint (PIP) varies from 0 to 90° and the distal interphalangeal joint (DIP) varies from 0 to 60°; the joint rotations are coordinated naturally. The four R-RRT mechanisms orientation allows a 15° abduction movement for index, ring, and little fingers. The kinematic analysis of this mechanism was developed in order to assure that the displacement speed and smooth acceleration into the desired range of motion and the simulation results are presented. The reconfiguration of mechanisms covers about 95% of hand sizes of a group of Mexican adult population. Maximum trajectory tracking error is less than 3% in full range of movement and it can be compensated by the additional rotation of finger joints without injury to the user.

## 1. Introduction

The number of people with disabilities is increasing; thus, the demand of rehabilitation services is increasing too, due to the population growth and ageing, emerging chronic diseases, and the medical advances that preserve and extend life expectancy [1]. The World Health Organization reported “an estimated 10% of the world’s population, some 650 million people, experience some form of impairment or disability”; about 80% of people with disabilities live in developing countries. The majority are poor and experience difficulties in accessing basic health services, including rehabilitation services [1], an alternative to address this problem is the use of robotic systems in rehabilitation therapies. Robotic systems have already proven to enhance hand therapies through incorporating intensive and interactive exercises [2, 3]. Levanon confirms that “advanced technology can enrich treatment and can help patients who cannot come to the clinic regularly for treatment” [4]. “Disorders of the upper

extremities specifically limit the independence of affected subjects” [5] and impairment of hand affects significantly the execution of activities of daily living (ADL). There are injuries like fractures, sprains, and dislocations that cause temporary disability and they require mobilization exercises as part of rehabilitation therapy [6]. Fasoli et al. concludes that “robotic therapy may complement other treatment approaches by reducing motor impairment in persons with moderate to severe chronic impairments” [7]. On the other hand, Carey et al. concluded “that individuals with chronic stroke receiving intensive tracking training showed improved tracking accuracy and grasp and release function, and these improvements were accompanied by brain reorganization” [8]. Thus, Kitago et al. establish that there is a great need to develop new approaches to rehabilitation of the upper limb after stroke. Robotic therapy is a promising form of neurorehabilitation that can be delivered in higher doses than conventional therapy [9]. Additionally, rehabilitation robots also can be a platform for quantitative monitoring on

the recovery process in a rehabilitation program due to the standardized experimental setup and the high repeatability of motion tasks.

Different robotic devices for upper limb rehabilitation have been developed over the past two decades to provide hand motor therapy [5]. There are different design philosophies applied to robotic therapies, determining the degrees of freedom considered and technologies used. The objective is to develop a training platform that helps patients regain hand range of motion and the ability to grasp objects, ultimately allowing the impaired hand to partake in activities of daily living [10].

In the specific case of the fingers of the hand, exoskeletons, wearable orthosis and gloves, haptic interfaces, and end-effector-based devices have been developed and evaluated in order to facilitate the rehabilitation process [3, 5]. Exoskeletons are devices with a mechanical structure that mirrors the skeletal structure of the limb; that is, each segment of the limb associated with a joint movement is attached to the corresponding segment of the device. This design allows independent, concurrent, and precise control of movements in a few limb joints. It is, however, more complex than an end-effector-based device [5]. An example of this approach is the HEXORR, Hand EXOskeleton Rehabilitation Robot [10]. This device has been designed to provide full range of motion (ROM) for all of the hand's digits. The thumb actuator allows for variable thumb plane of motion to incorporate different degrees of extension-flexion and abduction-adduction. The finger four-bar linkage is driven by a direct current, brushless motor. The mechanisms of HEXORR only have one rotation axis for all the metacarpophalangeal joints for index to little fingers, but the rotation axes of the finger joints are not collinear. This device does not consider the distal interphalangeal joints of the fingers.

Glove devices are wearable, such as the robotic glove, which utilizes soft actuators consisting of molded elastomeric chambers with fiber reinforcements that induce specific bending, twisting, and extending trajectories under fluid pressurization. These soft actuators were mechanically programmed to match and support the range of motion of individual fingers [11]. These devices require a pneumatic or hydraulic facility, which is more complex than electric supply, especially for domestic use. The variation in hand size can be a complication for the use of these devices.

The haptic devices form another group of systems interacting with the user through the sense of touch and the mobilization of the limb. Haptic devices can be classified as either active or passive, depending on their type of actuator. An example of this approach is the "haptic knob" which is a two-degree-of-freedom robotic interface to train movements and force control of wrist and hand. The "haptic knob" uses an actuated parallelogram structure that presents two movable surfaces that are squeezed by the subject [12]. This device is oriented to perform many ADL such as grasping and manipulating objects.

The advantage of the end-effector-based systems is their simpler structure and thus less complicated control algorithms. However, it is difficult to isolate specific movements of a particular joint. The Rutgers Hand Master II is a force-feedback glove powered by pneumatic pistons positioned in

the palm of the hand and provides force feedback to the thumb, index, middle, and ring fingertips [13]. The fingertips develop a linear trajectory, whose amplitude depends on the length of the pneumatic pistons. Amadeo is a commercially available device that provides endpoint control of each of the hand digits along linear fixed trajectories electric motor [14]. In this case, the fingertips develop a linear trajectory too.

The design of a reconfigurable robotic system proposed, Ro-Share, has advantages with respect to the devices mentioned. First, it is designed so that each fingertip develops a natural flexoextension trajectory considering the joint coordination of each finger kinematic chain. Each of the fingers is free to move without forcing the rotation axis alignment of its joints. Only one actuator is necessary for each mechanism that mobilizes one finger. Each mechanism can be adjusted to the finger length by the length adjustment of its crank link. The variation of hand length can be up to 16% for a male and female adult from 18 to 90 years old specific population [15]. Hence, a robotic system to guide the fingertip of fingers, index, middle, ring, and little finger, in flexion and extension exercises is proposed, which must be able to fit finger sizes through only one link length adjustment.

## 2. Methods

*2.1. Kinematic Hand Model.* The general structure of the human hand can be divided into two sets for its kinematic analysis. The first set is composed of the bones of carpus and the second of the metacarpals link and the phalanges of the five digits [16, 17]. A realistic approach, useful for flexoextension exercises of the fingers in rehabilitation therapies, considers for the fingers from the index to the little finger a kinematic chain with 3 links, which are the phalanges, and 4 degrees of freedom (DOF). For the thumb, the kinematic chain has 3 links, the metacarpal (MC), 2 phalanges, and 5 DOF. The palm of the hand is considered a fixed base. In this approach, for the index finger to the little finger, the metacarpals (MC) represent the immobile base of each kinematic chain. This is complemented by the proximal phalange (PP), medial phalange (MP), and distal phalange (DP) as links, as shown in Figure 1. The metacarpophalangeal joint (MCP) has 2 DOF, and the interphalangeal joints, proximal (PIP) and distal (DIP), have only one DOF. P represents the fingertip, the mobile end of the kinematic chain. The joints of the thumb are the carpometacarpal (TCMC) with 2 DOF, the metacarpophalangeal (TMCP) with 2 DOF, and the proximal interphalangeal joint (PIP) with one DOF.

The Denavit-Hartenberg (D-H) convention is used to define each one of the four kinematic chains [18, 19]. Table 1 presents the D-H parameters of kinematic chains, where LPP, LMP, and LDP are the nominal lengths of the proximal, medial, and distal phalanges, respectively.

Equation (1) describes the position and orientation of the fingertip [11]:

$$Pk = {}_0^{-1}T(u_k) {}_4^0T(\theta_i) k = {}_0^{-1}T(u_k) {}_1^0T(\theta_{MCPabd}) \cdot k {}_2^1T(\theta_{MCPflex}) k {}_3^2T(\theta_{PIPflex}) k {}_4^3T(\theta_{DIPflex}) k, \quad (1)$$

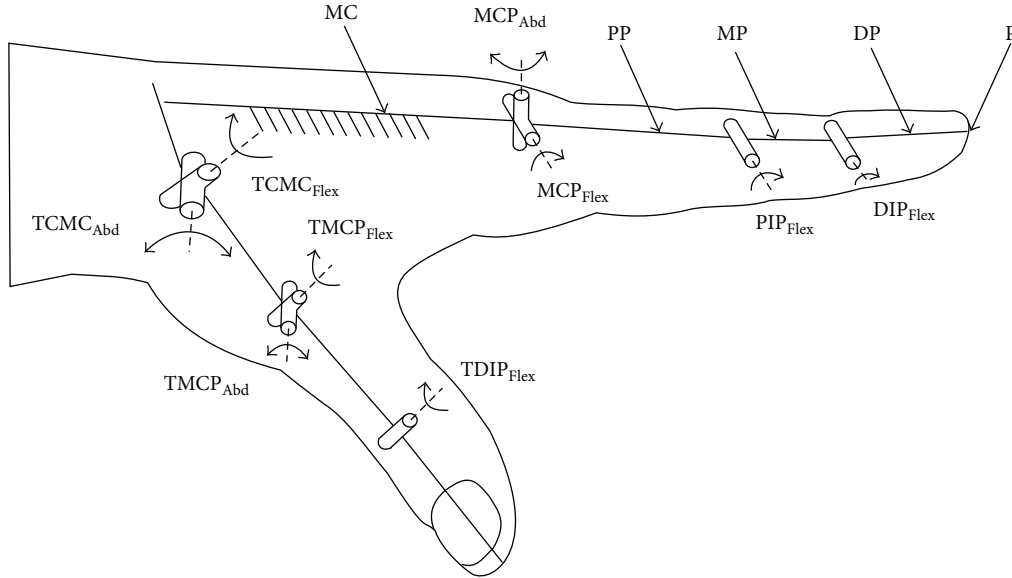


FIGURE 1: Kinematic model of hand with fixed metacarpal (except thumb).

TABLE 1: D-H parameters of kinematic chains corresponding to the index to little fingers, considering metacarpal links fixed.

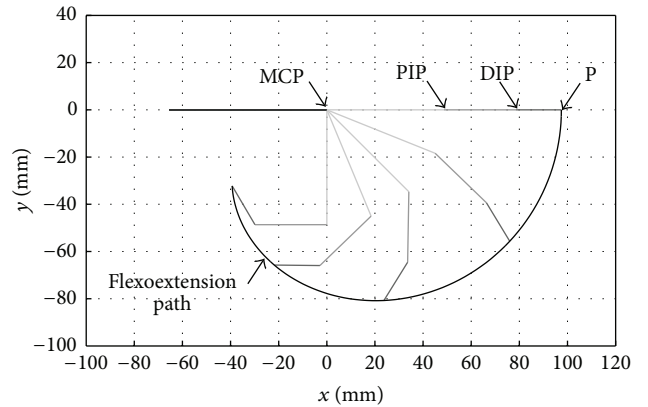
Joint	$\theta_i$	$d_i$	$a_i$	$\alpha_i$
1	$\theta_{MCP\ abd}$	0	0	$\pi/2$
2	$\theta_{MCP\ flex}$	0	LPP	0
3	$\theta_{PIP\ flex}$	0	LMP	0
4	$\theta_{DIP\ flex}$	0	LDP	0

TABLE 2: Angles of active movements of the joints of the fingers: index to little finger.

Finger\joint	$\theta_{MCP\ abd}$	$\theta_{MCP\ flex}$	$\theta_{PIP\ flex}$	$\theta_{DIP\ flex}$
Index	20–30°	90°	110°	80°–90°
Middle	20–30°	90°	110°	80°–90°
Ring	20–30°	90°	120°	80°–90°
Little	20–30°	90°	135°	90°

where  $P_k$  represents an array containing the position and orientation of the fingertip, and  $k$  is the indicator for the fingers: index = 2, medium = 3, ring = 4, and little finger = 5, since 1 is reserved for the thumb.  $T(u_k)$  represents the vector used to define the reference frame at the origin of the kinematic chain of each finger relative to a fixed frame of reference at the base of the hand.  $T(\theta_i)k$  are the homogeneous transformation matrices which define the geometric transformation between the origin of the kinematic chain of each finger and its tip. According to [16, 17], rotation of the finger joints is shown in Table 2. Figure 2 shows the path of flexoextension of the kinematic chain of the three phalanges of the middle finger. This path fingertip (P) is the initial requirement for movement of the flexoextensor mechanisms of the robotic system.

**2.2. Proposed R-RRT Mechanism.** The characteristics of simplicity, modularity, and low cost of construction and maintenance are desirable in devices for assistance in rehabilitation therapies [20]. The most important criterion is the patient's safety; therefore, the range of movement of flexoextensor mechanism R-RRT is mechanically limited to avoid finger hyperextension. Accuracy in the tracking of the flexoextension path is the second aspect of importance, since continuous and gentle movements are desired from the


 FIGURE 2: Flexoextension path of the kinematic chain of the three phalanges of middle finger ( $0^\circ \leq MCP \leq 90^\circ$ ,  $0^\circ \leq PIP \leq 90^\circ$ , and  $0^\circ \leq DIP \leq 60^\circ$ ).

beginning ( $Lim_{ext}$ ) to the end of the path ( $Lim_{flex}$ ). Therefore, the position and velocity of movements should be controlled. Exercises can start with movements of low amplitude and low speed and increase both amplitude and speed up to the full range of flexion and extension. Therapies must be always supervised by professional physiotherapists to avoid sudden movements that can cause pain or further damage to the

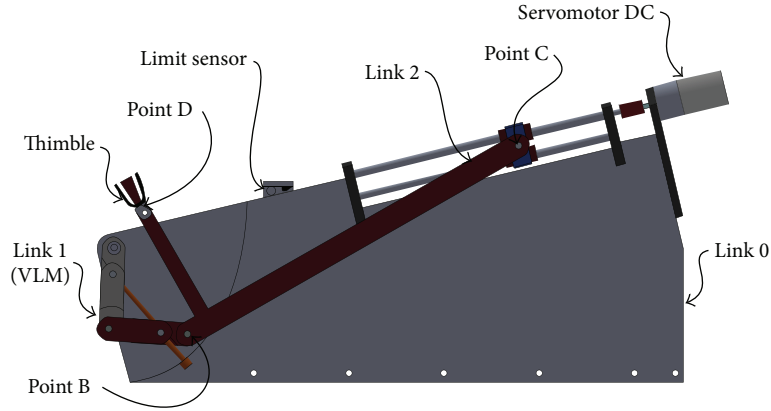


FIGURE 3: R-RRT mechanism of the middle finger.

patient. In response to the above requirements, the system is composed of four four-bar type crank-slide mechanisms (R-RRT) for the mobilization of the fingers from the index to the little finger.

Figure 3 shows the corresponding mechanism design for middle finger. The DC servomotor drives point C of the slide on a linear guide through the screw, foregoing causes semicircular movements of point B of the variable length crank (VLC). Finally, point D of the coupler link develops the flexoextension path. Point D is attached to the fingertip P through a thimble secured by adhesive tape for medical use. The thimble has an unactuated joint to connect itself with link 2 (coupler) at point D; it allows the free rotation of the thimble and the natural orientation of the distal phalanx. As an additional safety, a limit sensor detects when the mechanism reaches the positions of maximum flexion or extension, to indicate to an electronic controller these positions. The R-RRT, type slider-crank mechanism, is selected since the extension of the coupler link develops a very similar path presented in Figure 2. Each flexoextensor mechanism (R-RRT) develops the flexoextension path in the distal end of the extension of the coupler link (D), Figure 4(a).

The length of each finger defines the dimensions of the corresponding mechanism. The synthesis of flexoextensor mechanisms was performed from a trajectory generation method using 3 precision points based on the curves of the coupler link [21].

A major constraint is that the length of the extension of the coupling link,  $L_3$ , must be greater than the length of the crank,  $L_2$ , to avoid collisions between finger and mechanism. The lengths of link 2,  $L_2$ , and the extension of the coupler link,  $L_3$ , are defined by (2) and (3), respectively,

$$L_2 = L_1 * 6.21, \quad (2)$$

$$L_3 = L_1 * 1.2. \quad (3)$$

Due to the length of the crank handle that determines the range of movement on the  $x$ -axis, the path of flexoextension, Figure 2, was rotated the angle  $\alpha$ , Figure 5(a); after this, the rotated path was moved to point (0, 0) using a homogeneous transformation matrix H. Finally, the start and the end of

the path are aligned with the axis  $x$  and the position of the maximum flexion meets with point (0, 0), Figure 5(b).

The rotation angle is calculated with

$$\alpha = \tan^{-1} \left( \frac{y_{Fmax} - y_{Emax}}{x_{Fmax} - x_{Emax}} \right), \quad (4)$$

where  $x_{Fmax}$ ,  $y_{Fmax}$ ,  $x_{Emax}$ , and  $y_{Emax}$  are the coordinates of the maximum flexion position ( $Lim_{flex}$ ) and maximum extension position ( $Lim_{ext}$ ) of the natural flexoextension path in the axis  $x$  and  $y$ . Finally, the length of the crank link is calculated with

$$L_1 = \frac{(x_{EmaxRot} - x_{FmaxRot})}{2}, \quad (5)$$

where  $x_{FmaxRot}$  and  $x_{EmaxRot}$  are the coordinates on the axis  $x$  of the positions of maximum extension and maximum flexion of the natural flexoextension path rotated on the angle  $\alpha$ .

Once the mechanism has been synthesized, the orientation of the path is recovered by a rotation of the mechanism with the angle  $-\alpha$  (equal magnitude than  $\alpha$  but with opposite direction). Afterwards, an iterative numerical method to minimize the error path was later used [22].

**2.3. Reconfiguration of R-RRT Mechanism.** Each patient may have a different hand size, thus requiring the reconfiguration mechanism ability to adapt to flexoextension path. Therefore, a reconfiguration scheme to modify the path of point D of the coupler link is proposed in order to follow the path of flexoextension of the fingers for different sizes. For a group of Mexican population, the average hand size for adults between the ages of 18 and 90 is estimated at  $\mu = 175.62$  mm with a standard deviation of  $\sigma = 8,615$  mm [15]. If we consider a normal probability distribution, then, in the interval  $[\mu - 2\sigma, \mu + 2\sigma]$ , approximately 95% of the hand sizes for the Mexican population are understood. Therefore, it is estimated that hand size varies from 158.39 to 192.85 mm. The length of the crank link is half of straight length of the flexoextension rotated path on the  $x$ -axis. Then, changes in the length of the crank link can modify the path amplitude of point D of the mechanism. The design of a variable length crank link (VLC)

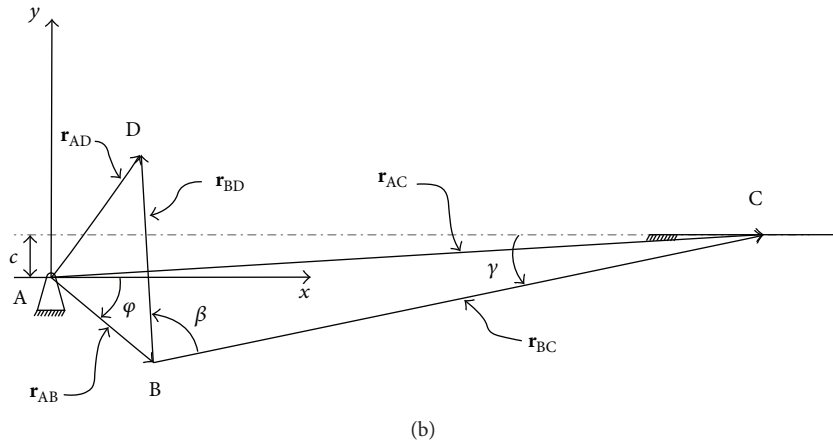
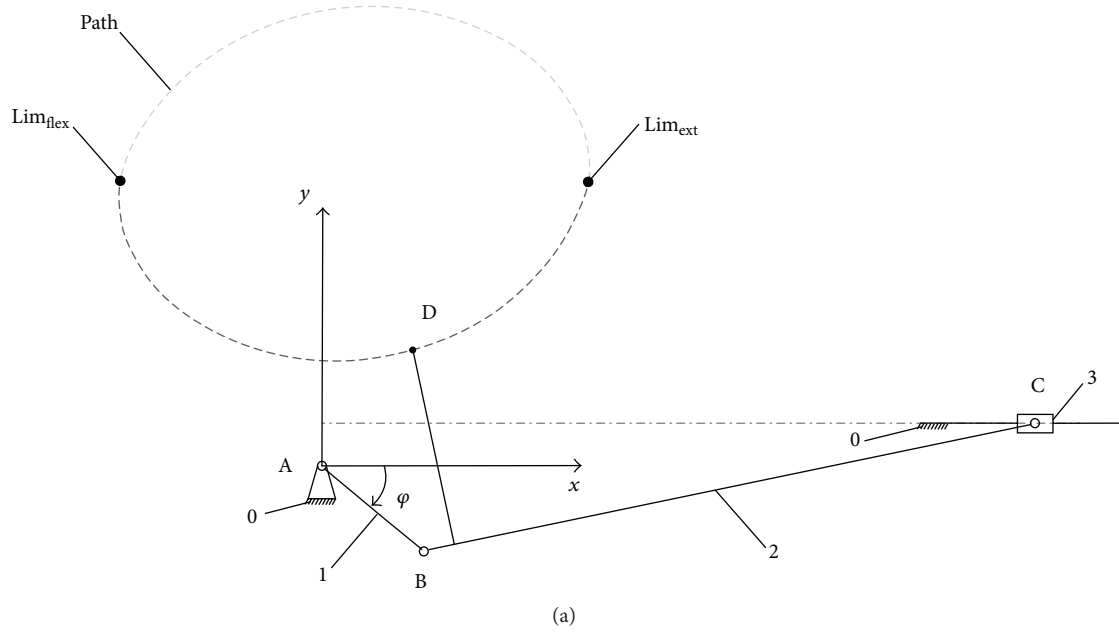


FIGURE 4: R-RRT mechanism: (a) scheme and (b) vector analysis.

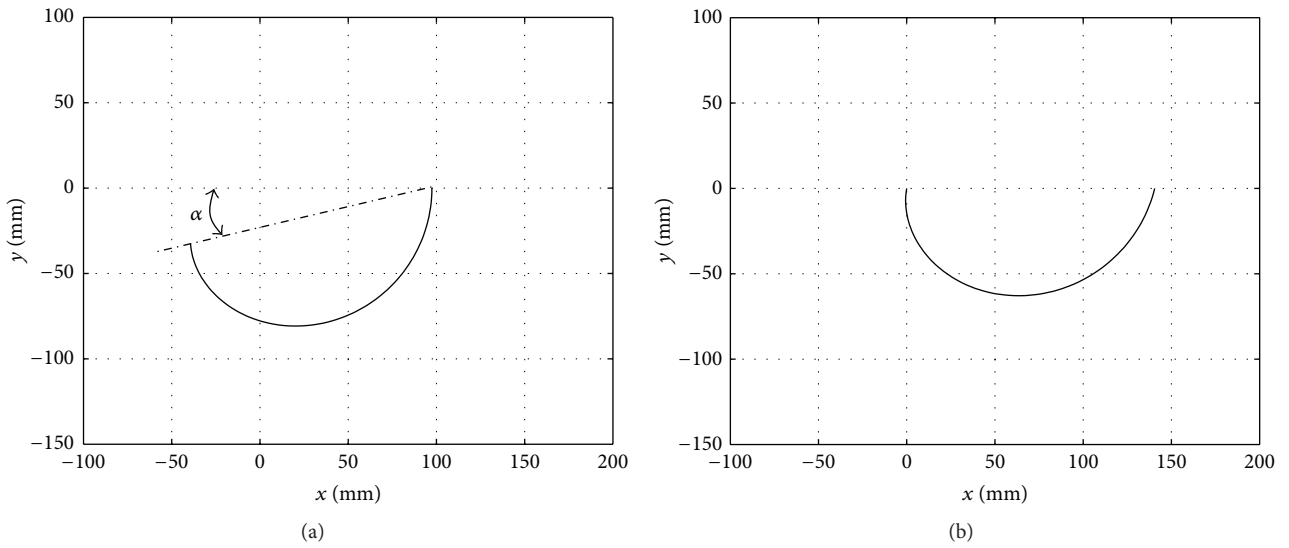


FIGURE 5: Flexoextension path: (a) rotation angle  $\alpha$  and (b) rotated path.

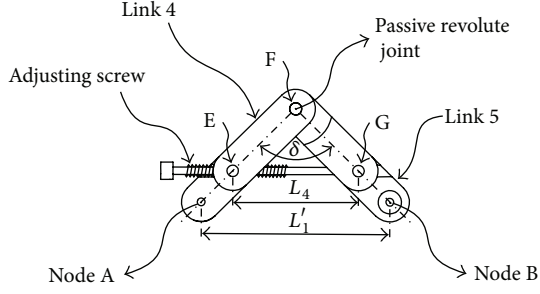


FIGURE 6: The variable length crank link (VLC).

is proposed in Figure 6, whose length  $L_1'$  between its external nodes A and B varies in proportion of length  $L_4$ . The VLC is composed of two links connected by a passive rotational joint, point F, and a screw whose end is attached to G point of link 5 through a ball joint, allowing only for rotation. The other point of contact between the screw and link 4 is achieved through a nut; so that when screw turns,  $L_4$  varies. Similar triangles formed by points EFG and AFB, Figure 6, have the angle  $\delta$ , which is defined by the law of cosines as

$$\delta = \cos^{-1} \left( \frac{L_4^2 + L_5^2 + L_6^2}{2 \cdot L_5 \cdot L_6} \right), \quad (6)$$

wherein  $L_5$  and  $L_6$  are the lengths of EF and FG lines, respectively, having the same length,  $L_5 = L_6$ .

The length  $L_1'$  is defined by

$$L_1' = \sqrt{(L_7^2 + L_8^2 - 2 \cdot L_7 \cdot L_8 \cdot \cos \delta)}, \quad (7)$$

wherein  $L_7$  and  $L_8$  are the lengths of AF and FB respectively, which have the same length,  $L_7 = L_8$ .

**2.4. Kinematic Analysis of R-RRT Mechanism.** In order to validate the monitoring path of flexoextension of the proposed mechanism, kinematic analysis of the synthesized mechanism is performed and the tracking error of the path is calculated. Vector loop method is used for position analysis [21]. A right-handed coordinate system is defined and a local reference frame  $x, y$  is located at point A of fixed link 0. Each mechanism has a point A, which is the point of rotation of the crank, link 1. Point B is in the joint that connects the crank link to the coupler, link 2; point B develops a circular constant radius equal to the crank's length. Point C, corresponding to the slide, moves on a linear axis parallel to the  $x$ -axis. Finally, point D, located in the extension of the coupler link, develops an elliptical path that, in the range of  $180^\circ \leq \theta \leq 360^\circ$ , is similar to the flexoextension path, Figure 2.

Vectors  $\mathbf{r}_{AB}$  and  $\mathbf{r}_{BC}$  correspond to links 1 and 2, respectively, Figure 4(b), so that their magnitudes are constant. Point C is defined by the  $\mathbf{r}_{AC}$  vector, whose magnitude varies according to angle  $\varphi$ , since it is the sum of vector  $\mathbf{r}_{AB}$  and  $\mathbf{r}_{BC}$ . The  $\mathbf{r}_{AC}$  vector has the following components:  $x_{AC}$  that is parallel to the sliding axis of the slide and  $y_{AC}$  which is constant and corresponds to the length of offset ( $c$ ) between the axis of the extended slide shaft and pivot of the link [21]. The most important point is D, because it performs the

desired path and is defined by  $\mathbf{r}_{AD}$  vector, which is the result of the sum of  $\mathbf{r}_{AB}$  and  $\mathbf{r}_{BD}$  vectors (8). The magnitude of  $\mathbf{r}_{BD}$  vector is constant, since it corresponds to the extension length of the coupler link; angle  $\beta$  is a constant value that determines the orientation according to  $\mathbf{r}_{BC}$  vector.

Position equation (8), velocity equation (9), and acceleration equation (10) of point D are calculated from the expressions:

$$\begin{aligned} \mathbf{r}_{AD} &= \mathbf{r}_{AB} + \mathbf{r}_{BD} = (x_{AB} + x_{BD})\hat{\mathbf{i}} + (y_{AB} + y_{BD})\hat{\mathbf{j}} \\ &= (L_1 \cos \varphi + L_3 \cos \psi)\hat{\mathbf{i}} + (L_1 \sin \varphi + L_3 \sin \psi)\hat{\mathbf{j}}, \end{aligned} \quad (8)$$

$$\begin{aligned} \mathbf{v}_{AD} &= \dot{\mathbf{r}}_{AD} = \dot{\mathbf{r}}_{AB} + \dot{\mathbf{r}}_{BD} = (\dot{x}_{AB} + \dot{x}_{BD})\hat{\mathbf{i}} + (\dot{y}_{AB} \\ &+ \dot{y}_{BD})\hat{\mathbf{j}} = -(L_1 \dot{\varphi} \sin \varphi + L_3 \dot{\psi} \sin \psi)\hat{\mathbf{i}} \\ &+ (L_1 \dot{\varphi} \cos \varphi + L_3 \dot{\psi} \cos \psi)\hat{\mathbf{j}}, \end{aligned} \quad (9)$$

$$\begin{aligned} \mathbf{a}_{AD} &= \ddot{\mathbf{r}}_{AD} = \ddot{\mathbf{r}}_{AB} + \ddot{\mathbf{r}}_{BD} = (\ddot{x}_{AB} + \ddot{x}_{BD})\hat{\mathbf{i}} + (\ddot{y}_{AB} \\ &+ \ddot{y}_{BD})\hat{\mathbf{j}} = (-L_1 \ddot{\varphi} \sin \varphi - L_1 \dot{\varphi}^2 \cos \varphi - L_3 \ddot{\psi} \sin \psi \\ &- L_3 \dot{\psi}^2 \cos \psi)\hat{\mathbf{i}} + (L_1 \ddot{\varphi} \cos \varphi - L_1 \dot{\varphi}^2 \sin \varphi \\ &+ L_3 \ddot{\psi} \cos \psi - L_3 \dot{\psi}^2 \sin \psi)\hat{\mathbf{j}}, \end{aligned} \quad (10)$$

where  $L_1$  is the length of segment AB,  $L_3$  is the length of segment BD, and  $\dot{\varphi}$  and  $\ddot{\varphi}$  are the angular velocity and acceleration, respectively.

### 3. Results

**3.1. Construction Parameters.** The reconfigurable robotic system for flexoextension is composed of four four-bar mechanisms and it is complemented with a variable height base on which the forearm and palm rest, Figure 7. Table 3 shows parameters of construction of four mechanisms corresponding to the index, middle, ring, and little fingers.

Figure 8 shows the behavior of the position, velocity, and acceleration of point D of the mechanism of the middle finger in the  $x$ - and  $y$ -axes. It is observed that all the curves are smooth and continuous in the range of the path from the maximum extension ( $\text{Lim}_{\text{ext}}$ ) up to the maximum finger bending ( $\text{Lim}_{\text{flex}}$ ).

Figure 9 illustrates the final work area of the flexoextensor reconfigurable mechanism for the case of the middle finger. The central path corresponds to the average hand size (175.62 mm) and external paths correspond to the minimum (158.39 mm) and maximum (192.85 mm) size of the Mexican adults between 18 and 90 [8]. The area between the latest two paths corresponds to the area of work expanded by reconfiguring the variable length crank link (VLC). However, after adjusting the length of the handle, it will not move until required by another patient.

**3.2. Path Tracking Error.** In order to determine the tracking error according to the natural course of the flexoextension path of the middle finger, the difference between the OD and OP vectors is measured. The maximum error has a value of

TABLE 3: Construction parameters for the four R-RRT mechanisms.

Finger/length	$L_1$ min (mm)	$L_1$ max (mm)	$L_2$ (mm)	$L_3$ (mm)	$L_5$ (mm)	$L_7$ (mm)	$\beta$ ( $^\circ$ )
Index	47.15	77.70	387.66	74.90	26.67	44.46	80
Middle	53.08	87.48	436.44	84.33	30.03	50.05	80
Ring	50.01	82.42	411.19	79.45	28.29	47.15	80
Little	38.78	63.91	318.85	61.61	21.94	36.56	80

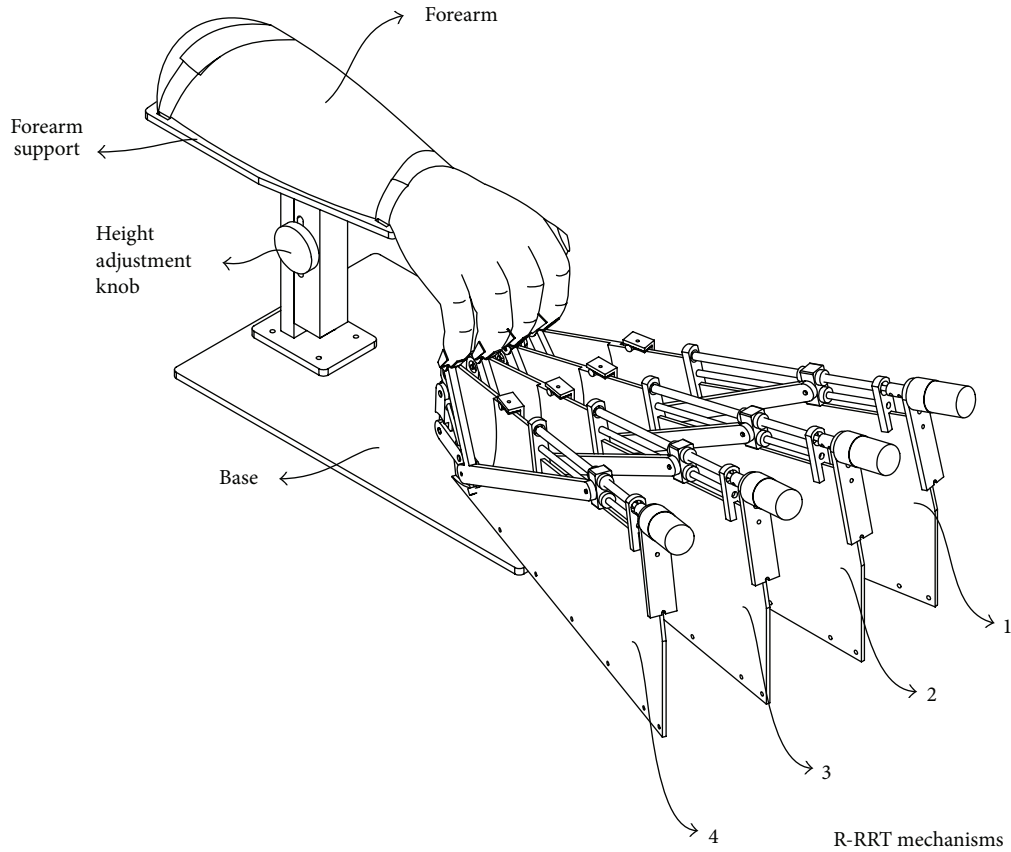


FIGURE 7: General view of the of the flexoextensor robotic system mechanisms.

2.98%. Figure 10 shows the graph of error in the range of movement of the crank link.

The patient hand size is bounded in the range of 158.39 mm to 186.63 mm and is divided into eight intervals with increments of 4.30 mm. With the constant value of the length of the coupler link  $L_2 = 436.44$  mm, length of the extension of the coupler link  $L_{ext} = 84.33$  mm, and the extension of the coupler link angle  $\beta = 80^\circ = 1.396$  radians, only the length of the link is modified and the paths are shown in Figure 11. Table 4 shows the values of nine hand sizes and their maximum tracking error obtained.

**3.3. Abduction Movement.** In natural extension movements of the hand fingers, an abduction movement is also developed by index, ring, and little finger. When the MCP joint is flexed, the lateral ligaments are tight; it makes the abduction movements difficult or impossible [16]. The index, ring, and little fingers have major amplitude of abduction movement as  $30^\circ$  [Cobos]. The position of each R-RRT mechanism has the

maximum flexion point as reference; in this case, the middle finger does not develop the abduction; then, middle finger mechanism orientation is parallel with the arm longitudinal axis. The mechanism orientation for index, ring, and little fingers allows an abduction movement, which begins with  $0^\circ$  in maximum flexion and ends with an angle  $\gamma$  in maximum extension. If the angle  $\gamma$  takes the value of the half of maximum abduction; then,  $\gamma = 15^\circ$ . The result is an abduction movement of  $15^\circ$  for index and ring finger with reference to middle finger, and  $15^\circ$  of little finger with reference to ring finger. This results in comfortable movements for four fingers, index to little finger, and the metacarpophalangeal joint movement in flexoextension and abduction.

#### 4. Conclusions

The design of the reconfigurable robotic system for flexoextension can be adapted to the size of the hand; it is the result of a compromise between functionality and

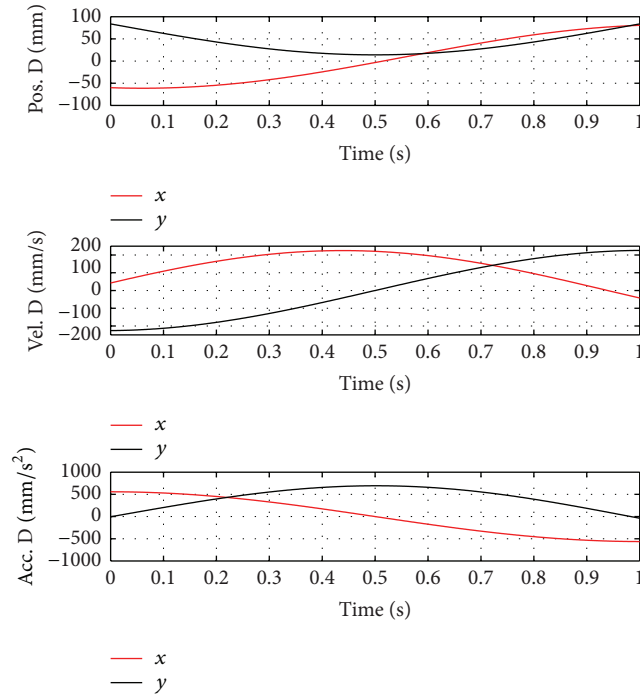


FIGURE 8: Result of position, velocity, and acceleration of point D, for  $180^\circ \leq \varphi \leq 360^\circ$ .

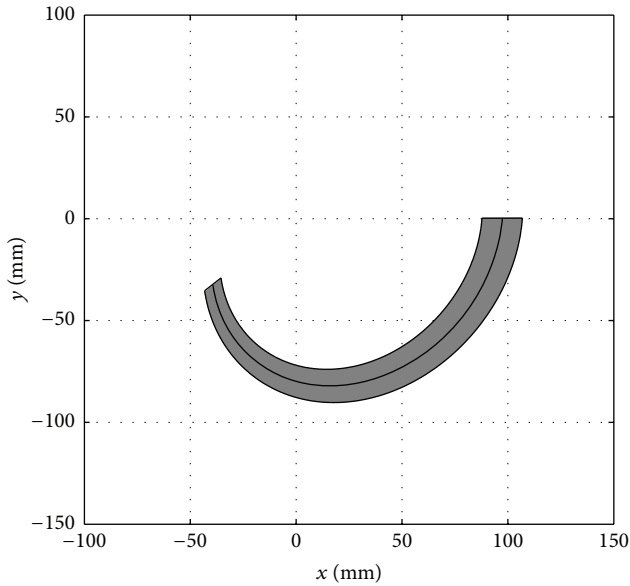


FIGURE 9: Work area of reconfigurable flexoextensor mechanism (the middle finger case).

practicality required for the movement of the fingers as part of rehabilitation therapies. The movement of the fingers is performed following their natural flexoextension path and prevents hyperextension, ensuring that the fingers never perform unnatural movements. The four R-RRT mechanisms orientation allows a  $15^\circ$  abduction movement for index, ring, and little fingers. The reconfigurability of each of the four R-RRT mechanisms allows the system to fit the hand size of

TABLE 4: Maximum tracking error for different lengths of hand.

Point	Hand size (mm)	Length of crank (mm)	Maximum tracking error (%)
1	158.39	53.07	2.97
2	162.70	57.38	2.97
3	167.01	61.68	2.97
4	171.31	65.98	2.97
5	175.62	70.28	2.97
6	179.93	74.56	2.96
7	184.24	78.88	2.96
8	188.54	83.18	2.96
9	192.85	87.48	2.97

each patient, allowing attention to a larger percentage of the population considered for design.

An advantage of our proposal is related to the patient comfort; that is, the patient's hand should not carry anything, since it is based on the system. This represents an advantage over gloves or exoskeletons whose mass must be loaded by the user's hand. The system will provide the required forces to move the fingers and allow the physiotherapist, by means of an electronic control system, to monitor and record the progress for evaluation of both the evolution of patients and rehabilitation protocols. Levanon says that "... technology is the language of the next generation and therapists must adapt the types of treatments that are able to provide their customers, and they need to be enabled to use family and significant equipment with customers in the future" [4].

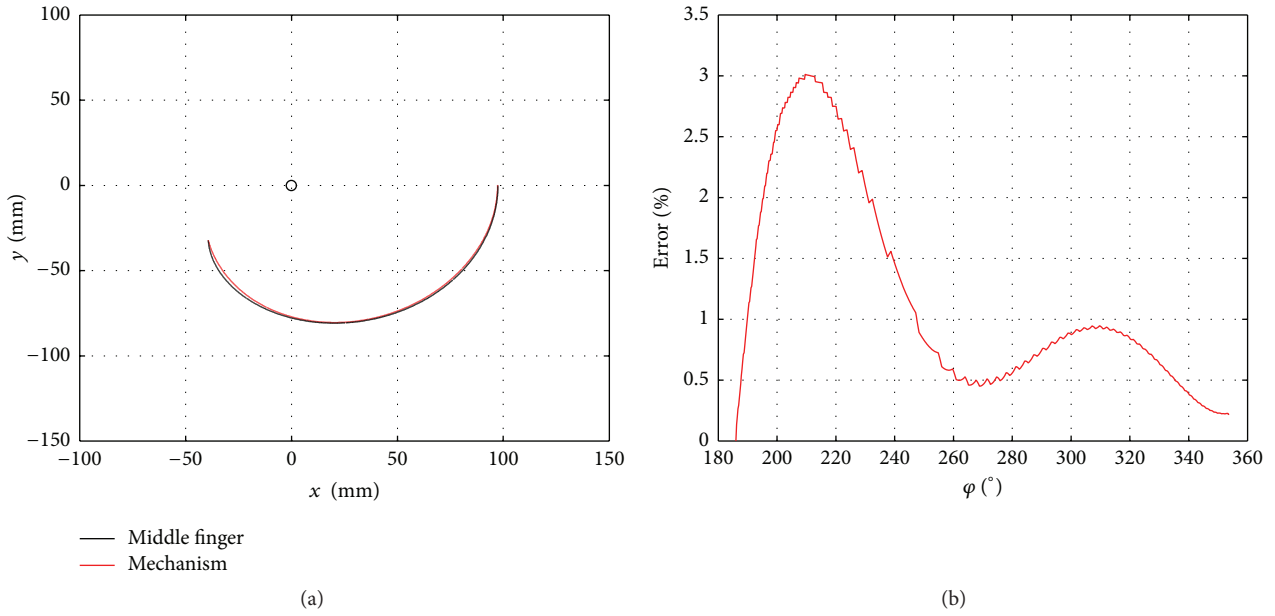


FIGURE 10: Error tracking of the mechanism (a) according to the natural path of flexion and extension of the middle finger and (b) percentage error in the path.

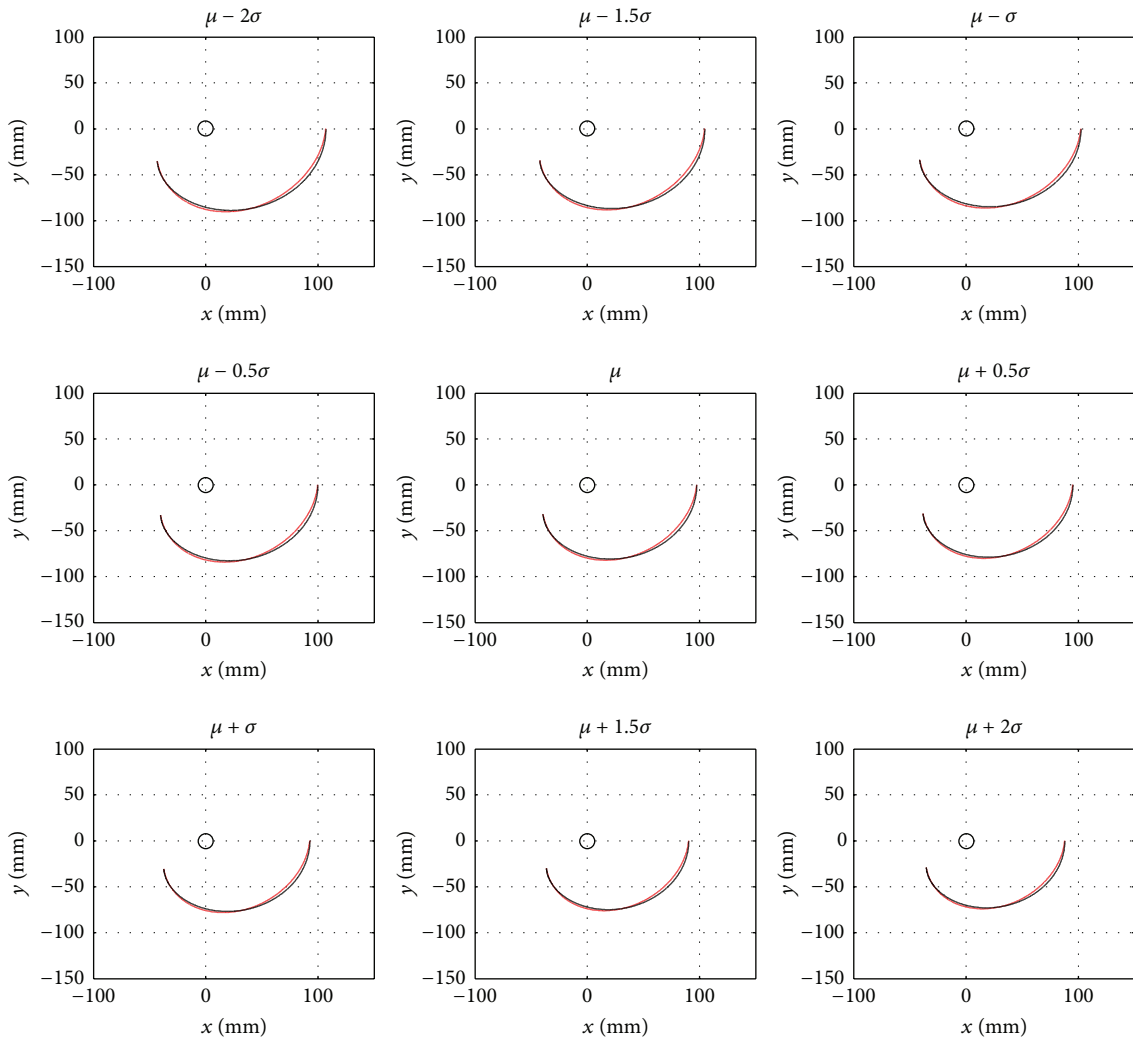


FIGURE 11: Paths of the middle finger and R-RRT proposed mechanism.

## Competing Interests

The authors declare that they have no competing interests.

## Acknowledgments

The authors would like to acknowledge the financial support of the institutions: Instituto Politécnico Nacional, Universidad Tecnológica de Querétaro and CONACYT, also CRIQ Centro de Rehabilitación Integral de Querétaro, and the therapists for their advice and discussion about rehabilitation protocols.

## References

- [1] WHO, *Disability and Rehabilitation*, World Health Organization, 2006, [http://www.who.int/nmh/donorinfo/vip\\_promoting-access\\_healthcare\\_rehabilitation\\_update.pdf.pdf](http://www.who.int/nmh/donorinfo/vip_promoting-access_healthcare_rehabilitation_update.pdf.pdf).
- [2] C. G. Burgar, P. S. Lum, P. C. Shor, and H. F. Machiel Van der Loos, "Development of robots for rehabilitation therapy: the Palo Alto VA/Stanford experience," *Journal of Rehabilitation Research and Development*, vol. 37, no. 6, pp. 663–673, 2000.
- [3] P. Heo, G. M. Gu, S.-J. Lee, K. Rhee, and J. Kim, "Current hand exoskeleton technologies for rehabilitation and assistive engineering," *International Journal of Precision Engineering and Manufacturing*, vol. 13, no. 5, pp. 807–824, 2012.
- [4] Y. Levanon, "The advantages and disadvantages of using high technology in hand rehabilitation," *Journal of Hand Therapy*, vol. 26, no. 2, pp. 179–183, 2013.
- [5] P. Maciejasz, J. Eschweiler, K. Gerlach-Hahn, A. Jansen-Troy, and S. Leonhardt, "A survey on robotic devices for upper limb rehabilitation," *Journal of Neuroengineering and Rehabilitation*, vol. 11, no. 1, article 3, 2014.
- [6] A. Quesnot, J.-C. Chanussot, and R.-G. Danowski, "Main et doigts," in *Rééducation de l'Appareil Locomoteur. Tome 2 Membre Supérieur*, E. Masson, Ed., pp. 353–419, Elsevier Masson, 2nd edition, 2011.
- [7] S. E. Fasoli, H. I. Krebs, J. Stein, W. R. Frontera, and N. Hogan, "Effects of robotic therapy on motor impairment and recovery in chronic stroke," *Archives of Physical Medicine and Rehabilitation*, vol. 84, no. 4, pp. 477–482, 2003.
- [8] J. R. Carey, T. J. Kimberley, S. M. Lewis et al., "Analysis of fMRI and finger tracking training in subjects with chronic stroke," *Brain*, vol. 125, no. 4, pp. 773–788, 2002.
- [9] T. Kitago, J. Goldsmith, M. Harran et al., "Robotic therapy for chronic stroke: general recovery of impairment or improved task-specific skill?" *Journal of Neurophysiology*, vol. 114, no. 3, pp. 1885–1894, 2015.
- [10] C. N. Schabowsky, S. B. Godfrey, R. J. Holley, and P. S. Lum, "Development and pilot testing of HEXORR: hand EXOskeleton rehabilitation robot," *Journal of NeuroEngineering and Rehabilitation*, vol. 7, article 36, 2010.
- [11] M. A. Delph, S. A. Fischer, P. W. Gauthier, C. H. M. Luna, E. A. Clancy, and G. S. Fischer, "A soft robotic exomusculature glove with integrated sEMG sensing for hand rehabilitation," in *Proceedings of the IEEE 13th International Conference on Rehabilitation Robotics (ICORR '13)*, June 2013.
- [12] O. Lamercy, L. Dovat, V. Johnson et al., "Development of a robot-assisted rehabilitation therapy to train hand function for activities of daily living," in *Proceedings of the IEEE 10th International Conference on Rehabilitation Robotics (ICORR '07)*, pp. 678–682, Noordwijk, Netherlands, June 2007.
- [13] M. Bouzit, G. Burdea, G. Popescu, and R. Boian, "The Rutgers Master II-new design force-feedback glove," *IEEE/ASME Transactions on Mechatronics*, vol. 7, no. 2, pp. 256–263, 2002.
- [14] Tyromotion, AMADEO-Five Fingers. One Amadeo. For All Phases of Rehabilitation, 2016, <http://tyromotion.com/en/products/amadeo>.
- [15] R. Ávila Chaurand, L. R. Prado León, and E. L. González Muñoz, *Dimensiones antropométricas Población Latinoamericana*, Universidad de Guadalajara, Guadalajara, Mexico, 2nd edition, 2007.
- [16] A. I. Kapandji, *Fisiología Articular: Esquemas Comentados de Mecánica Humana*, Editorial Médica Panamericana, Madrid, Spain, 6th edition, 2006.
- [17] B. Tondu, "Kinematic modelling of anthropomorphic robot upper limb with human-like hands," in *Proceedings of the International Conference on Advanced Robotics (ICAR '09)*, pp. 1–9, IEEE, Munich, Germany, June 2009.
- [18] J. Denavit and R. S. Hartenberg, "A kinematic notation for lower-pair mechanisms based on matrices," *Journal of Applied Mechanics*, vol. 23, pp. 215–221, 1955.
- [19] J. J. Craig, *Introduction to Robotics: Mechanics and Control*, Addison-Wesley, Boston, Mass, USA, 2nd edition, 1955.
- [20] C. E. Syrseloudis, I. Z. Emiris, T. Lilas, and A. Maglara, "Design of a simple and modular 2-DOF ankle physiotherapy device relying on a hybrid serial-parallel robotic architecture," *Applied Bionics and Biomechanics*, vol. 8, no. 1, pp. 101–114, 2011.
- [21] R. L. Norton, *Design of Machinery: An Introduction to the Synthesis and Analysis of Mechanisms and Machines*, Mcgraw-Hill, New York, NY, USA, 5th edition, 2012.
- [22] H. Zhou and K.-L. Ting, "Adjustable slider-crank linkages for multiple path generation," *Mechanism and Machine Theory*, vol. 37, no. 5, pp. 499–509, 2002.

## Research Article

# Optical Enhancement of Exoskeleton-Based Estimation of Glenohumeral Angles

Camilo Cortés,<sup>1,2</sup> Luis Unzueta,<sup>1</sup> Ana de los Reyes-Guzmán,<sup>3</sup>  
Oscar E. Ruiz,<sup>2</sup> and Julián Flórez<sup>1</sup>

<sup>1</sup>*Health and Biomedical Applications, Vicomtech-IK4, Mikeletegi Pasealekua 57, 20009 San Sebastián, Spain*

<sup>2</sup>*Laboratorio de CAD CAM CAE, Universidad EAFIT, Carrera 49 No. 7 Sur-50, 050022 Medellín, Colombia*

<sup>3</sup>*Biomechanics and Technical Aids Department, National Hospital for Spinal Cord Injury, SESCAM, Finca la Peraleda s/n, 45071 Toledo, Spain*

Correspondence should be addressed to Julián Flórez; [jflorez@vicomtech.org](mailto:jflorez@vicomtech.org)

Received 15 January 2016; Revised 1 April 2016; Accepted 26 April 2016

Academic Editor: Qining Wang

Copyright © 2016 Camilo Cortés et al. This is an open access article distributed under the Creative Commons Attribution License, which permits unrestricted use, distribution, and reproduction in any medium, provided the original work is properly cited.

In Robot-Assisted Rehabilitation (RAR) the accurate estimation of the patient limb joint angles is critical for assessing therapy efficacy. In RAR, the use of classic motion capture systems (MOCAPs) (e.g., optical and electromagnetic) to estimate the Glenohumeral (GH) joint angles is hindered by the exoskeleton body, which causes occlusions and magnetic disturbances. Moreover, the exoskeleton posture does not accurately reflect limb posture, as their kinematic models differ. To address the said limitations in posture estimation, we propose installing the cameras of an optical marker-based MOCAP in the rehabilitation exoskeleton. Then, the GH joint angles are estimated by combining the estimated marker poses and exoskeleton Forward Kinematics. Such hybrid system prevents problems related to marker occlusions, reduced camera detection volume, and imprecise joint angle estimation due to the kinematic mismatch of the patient and exoskeleton models. This paper presents the formulation, simulation, and accuracy quantification of the proposed method with simulated human movements. In addition, a sensitivity analysis of the method accuracy to marker position estimation errors, due to system calibration errors and marker drifts, has been carried out. The results show that, even with significant errors in the marker position estimation, method accuracy is adequate for RAR.

## 1. Introduction

The application of robotics and Virtual Reality (VR) to motor neurorehabilitation (Figure 1) has been beneficial for patients, as they receive intensive, repetitive, task-specific, and interactive treatment [1–4].

The assessment of (a) patient movement compliance with the prescribed exercises and (b) patient long-term improvement is critical when planning and evaluating the efficacy of RAR therapies. In order to obtain the patient motion data to conduct the said assessments, one has to estimate patient posture (i.e., the joint angles of the limbs). Patient posture estimation methods need to be practical and easy to set up for the physician, so that the said assessments can indeed be an integral part of the therapy.

Current methods for estimating patient posture are either cumbersome or not accurate enough in exoskeleton-based

therapies. In order to overcome such limitations, we propose a method where low-cost RGB-D cameras (which render color and depth images) are directly installed in the exoskeleton and colored planar markers are attached to the patient's limb to estimate the angles of the GH joint, thereby overcoming the individual limitations of each of these systems.

## 2. Literature Review

Optical, electromagnetic, and inertial MOCAPs have been used in many rehabilitation scenarios for accurate posture estimation [5]. However, the use of the said MOCAPs in exoskeleton-based rehabilitation is limited by the factors discussed below:

- (1) Optical marker-based systems (e.g., Optotrak, CODA, Vicon) are considered the most accurate for

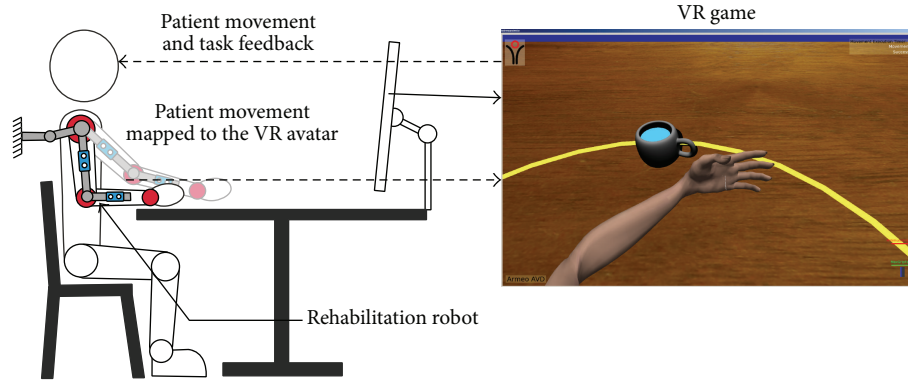


FIGURE 1: Robotic and VR-based rehabilitation.

human motion capture [5]. Reference [6] reports Optotrak errors of 0.1–0.15 mm. However, in the specific case of exoskeleton-based therapy, these systems require redundant sensors and markers to cope with occlusions caused by the exoskeletal body. Therefore, their specific usage for therapy is limited. Besides, the cost of these systems is high (50 K–300 K USD [7]) compared to nonoptical MOCAPs.

- (2) Electromagnetic systems do not suffer from optical occlusions. However, they are easily perturbed by surrounding metallic objects (e.g., exoskeletal body) and electric/magnetic fields [5]. An additional drawback of these systems is their limited detection volume when compared to optical systems.
- (3) Inertial and Magnetic Measurement Systems are robust, handy, and economical for full-body human motion detection (upper limb tracking in [8, 9]). With the use of advanced filtering techniques, inertial sensor drift errors are reduced and a dynamic accuracy of 3 deg. RMS [5] is achieved. However, these systems require patients to perform calibration motions/postures, which may not be suitable for those with neuromotor impairments.

In exoskeleton-based rehabilitation, the prevailing approach to estimate human limb joint angles (e.g., [10–13]) is to approximate them with the angles of the exoskeleton joints. However, misalignment between the axes of the exoskeleton and human joints may produce large estimation errors [14, 15]. Accurate estimation of GH joint angles is hard to achieve using this approach, since it requires an exoskeleton with a complex kinematic structure that considers the concurrent motion of the sternoclavicular and acromioclavicular joints.

Recognizing the differences in the kinematic structures of the limb and exoskeleton, [16] presents a computational method which considers the limb and exoskeleton parallel kinematic chains related by the cuff constraints joining them together. Then, the IK problem of the parallel kinematic chain can be solved to find the limb joint angles. A limitation of this method is that its performance has been demonstrated solely for analytic (1-DOF) movements of the elbow and wrist joints.

The estimation accuracy of the GH joint angles has yet to be determined.

Reference [17] presents a computational method based on the estimation of the arm swivel angle (which parametrizes arm posture) for exoskeleton-based therapy. The arm IK is solved with a redundancy resolution criterion that chooses a swivel angle that allows the subject to retract the palm to the head efficiently. The approach in [17] extends their previous work in [18, 19] by considering the influence of the wrist orientation on the swivel angle estimation. Although the error of the swivel angle estimation (mean error  $\approx 4$  deg.) has been reported for compound movements [17], individual errors in the wrist, elbow, and GH joint angles are not indicated.

Reference [20] extends the method in [17] to estimate the wrist angles and assesses its performance for compound movements (mean RMSE  $\approx 10$  deg. in the swivel angle estimation). Reference [20] reports the individual errors of the arm joint angles solely for the movement task where the swivel angle was best estimated (mean RMSE  $\approx 5$  deg. in the swivel angle estimation). No errors of the arm joint angles were discussed for the other cases. A limitation of the work in [20] is that the MOCAP used to obtain the reference angles to assess their method performance is a custom-made inertial system with no reported measurement accuracy.

*2.1. Conclusions of the Literature Review.* We remind the reader that the general context of this paper is the estimation of the GH joint angles.

- (1) As per our literature review, no MOCAPs have been developed for the specific scenario of exoskeleton-based rehabilitation. Even if current MOCAPs and the exoskeleton could be set up for simultaneous use (e.g., [15, 16]), the setup protocol and operation are intricate and conflicting with the usual time and resources available for patient treatment.
- (2) Exoskeleton-based posture estimations present limitations in their accuracy due to kinematic mismatch of the limb and exoskeleton [15, 16].
- (3) The accuracy of the GH joint angle estimations provided by computational methods in [16, 17] is

unknown. Reference [20] extends the work in [17] by estimating the wrist angles. Reference [20] solely reports the estimation accuracy of the GH angles for the best-case scenario and the precision of its ground-truth is not indicated.

**2.2. Contributions of This Paper.** In response to the limitations discussed in the estimation of patient joint angles in exoskeleton-based therapy (Sections 2 and 2.1), this paper introduces a hybrid approach to estimate, in real-time, the GH joint angles. This hybrid system is composed of a low-cost marker-based vision system and the rehabilitation robot, overcoming the individual limitations of its constitutive subsystems:

- (a) Occlusions are minimized, which are a major limitation of optical systems.
- (b) Accuracy of joint angle estimation is improved, which is a major limitation of exoskeleton-based systems.

This paper presents the implementation and assessment of our method using simulated human motion data. In addition, a sensitivity analysis of our method accuracy to marker position estimation errors is carried out.

We have considered the following scenarios of application for the proposed method in the RAR domain:

- (A) Precise estimation of GH joint angles during rehabilitation or evaluation sessions of GH joint analytic movements.
- (B) Acquisition of GH joint movement data enabling validation and improvement of other posture estimation methods without using expensive redundant optical MOCAPs.

### 3. Methods

**3.1. Problem Definition.** This section presents the problem of estimating the patient limb GH joint angles during the GH joint RAR using the proposed hybrid motion capture system (a detailed version of the problem definition is presented in the Appendix). This problem can be stated as follows.

*Given.* Consider the following:

- (1) Patient: (a) the kinematic model (e.g., the Denavit-Hartenberg parameters [21]) of the human upper limb ( $H$ ) (Figure 2(a)).
- (2) Exoskeleton: (a) the kinematic model of the exoskeleton ( $E$ ) and (b) the exoskeleton joint angles at any instant of the therapy ( $v^E(t)$ ) (Figure 2(b)).
- (3) Marker-based optical motion capture system ( $R$ ): (a) color and depth information captured by the RGB-D cameras installed in the exoskeleton links and (b) geometry and color of the markers attached to the patient upper limb (Figure 2(c)).

*Goal.* The goal is to estimate the patient GH joint angles ( $v_G^H(t)$ ) with minimum error during the GH joint rehabilitation exercises.

**3.2. Kinematic Models.** This section discusses the main features of the kinematic models of the human limb and exoskeleton used for the posture estimation method.

**3.2.1. Kinematic Model of the Human Upper Body.** The human kinematic model is denoted by  $H(L^H, J^H)$ , where  $L^H$  and  $J^H$  are the sets of links and joints, respectively. We use the human upper body model presented in [16] (Figure 2(a)), which includes joints of the spine, scapulothoracic system, and arm. The upper limb is modeled with 9 DOFs: 2 DOFs of the scapulothoracic system, 3 DOFs of the GH joint (spherical joint), 2 DOFs of the elbow, and 2 DOFs of the wrist (see further details in the Appendix). This model presents the following advantages:

- (a) It can be easily implemented in robotic simulators and similar tools.
- (b) It is suitable for simulating human-robot interaction in real-time [16].
- (c) The spherical model of the GH joint avoids limitations of other representations of such joint, like the Gimbal lock that occurs when using the three concurrent and orthogonal 1-DOF revolute joints' model [22].

**3.2.2. Kinematic Model of the Exoskeleton.** The exoskeleton kinematic model is denoted by  $E(L^E, J^E)$ , where  $L^E$  and  $J^E$  are the sets of links and joints, respectively. In this research, the rehabilitation exoskeleton used is the Armeo Spring (Figure 2(b)), which is a passive system that supports the weight of the patient's arm [23] with springs. The Armeo kinematic structure includes rotational joints (equipped with encoders [24, 25]) and prismatic joints (enabling exoskeleton adjustment to the size of each patient). We use the Armeo Spring kinematic model presented in [16], which includes both types of joints (see further details in the Appendix).

**3.3. GH Joint Angles Estimation Method.** The aim of the method is to estimate the GH joint angles with respect to (w.r.t.) a coordinate system (CS) attached to the scapulothoracic system. Figure 2(d) shows the proposed system for the GH joint angle estimation. Our approach is based on the estimation of the upper arm orientation w.r.t. the acromion (Figure 3(a)). According to such requirements, the rationale to install the markers of the optical MOCAP  $R$  is as follows:

- (a) Marker  $m_0$  is rigidly installed in the acromion, so the estimated upper arm orientation can be expressed w.r.t. the  $m_0$  CS (and therefore w.r.t. the scapulothoracic system).
- (b) Marker  $m_1$  is rigidly installed in the upper arm, so that all the rotations of the upper arm are captured by  $m_1$ . The region that was chosen to attach  $m_1$  to the upper arm by using a custom-made fixation (Figure 2(d)) is

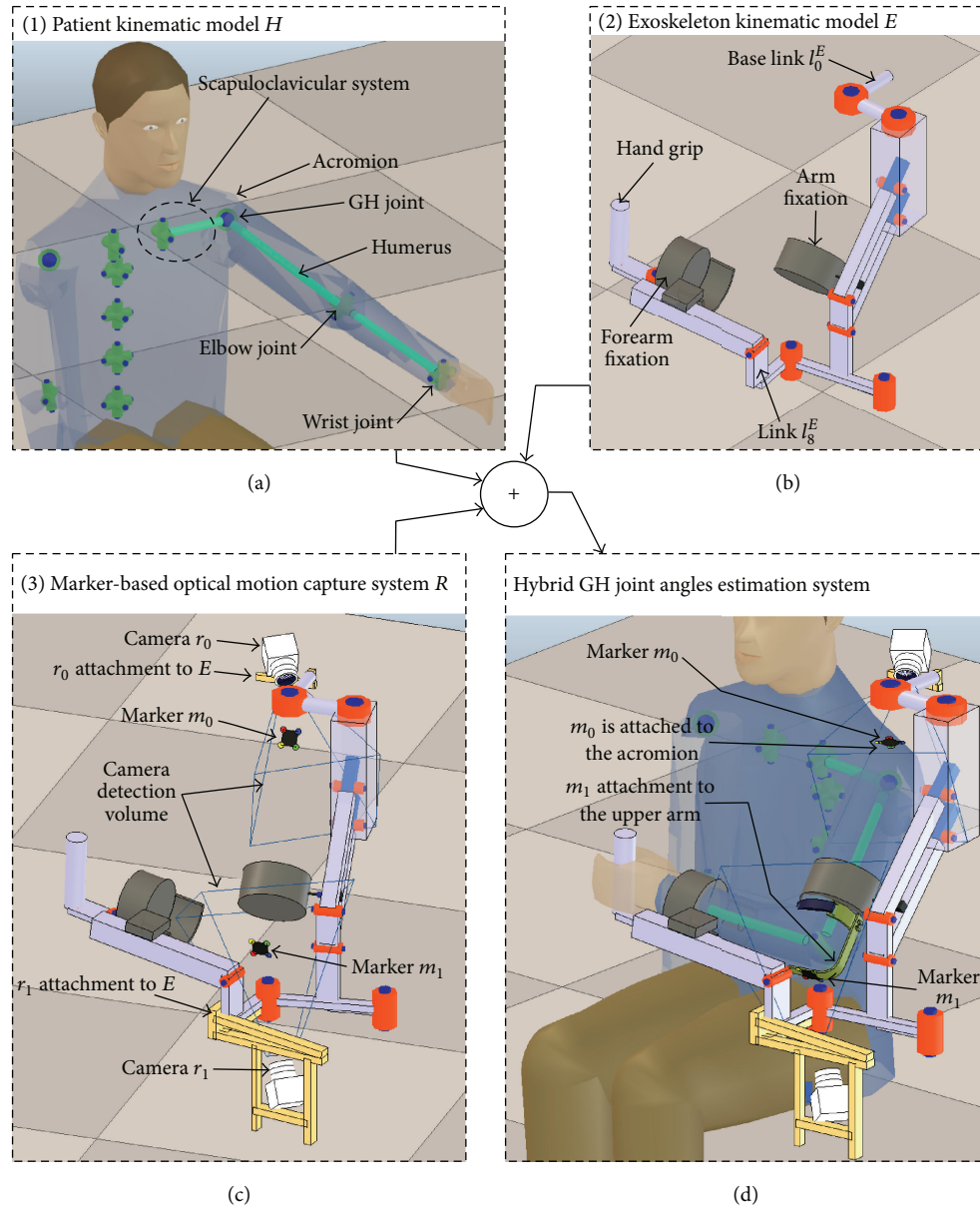


FIGURE 2: Components of the GH joint angles estimation system: (a) human kinematic model, (b) exoskeleton kinematic model, (c) marker-based optical motion capture system, and (d) hybrid GH joint angles estimation system.

the distal part of the humerus (near the elbow). Elbow rotations do not affect the orientation of  $m_1$ .

Reference [26] reports a five-marker installation procedure. This reference explicitly mentions five markers as an acceptable number for clinical upper limb tracking. In this paper, we report the usage of two markers for upper arm tracking. It is not possible to compare the performance of the marker placement protocol proposed here with the one in [26] because the work in [26] addresses (a) non-RAR scenarios, (b) tracking of the entire upper limb, and (c) protocol sensitivity w.r.t. its application on the dominant/nondominant arm and w.r.t. the age of test subjects. However, the work in [26] helps to establish the number of markers compatible with the clinical application of upper limb tracking.

The cameras of the optical motion capture system  $R$  are rigidly attached (using custom-made supports) to exoskeleton links so that camera  $r_0$  detects marker  $m_0$  and camera  $r_1$  detects marker  $m_1$  during the GH joint training. Camera  $r_0$  is mounted on link  $l_0^E$  and camera  $r_1$  is mounted on link  $l_g^E$  (Figure 3(a)).

The cameras used in our system are of low cost. Commercial cameras that present similar specifications to the ones simulated here (Table 1) are Intel® SR300 (99 USD) [27, 28], DepthSense® 525 (164 USD) [29, 30], and CamBoard pico<sup>S</sup> (690 USD) [28, 31].

Figure 3(b) shows an overview of the operation of the estimation method. In order to estimate the upper arm pose, the poses of the markers need to be expressed w.r.t.

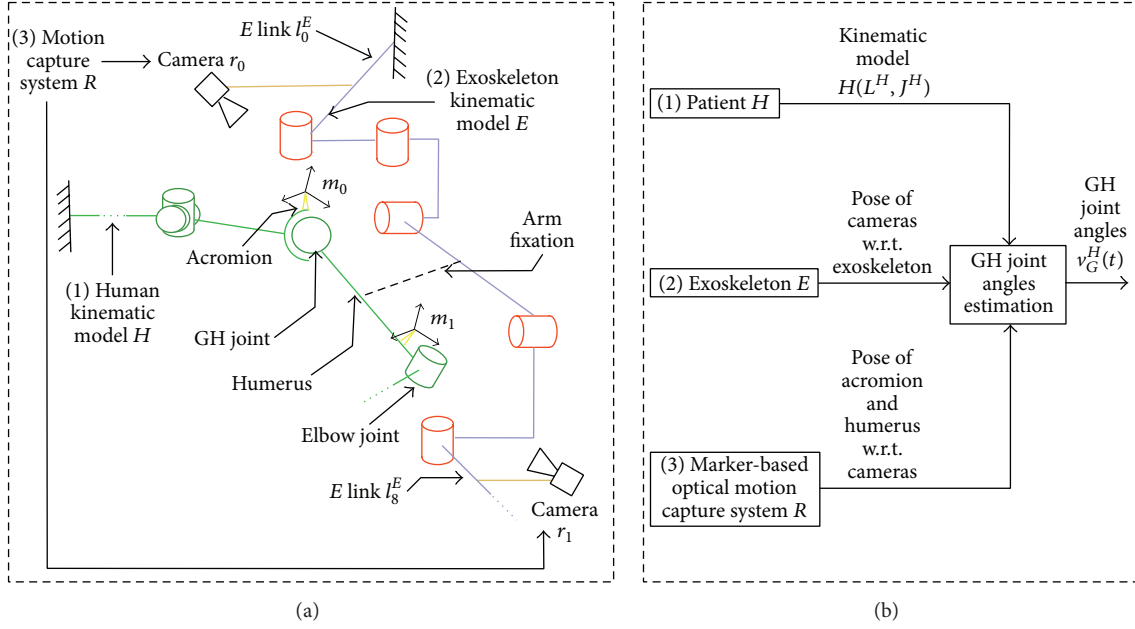


FIGURE 3: (a) Schematic diagram of the hybrid GH joint angles estimation system and (b) high-level operation of the system.

TABLE I: Vision sensor features.

Color camera resolution (px)	128 × 128
Depth camera resolution (px)	128 × 128
Field of view (deg.)	Horizontal = 45; vertical = 45
Minimum sensing distance (meters)	0.05
Maximum sensing distance (meters)	0.3

a common CS. A suitable CS to conduct such estimation is the exoskeleton base.

A summary of the steps to estimate the GH joint angles is as follows:

- (1) Estimate the pose of the markers w.r.t. the cameras.
- (2) Estimate the pose of the cameras w.r.t. the exoskeleton.
- (3) Estimate the pose of the markers w.r.t. the exoskeleton.
- (4) Estimate the upper arm pose w.r.t. the exoskeleton.
- (5) Refer the GH joint angles w.r.t. the acromion (marker  $m_0$  CS).

The details of the mentioned steps are presented in the following sections.

**3.3.1. Estimation of the Pose of the Markers w.r.t. the Cameras.** The purpose of this step is to estimate the position and orientation of the markers (Figure 4) w.r.t. the CSs of the cameras using the color and depth images provided by each camera  $r_i$ :

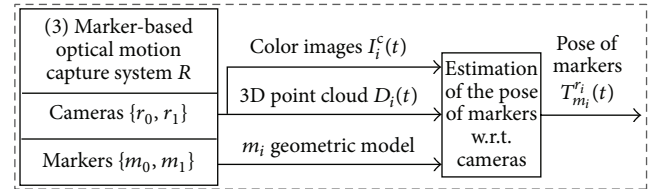


FIGURE 4: Schematic diagram of the iterative estimation of the pose of the markers.

- (A) The RGB image is  $I_i^c$  ( $A \times B$  pixels). The pixel coordinates  $(u, v)$  take values  $0 \leq u \leq A - 1$  and  $0 \leq v \leq B - 1$ .  $C_i$  ( $1 \times 3 * A * B$ ) contains the RGB color associated with each pixel  $(u, v) \in I_i^c$ .
- (B) The depth image associated with the scene in  $I_i^c$  is  $I_i^d$  ( $L \times N$  pixels);  $L \leq A$  and  $N \leq B$ . The pixel coordinates  $(u, v)$  in  $I_i^d$  take values  $0 \leq u \leq L - 1$  and  $0 \leq v \leq N - 1$ . The CS of images  $I_i^c$  and  $I_i^d$  is coincident.  $D_i$  ( $1 \times L * N * 3$ ) contains the  $(x, y, z)$  coordinates of the object in each pixel  $(u, v) \in I_i^d$  w.r.t. the  $r_i$  CS.

The pose estimation of the markers w.r.t. the cameras is based on the reconstruction of the 3D position of the colored disks on the markers. The following steps are taken to estimate the marker pose:

- (1) Estimation of disk coordinates in color image (Figure 5): the purpose of this step is to find the approximate  $(u, v)$  coordinates of the centers of the marker disks in image  $I_i^c$ . The following steps are carried out:
  - (a) Color segmentation in image  $I_i^c$ : image regions containing the colors of the marker disks are

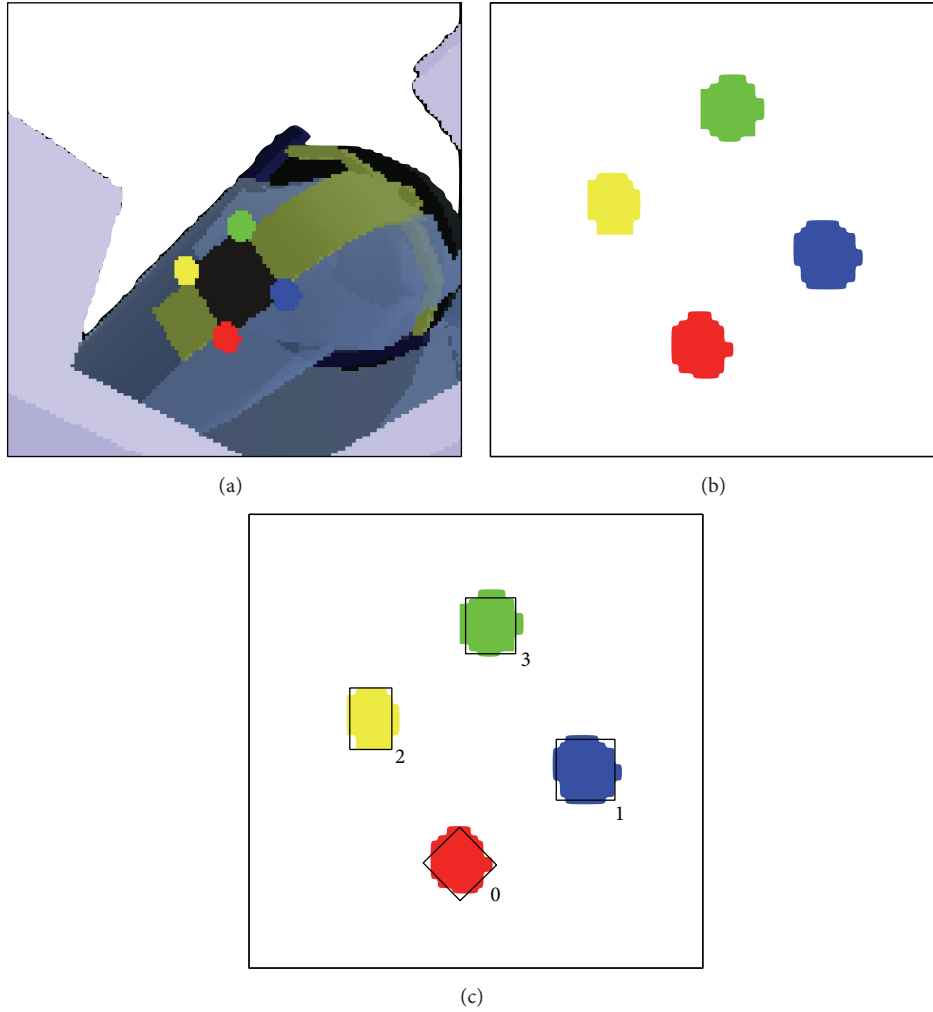


FIGURE 5: Estimation of disk coordinates in color image. (a) Simulated RGB image, (b) result of the color segmentation (zoomed image), and (c) result of the blob extraction (zoomed image).

preserved and the other regions are colored in white. The resulting image is defined as  $I_i^{\text{sc}}$ .

(b) Blob extraction on image  $I_i^{\text{sc}}$ : blob extraction consists of finding the connected regions in the image  $I_i^{\text{sc}}$  sharing the same color and labeling them according to their color.

(c) Disk center coordinates estimation: for each  $j$  ( $j = 0, \dots, n$ ) blob extracted from  $I_i^c$ , the position  $\tilde{p}_j^{I_i^c} \in \mathbb{Z}^2$  of the center of a bounding box for the blob is obtained. This point approximates the actual center of disk  $p_j^{I_i^c}$  (Figure 5). The resulting set of the approximate coordinates of disk centers in  $I_i^c$  is  $\tilde{P}^{I_i^c} = \{\tilde{p}_0^{I_i^c}, \dots, \tilde{p}_j^{I_i^c}, \dots, \tilde{p}_n^{I_i^c}\}$ . The  $\mathbb{Z}^2$  center coordinates are referenced w.r.t. the internal image CS. Blobs are extracted with standard connected-component labeling algorithms.

(2) Estimation of disk coordinates in the camera  $r_i$  CS: this step converts disk coordinates in the internal

image CS into the  $\mathbb{R}^3$  ones w.r.t. the  $r_i$  sensor CS, as follows:

(a) Convert the positions  $(u, v)$  of the disk centers in set  $\tilde{P}^{I_i^c}$  into the image  $I_i^d$  CS. The CSs of images  $I_i^c$  and  $I_i^d$  match. Hence,

$$\tilde{p}_j^{I_i^d} = \begin{pmatrix} \frac{L-1}{A-1} & 0 \\ 0 & \frac{N-1}{B-1} \end{pmatrix} \tilde{p}_j^{I_i^c}. \quad (1)$$

(b) Compute the indices  $a_j^{I_i^d}$  of the  $(x, y, z)$  coordinates of point  $\tilde{p}_j^{I_i^d}$  in array  $D_i$  as follows:

$$\begin{aligned} a_j^{I_i^d}(x) &= 3 * \left( \tilde{p}_j^{I_i^d}(u) \right) + L * \left( \tilde{p}_j^{I_i^d}(v) \right) \\ a_j^{I_i^d}(y) &= 3 * \left( \tilde{p}_j^{I_i^d}(u) \right) + L * \left( \tilde{p}_j^{I_i^d}(v) \right) + 1 \\ a_j^{I_i^d}(z) &= 3 * \left( \tilde{p}_j^{I_i^d}(u) \right) + L * \left( \tilde{p}_j^{I_i^d}(v) \right) + 2. \end{aligned} \quad (2)$$

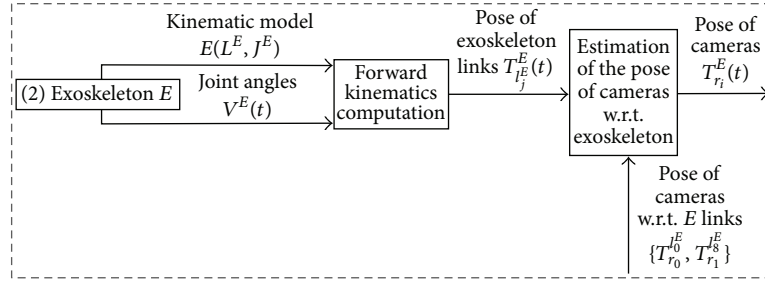


FIGURE 6: Schematic diagram of the iterative estimation of the pose of the cameras.

The point  $\tilde{p}_j^{r_i}$  contains the  $(x, y, z)$  coordinates of point  $\tilde{p}_j^{r_i^d}$  w.r.t. the  $r_i$  CS. The coordinates of point  $\tilde{p}_j^{r_i}$  are obtained as follows:

$$\begin{aligned}\tilde{p}_j^{r_i}(x) &= D_i \left[ a_j^{r_i^d}(x) \right] \\ \tilde{p}_j^{r_i}(y) &= D_i \left[ a_j^{r_i^d}(y) \right] \\ \tilde{p}_j^{r_i}(z) &= D_i \left[ a_j^{r_i^d}(z) \right].\end{aligned}\quad (3)$$

The approximate marker disk centers detected by camera  $r_i$  form the set  $\tilde{P}^{r_i} = \{\tilde{p}_0^{r_i}, \dots, \tilde{p}_j^{r_i}, \dots, \tilde{p}_n^{r_i}\}$ .

- (3) Computation of the marker  $m_i$  CS in the  $r_i$  camera CS: an  $SO(3)$  coordinate frame  $T_{m_i}^{r_i} = [\widehat{V}_x \widehat{V}_y \widehat{V}_z O_{m_i}]$  is attached to each marker:

- (a) Make

$$O_{m_i} = \left( \frac{1}{n+1} \right) \sum_{j=0}^n (\tilde{p}_j^{r_i}). \quad (4)$$

- (b) Use the four disk centers in the marker (Figure 5) as follows:

$$\begin{aligned}\widehat{V}_x &= \left( \frac{1}{2} \right) ((\tilde{p}_0^{r_i} - \tilde{p}_1^{r_i}) + (\tilde{p}_2^{r_i} - \tilde{p}_3^{r_i})) \\ \widehat{V}_y &= \left( \frac{1}{2} \right) ((\tilde{p}_2^{r_i} - \tilde{p}_0^{r_i}) + (\tilde{p}_3^{r_i} - \tilde{p}_1^{r_i})) \\ \widehat{V}_z &= \widehat{V}_x \times \widehat{V}_y.\end{aligned}\quad (5)$$

The submatrix  $[\widehat{V}_x \widehat{V}_y \widehat{V}_z]$  is normalized to guarantee its  $SO(3)$  nature. The frame  $\tilde{T}_{m_i}^{r_i}$  describes the estimated pose of marker  $m_i$  w.r.t. the CS of the camera  $r_i$ .

**3.3.2. Estimation of the Pose of the Cameras w.r.t. the Exoskeleton.** The goal of this step is to find the transformation  $T_{r_i}^E$ , which expresses the pose of the camera  $r_i$  w.r.t. the base of the exoskeleton (Figure 6).

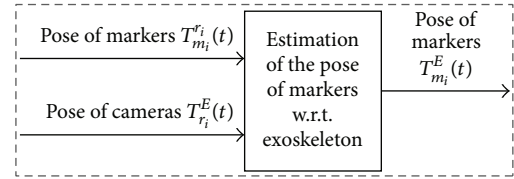


FIGURE 7: Schematic diagram of the iterative estimation of the pose of the markers w.r.t. the exoskeleton CS.

The rigid transformation matrices  $T_{r_0}^{l_0^E}$  and  $T_{r_1}^{l_8^E} \in \mathbb{R}^{4 \times 4}$ , which describe the pose of the cameras  $r_i$  w.r.t. the CS of the link where they are installed, are estimated during system calibration (the calibration matrix can be obtained by camera detection of a 2D/3D calibration object mounted on a known location of the exoskeleton). The poses  $T_{l_0^E}^E$  and  $T_{l_8^E}^E$  of the exoskeleton links  $l_0^E$  and  $l_8^E$  w.r.t. to the exoskeleton base CS are computed using the Forward Kinematics of exoskeleton  $E$ . Then,  $T_{r_0}^E$  and  $T_{r_1}^E$  are estimated as follows:

$$\begin{aligned}\tilde{T}_{r_0}^E &= \tilde{T}_{l_0^E}^E * \tilde{T}_{r_0}^{l_0^E} \\ \tilde{T}_{r_1}^E &= \tilde{T}_{l_8^E}^E * \tilde{T}_{r_1}^{l_8^E}.\end{aligned}\quad (6)$$

**3.3.3. Estimation of the Pose of the Markers w.r.t. the Exoskeleton.** The objective of this step is to estimate the transformation ( $T_{m_i}^E$ ) that describes the pose of marker  $m_i$  w.r.t. the exoskeleton base CS (Figure 7). Transformations  $T_{m_i}^E$  are estimated as follows:

$$\begin{aligned}\tilde{T}_{m_0}^E &= \tilde{T}_{r_0}^E * \tilde{T}_{m_0}^{r_0} \\ \tilde{T}_{m_1}^E &= \tilde{T}_{r_1}^E * \tilde{T}_{m_1}^{r_1}.\end{aligned}\quad (7)$$

**3.3.4. Estimation of the Upper Arm Pose w.r.t. the Exoskeleton.** The purpose of this step is to estimate the upper arm pose ( $T_{arm}^E$ ) w.r.t. the exoskeleton base CS using the marker poses  $T_{m_i}^E$  (Figure 8). The upper arm direction vector is computed from the estimated position of the end-points of the upper arm (GH and elbow joint centers) as follows (CSs in Figure 9):

- (1) Estimate the position of the GH joint center: the rigid transformation matrix  $T_G^{r_0}$ , which expresses the pose

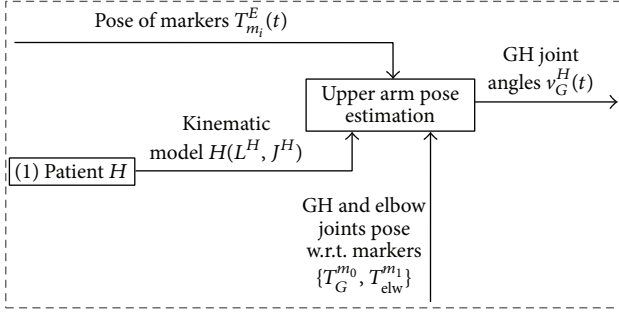


FIGURE 8: Schematic diagram of the iterative estimation of the upper arm pose.

of the GH joint CS w.r.t. the  $m_0$  CS, is estimated during the calibration process of the system. Hence, the GH joint center is estimated as follows:

- (a) Estimate  $T_G^E$ , which is the pose of the GH joint CS w.r.t. the exoskeleton  $E$  base CS (see (8)).
- (b) Extract  $p_G^E$  from  $T_G^E$ . The point  $p_G^E$  is the position of the center of the GH joint seen from the  $E$  CS:

$$\tilde{T}_G^E = \tilde{T}_{m_0}^E * \tilde{T}_G^{m_0}. \quad (8)$$

- (2) Estimate the position of the elbow joint center: the rigid transformation matrix  $T_{elw}^{m_1}$  (elbow joint CS w.r.t. the  $m_1$  CS) is estimated during the calibration process of the system. Hence, the elbow joint center is computed as follows:

- (a) Estimate  $T_{elw}^E$ , which is the pose of the elbow joint CS w.r.t. the exoskeleton  $E$  base CS (see (9)).
- (b) Extract  $p_{elw}^E$  from  $T_{elw}^E$ . The point  $p_{elw}^E$  is the position of the center of the elbow joint seen from the  $E$  CS:

$$\tilde{T}_{elw}^E = \tilde{T}_{m_1}^E * \tilde{T}_{elw}^{m_1}. \quad (9)$$

- (3) Estimate the upper arm position:

- (a) Estimate the arm direction vector as  $\hat{V}_{arm} = (\tilde{p}_G^E - \tilde{p}_{elw}^E) / \|\tilde{p}_G^E - \tilde{p}_{elw}^E\|$ .
- (b) Estimate the origin of the upper arm CS as  $\tilde{p}_{arm}^E = 1/2 * \|\hat{V}_{arm}\| * \hat{V}_{arm} + \tilde{p}_{elw}^E$ .

- (4) Estimate the upper arm orientation: the estimated orientation of the upper arm is computed using Euler angle  $yxz$  decomposition w.r.t. the base CS of exoskeleton  $E$ :

- (a) Estimate the rotation of the arm around the  $y$ -axis of the  $E$  CS using the projection of  $\hat{V}_{arm}$  on the  $x$ - $z$  plane of the fixed  $E$  CS.
- (b) Compute the rotation of the arm around the mobile  $x$ -axis of  $E$  CS from the inner product of  $\hat{V}_{arm}$  with the mobile  $z$ -axis of  $E$  CS.

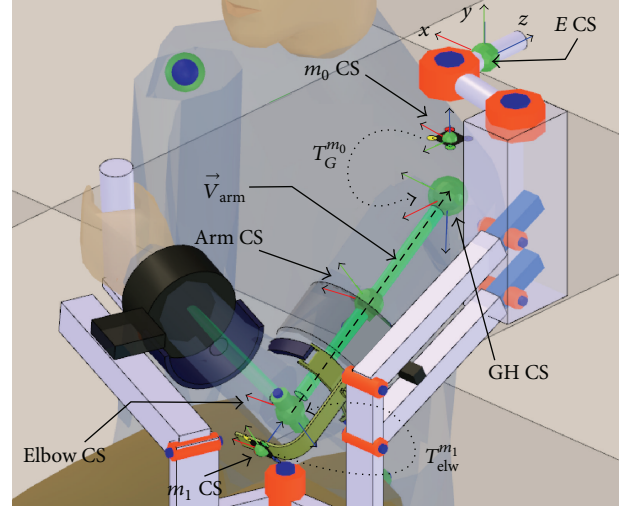


FIGURE 9: Coordinate systems for the upper arm pose estimation.

- (c) Estimate the rotation of the upper arm around its longitudinal axis  $\hat{V}_{arm}$  as the rotation of the marker  $m_1$  around vector  $\hat{V}_{arm}$ . This angle is the one between (i) the mobile  $x$ -axis of  $E$  CS and (ii) the projection of  $x$ -axis of marker  $m_1$  CS onto the  $x$ - $y$  plane of  $E$  CS.

- (5) Express the pose of the upper arm w.r.t. the  $E$  base CS as the  $4 \times 4$  rigid transformation  $T_{arm}^E$ .

3.3.5. *Refer the Angles of the GH Joint w.r.t. the Acromion.* Since  $m_0$  is rigidly attached to the acromion, the upper arm orientation can be expressed w.r.t. the acromion by using the inverse of  $T_{m_0}^E$ :

$$\tilde{T}_{arm}^{m_0} = \tilde{T}_E^{m_0} * \tilde{T}_{arm}^E. \quad (10)$$

3.4. *Implementation and Simulation.* The arm posture estimation method was implemented by using the V-REP robotics simulator [32]. In the simulator, the scene in Figure 2(d) is created, which includes the models of (a) a human patient, (b) an Armeo Spring, (c) the RGB-D vision sensors with the couplings to attach them to the exoskeleton, and (d) the planar markers with the couplings to attach them to the human arm. The configuration of the simulated vision sensors is summarized in Table 1.

For the estimation of the coordinates of disk centers  $P_i^c$  in the image  $I_i^c$ , color segmentation and blob detection algorithms available in the simulator were used. Additional code was written to sort blob centers by color. All additional code was written in LUA (lightweight embeddable scripting language) scripts.

3.4.1. *Generation of the Ground-Truth Poses of the Patient Upper Limb during RAR.* The accuracy of the proposed method is determined by comparing its estimations of the

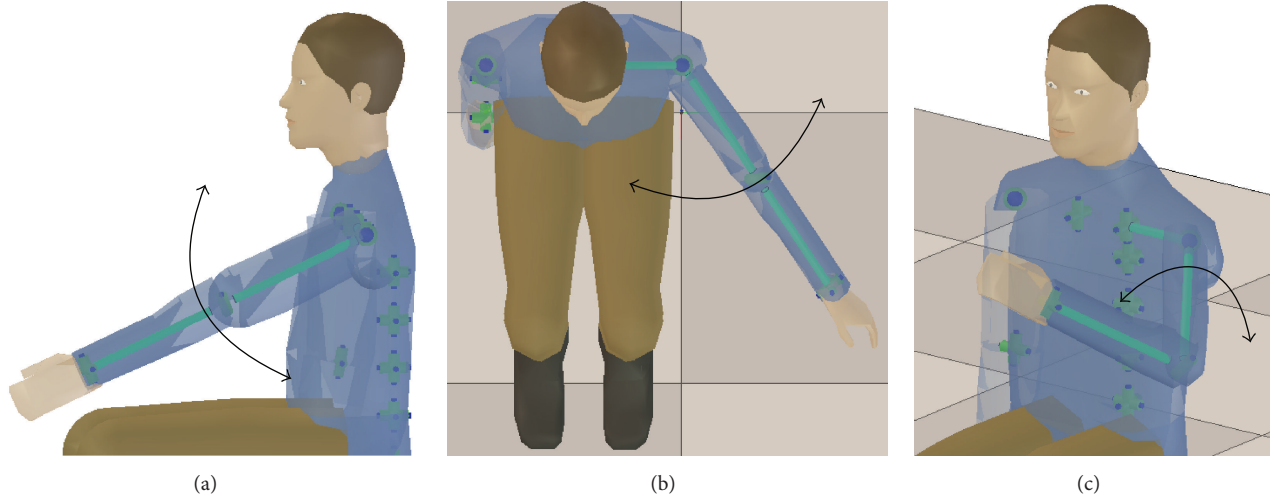


FIGURE 10: GH joint movements: (a) shoulder flexion-extension (SFE), (b) shoulder horizontal abduction-adduction (SAbAd), and (c) shoulder internal rotation (SIR).

TABLE 2: Movement dataset features.

Movement dataset	Amplitude (deg.)	Samples
SAbAd	(6°, 31°, 10°)	1000
SFE	(31°, 8°, 1°)	1000
SIR	(3°, 3°, 34°)	1000
COMB	(40°, 90°, 60°)	2000

upper arm poses with the ones of the simulated human patient (ground-truth values of  $T_{\text{arm}}^{m_0}$ ). To generate movements of the simulated patient that resemble the ones of therapy, we performed the next steps:

- (1) Armeo movement generation: we recorded 4 time sequence datasets of the actual Armeo joint measurements (sampled at 66.6 Hz) while performing the following shoulder movements (Figure 10): (a) shoulder horizontal abduction-adduction (SAbAd), (b) shoulder flexion-extension (SFE), (c) shoulder internal rotation (SIR), and (d) a combination of all the mentioned movements (COMB). These movement history datasets are used to guide a simulation of the Armeo model.
- (2) Patient movement generation: the movements of the patient upper limb that correspond to the recorded movements of the Armeo are computer-generated with the method in [16]. The said method provides an estimation of the patient posture given the joint angles of the exoskeleton by using an inverse kinematics approach.

In this way, four sets (one per movement dataset) of known poses of the upper arm are obtained by simulating patient movement and compared here against those estimated with our method. Our method accuracy is assessed without compensating any time offsets between the reference and estimated angles. In this way, real-time accuracy of

the method is assessed. Table 2 presents the approximate amplitudes of the  $\gamma xz$  Euler angle decomposition of the GH joint movements of the simulated patient w.r.t. its local CS.

#### 3.4.2. Measurement of the Estimation Performance

- (1) Error in the estimation of the markers position: the error in the position estimation of markers  $m_i$  is computed as the RMS of expression  $e_{\text{pos}}^{m_i} = \|p_{m_i}^E - \tilde{p}_{m_i}^E\|$ , where  $i \in \{0, 1\}$ .
- (2) Error in the estimation of the arm pose: the error in the arm position estimation for a GH joint movement dataset ( $e_{\text{pos}}^{\text{arm}}$ ) is computed as the RMS of  $\|p_{\text{arm}}^{m_0} - \tilde{p}_{\text{arm}}^{m_0}\|$  for all samples in the movement dataset.

To quantify the error in the arm orientation estimation ( $e_{\text{ori}}^{\text{arm}}$ ), the next steps are carried out:

- (a) Compute the matrix of rotation error  $\text{Rot}_{\text{error}} = \text{Rot}_{\text{arm}}^{m_0} * (\widetilde{\text{Rot}}_{\text{arm}}^{m_0})^{-1}$ , where  $\text{Rot}_{\text{arm}}^{m_0}$  and  $\widetilde{\text{Rot}}_{\text{arm}}^{m_0}$  are the rotation submatrices of transformation matrices  $T_{\text{arm}}^{m_0}$  and  $\widetilde{T}_{\text{arm}}^{m_0}$ , respectively.
- (b) Express  $\text{Rot}_{\text{error}}$  in exponential map notation [22] as  $\vec{e}_{\text{ori}}^{\text{arm}} \in \mathbb{R}^3$ .
- (c) Compute  $e_{\text{ori}}^{\text{arm}}$  as the RMS of  $\|\vec{e}_{\text{ori}}^{\text{arm}}\|$  for all samples in the movement dataset.

**3.5. Sensitivity Analysis.** A sensitivity analysis is carried out to study the influence of relevant parameters on the method accuracy. Formally, the sensitivity analysis determines the effect of the perturbation of the parameter  $Q$  on the objective function  $F(Q)$ . The relative sensitivity of  $F(Q)$  w.r.t.  $Q$ ,  $S_Q^F$ , is

given by (11) [33]. The value of  $S_Q^F$  is the ratio (dimensionless) between the percentual changes in  $F$  and  $Q$ :

$$S_Q^F = \frac{\partial F/F}{\partial Q/Q} = \frac{\partial \ln(F)}{\partial \ln(Q)}. \quad (11)$$

The upper arm pose accuracy (and, therefore, that of the GH joint angles) relies on the precise estimation of the position of the centers of the elbow and GH joints ( $\tilde{p}_{\text{elw}}^E$  and  $\tilde{p}_G^E$ ) (Section 3.3.4), which ultimately depend on the following transformations involving the markers:

- (a)  $\tilde{T}_{m_0}^E$  and  $\tilde{T}_{m_1}^E$  (markers w.r.t. exoskeleton).
- (b)  $T_G^{m_0}$  and  $T_{\text{elw}}^{m_1}$  (GH and elbow joints w.r.t. markers).

The conducted sensitivity analysis focuses on errors in  $T_G^{m_0}$  and  $T_{\text{elw}}^{m_1}$ , given that errors in the estimation of  $\tilde{T}_{m_0}^E$  and  $\tilde{T}_{m_1}^E$  (Section 4.2) are small. Possible causes of errors in  $T_G^{m_0}$  and  $T_{\text{elw}}^{m_1}$  are as follows:

- (1) Inaccurate computation of  $T_G^{m_0}$  and  $T_{\text{elw}}^{m_1}$  during the system calibration.
- (2) Relative displacement of the markers w.r.t. the GH and elbow joints due to skin movement.

In the sensitivity analysis, translations errors in matrices  $T_G^{m_0}$  and  $T_{\text{elw}}^{m_1}$  are induced by disturbing the location of the markers  $m_k$  ( $k = [0, 1]$ ) w.r.t. the CSs of the GH and elbow joints. Since orientation information in  $T_G^{m_0}$  and  $T_{\text{elw}}^{m_1}$  is not used to estimate the upper arm pose, it is excluded from the sensitivity analysis.

For the sensitivity analysis (see (11)), the vector-valued function  $F(q)$  quantifies the estimation error of the arm position and orientation (see (12)) and the parameter set  $q$  represents the marker translation errors. The parameter set  $q$  is defined as  $q = \{q_1, q_2, q_3, q_4, q_5, q_6\}$ , where each  $q_j \in q$  is a scalar representing the magnitude of a translation of a specific marker along a prescribed direction. Table 3 describes the meaning of each parameter in set  $q$ :

$$F(q) = (e_{\text{pos}}^{\text{arm}}(q), e_{\text{ori}}^{\text{arm}}(q)); \quad F(q) : \mathbb{R}^6 \longrightarrow \mathbb{R}^2. \quad (12)$$

The sensitivity analysis procedure (Figure 11) entails the following steps:

- (1) Load the movement dataset of the GH joint to test (SFE, SABAd, SIR, and COMB).
- (2) Select the parameter  $q_j \in q$  to perturb (selection of a marker and a direction of translation). Marker  $m_0$  translates along axes of the GH joint CS. Marker  $m_1$  translates along axes of the elbow joint CS (Figure 12).
- (3) Apply the translation indicated by  $q_j$  to the corresponding marker. The marker perturbation  $q_j$  is applied for the complete movement dataset.
- (4) Compute the estimation errors of the upper arm position and orientation  $F_i(q) = (e_{\text{pos}_i}^{\text{arm}}(q), e_{\text{ori}_i}^{\text{arm}}(q))$  as the simulated patient moves according to the chosen GH joint movement dataset. The current iteration of the process is indicated by index  $i$ .

TABLE 3: Parameters of function  $F(q)$  (error in the position and orientation estimation of the upper arm (see (12))) to study in the sensitivity analysis.

Parameter	Meaning	CS of reference
$q_1$	Translation with magnitude $\ q_1\ $ of $m_0$ along $x$ -axis	GH joint
$q_2$	Translation with magnitude $\ q_2\ $ of $m_0$ along $y$ -axis	GH joint
$q_3$	Translation with magnitude $\ q_3\ $ of $m_0$ along $z$ -axis	GH joint
$q_4$	Translation with magnitude $\ q_4\ $ of $m_1$ along $x$ -axis	Elbow joint
$q_5$	Translation with magnitude $\ q_5\ $ of $m_1$ along $y$ -axis	Elbow joint
$q_6$	Translation with magnitude $\ q_6\ $ of $m_1$ along $z$ -axis	Elbow joint

- (5) Compute the position and orientation components of  $S_{q_j}^F$  as per (11). The derivative of  $F(q)$  w.r.t.  $q_j$  is given by (13). The required derivatives are computed numerically [34, 35]:

$$\frac{\partial F(q)}{\partial q_j} = \left( \frac{\partial e_{\text{pos}}^{\text{arm}}(q)}{\partial q_j}, \frac{\partial e_{\text{ori}}^{\text{arm}}(q)}{\partial q_j} \right). \quad (13)$$

- (6) Increment  $q_j$  by  $\Delta q$  and go to step (3). Repeat the process until the desired number of iterations  $i$  of the procedure is reached.

The complete sensitivity analysis was performed for each movement dataset (SFE, SABAd, SIR, and COMB). The directions in which marker translations occur (Table 3) are chosen so that the markers do not leave the detection volume of the cameras. Table 4 summarizes the parameters of the sensitivity analysis. Translation units are in meters (mts).

## 4. Results and Discussion

This section presents and discusses the results of (a) estimation accuracy of the marker 3D position, (b) estimation accuracy of the upper arm pose, and (c) sensitivity analysis of the estimation accuracy of the upper arm pose w.r.t. translation errors in  $T_G^{m_0}$  and  $T_{\text{elw}}^{m_1}$ .

**4.1. Results of Marker Position Estimation.** Table 5 presents the RMS of the estimation errors of the position of the markers  $m_i$  per movement dataset. The mean RMS errors of the position estimation of  $m_0$  and  $m_1$  for all movement datasets are 0.00083 and 0.00208 mts, respectively.

Figure 13 shows the box plots of the estimation errors in the marker positions for all movement datasets. A greater variation in the position estimation accuracy of marker  $m_1$ , in comparison to that of  $m_0$ , is observed. We have attributed this to (a) the higher linear and rotational velocities and likewise (b) the larger translations and rotations that  $m_1$  undergoes compared to  $m_0$ .

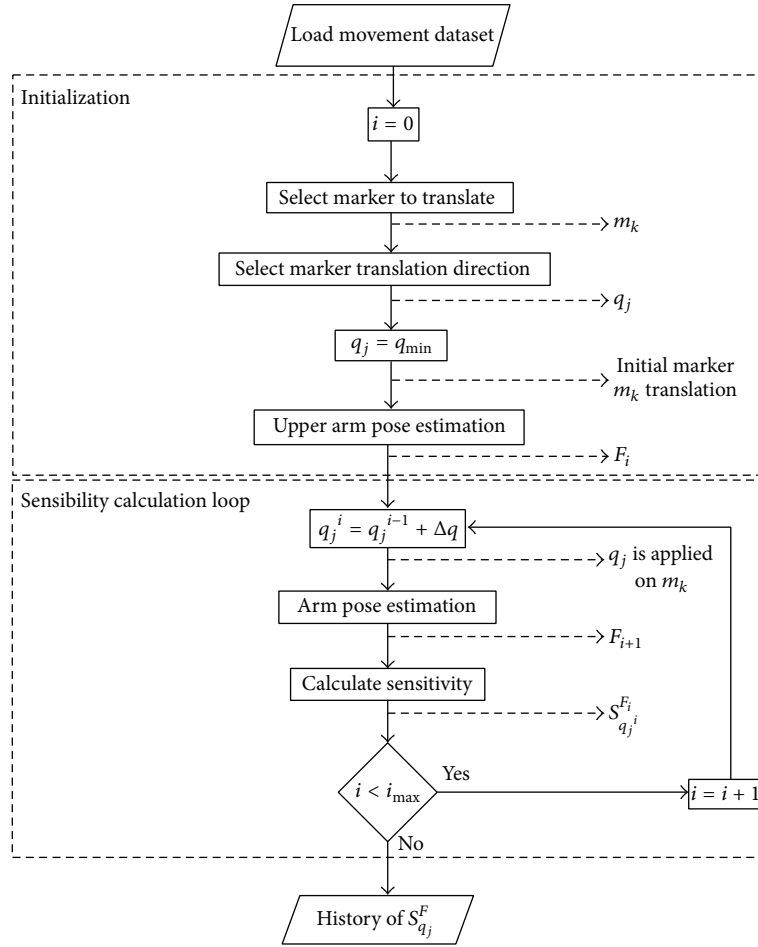


FIGURE 11: Sensitivity analysis steps.

TABLE 4: Parameters of the sensitivity analysis.

Minimum marker translation $q_{\min}$ (mts)	0
Maximum iterations of the sensitivity analysis $i_{\max}$	10
Increment of marker translation in each iteration $\Delta q$ (mts)	0.002
Movement datasets evaluated	4

 TABLE 5: RMS of errors (and standard deviation in parentheses) in the position estimation of markers  $m_i$  in the datasets of GH joint movements.

Movement	$m_0$ [mts]	$m_1$ [mts]
SAbAd	0.00089 (0.0001)	0.00175 (0.001)
SFE	0.00060 (0.0002)	0.00197 (0.0008)
SIR	0.00088 (0.0001)	0.00135 (0.0007)
COMB	0.00097 (0.0003)	0.00324 (0.002)

**4.2. Results of Upper Arm Pose Estimation.** The RMS of errors in the upper arm pose estimation are presented in Table 6. By averaging the results of all movement datasets, errors of 0.00110 mts and 0.88921 deg. in the upper arm position and orientation estimation are obtained. Figure 13 shows the box

TABLE 6: RMS (and standard deviation in parentheses) of errors in the upper arm position and orientation estimation in the assessed movement datasets.

Movement	Position [mts]	Orientation [deg.]
SAbAd	0.00109 (0.0005)	0.92039 (0.4842)
SFE	0.00094 (0.0004)	0.83796 (0.3763)
SIR	0.00091 (0.0002)	0.73465 (0.4156)
COMB	0.00145 (0.0008)	1.0638 (0.5238)

plots of the estimation errors in the upper arm position and orientation for all movement datasets.

In motor rehabilitation, angular errors in the range of 3–5 degrees are considered acceptable for mobility evaluation of patients [6, 36, 37]. Figure 13 shows that our arm orientation estimation accuracy is adequate for exoskeleton-assisted rehabilitation.

**4.3. Results of the Sensitivity Analysis.** The results of the sensitivity analysis per movement dataset of the shoulder are presented in Figures 14, 15, 16, and 17. In each figure, the following subfigures are presented:

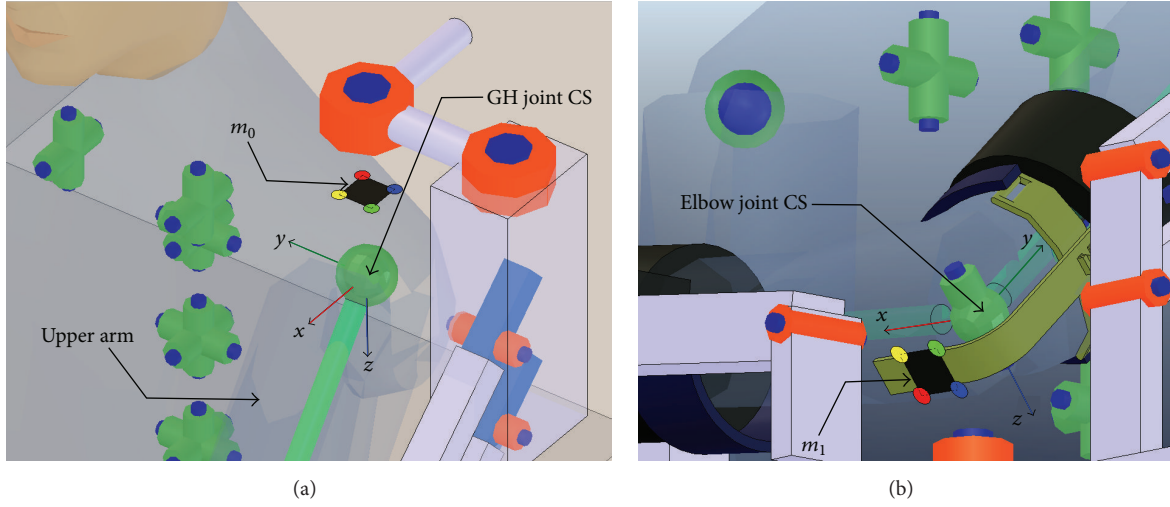


FIGURE 12: Sensitivity analysis. Coordinate systems of reference for the translations of (a) marker  $m_0$  and (b) marker  $m_1$ .

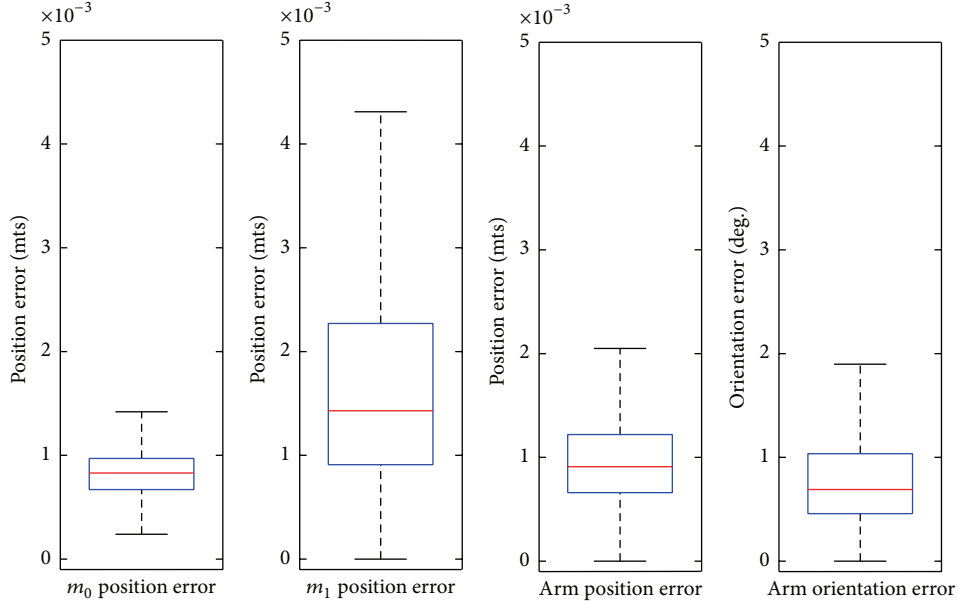


FIGURE 13: Box plots of estimation errors in markers position and upper arm position and orientation for all movement datasets.

- (a) Error in upper arm position estimation ( $e_{\text{pos}}^{\text{arm}}$ ) versus total marker translation ( $q_j$ ): this figure shows the evolution of the absolute error in the upper arm position estimation as the error in the translation components of matrices  $T_G^{m_0}$  and  $T_{\text{elw}}^{m_1}$  increases.
- (b) Error in upper arm orientation estimation ( $e_{\text{ori}}^{\text{arm}}$ ) versus total marker translation ( $q_j$ ): this figure shows the evolution of the absolute error in the upper arm orientation estimation as the error in the translation components of matrices  $T_G^{m_0}$  and  $T_{\text{elw}}^{m_1}$  increases.
- (c) Position component of  $S_{q_j}^F$  versus total marker translation ( $q_j$ ): this figure shows the evolution of the relative sensitivity metric corresponding to the error in the upper arm position estimation as the error in

the translation components of matrices  $T_G^{m_0}$  and  $T_{\text{elw}}^{m_1}$  increases.

- (d) Orientation components of  $S_{q_j}^F$  versus total marker translation ( $q_j$ ): this figure shows the evolution of the relative sensitivity metric corresponding to the error in the upper arm orientation estimation as the error in the translation components of matrices  $T_G^{m_0}$  and  $T_{\text{elw}}^{m_1}$  increases.

**4.3.1. Sensitivity in Arm Position Estimation.** Regarding the arm position estimation, one can observe that translations of marker  $m_0$  produce larger absolute errors than translations of marker  $m_1$ . This difference is due to the fact that the translations of  $m_0$  produce a larger change in  $\|\vec{V}_{\text{arm}}\|$  when

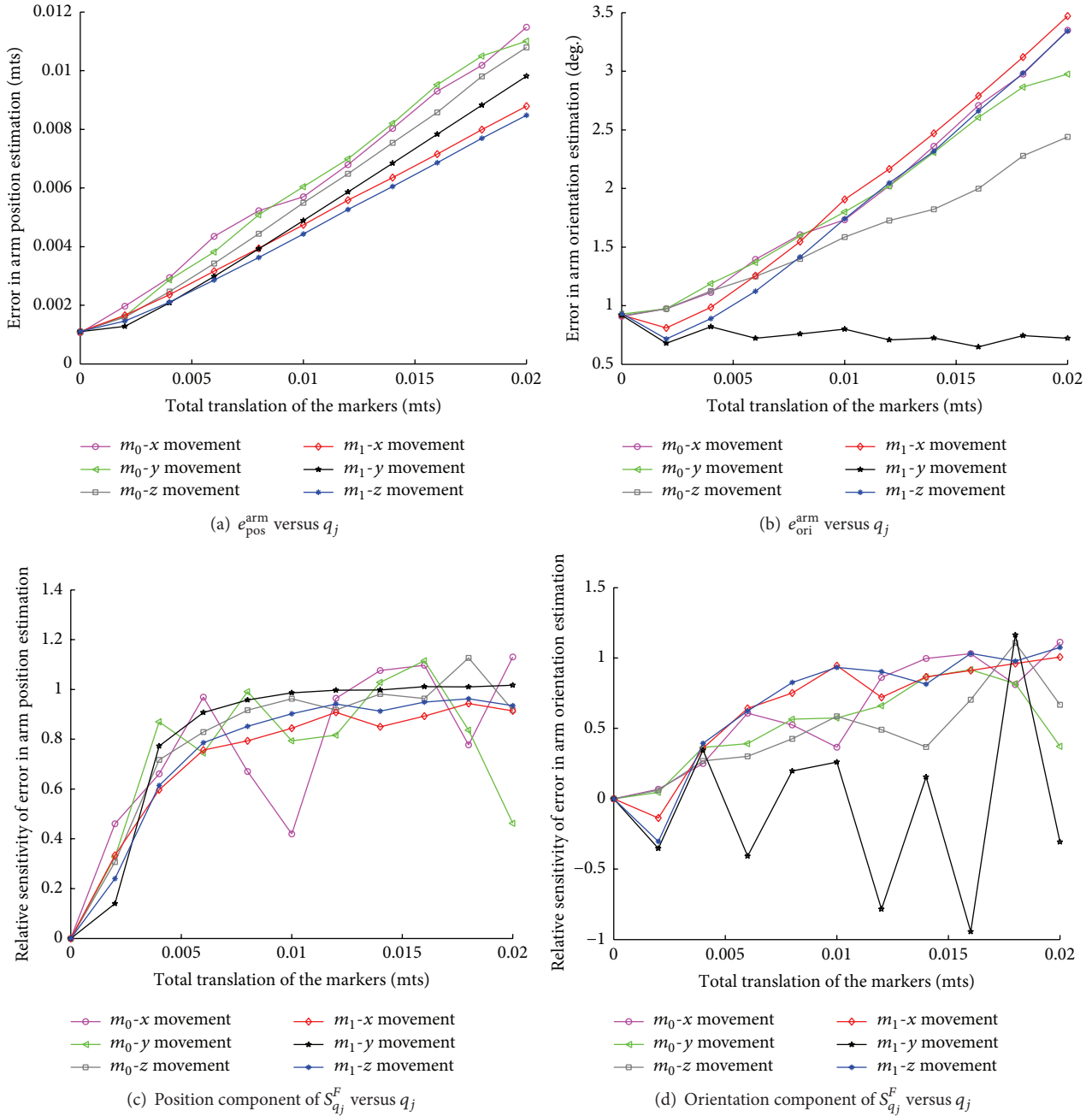


FIGURE 14: Results of the sensitivity analysis with the SAdAd movement dataset ( $q_j$ :  $m_0$ -x movement/ $m_0$ -y movement/ $m_0$ -z movement/ $m_1$ -x movement/ $m_1$ -y movement/ $m_1$ -z movement).

compared to the one produced by translations of  $m_1$ . Note that since  $\tilde{p}_{arm}^E$  is computed by using  $\vec{V}_{arm}$ , any modification in  $\|\vec{V}_{arm}\|$  directly affects the accuracy of  $\tilde{p}_{arm}^E$ .

Observing the behavior of the position component of  $S_{q_j}^F$ , one can conclude that all translations of the markers  $m_0$  and  $m_1$  contribute similarly to the error in the arm position estimation. The curves obtained for the position component of  $S_{q_j}^F$  resemble a logarithmic function with an asymptote along the value 1 of the ordinate axis. A value of 1 in the magnitude of the position component of  $S_{q_j}^F$

means that a percentage change in the magnitude of the marker translation produced the same percentage change (also matching the sign) in the magnitude of the error in the arm position estimation.

4.3.2. *Sensitivity in Arm Orientation Estimation.* In Figures 14, 15, 16, and 17, one can observe that the translations of marker  $m_1$  produce larger absolute errors in the upper arm orientation estimation when compared to those produced by translations of marker  $m_0$ . Notice that the  $x$ -axis and  $z$ -axis of the elbow joint CS are always perpendicular to the upper

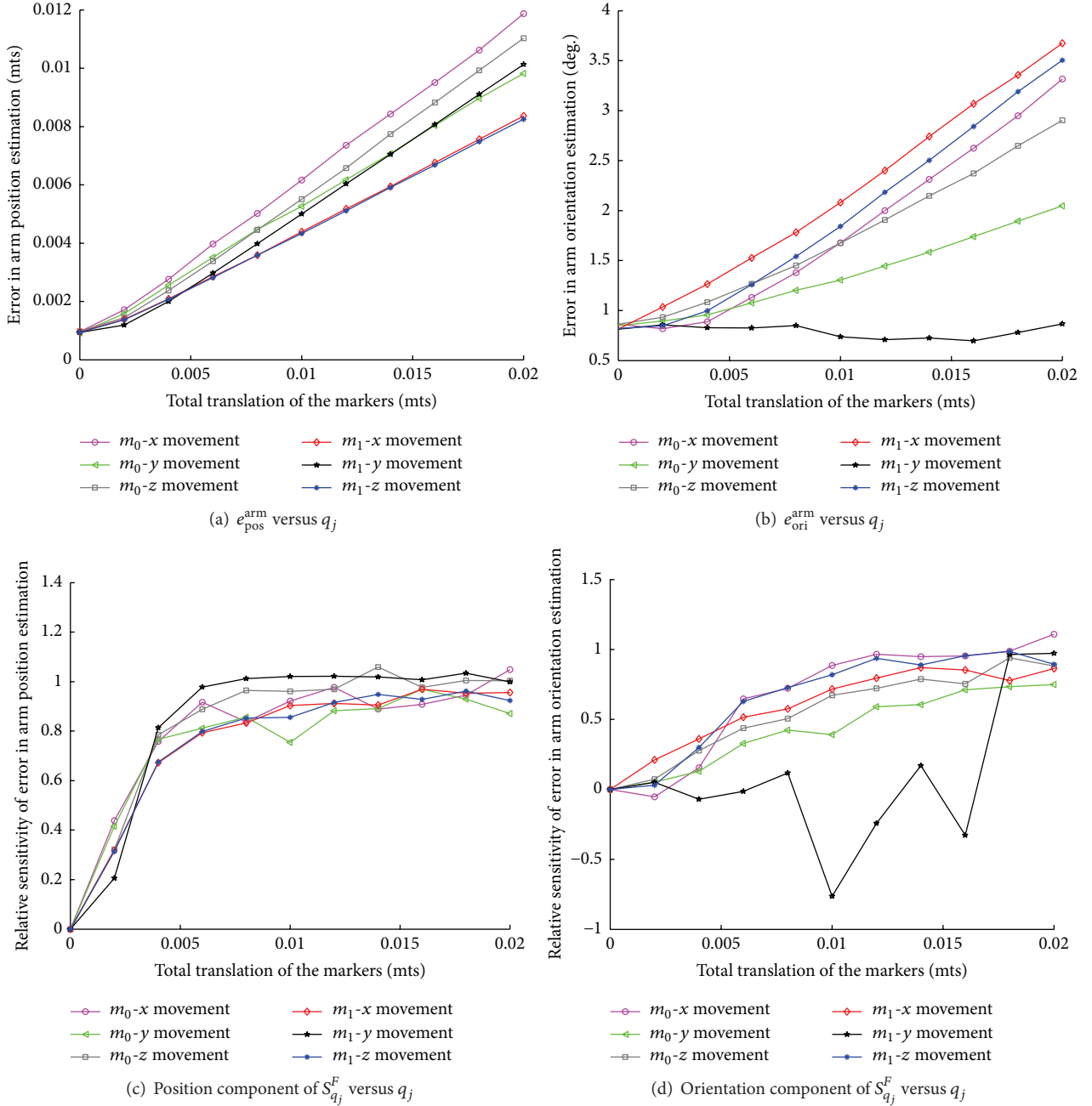


FIGURE 15: Results of the sensitivity analysis with the SFE movement dataset ( $q_j$ :  $m_0$ -x movement/ $m_0$ -y movement/ $m_0$ -z movement/ $m_1$ -x movement/ $m_1$ -y movement/ $m_1$ -z movement).

arm vector ( $\vec{V}_{\text{arm}}$ ) (Figure 12(b)). When the position of  $m_1$  is perturbed along the said axes, the angle between (i) the actual upper arm vector ( $\vec{V}_{\text{arm}}$ ) and (ii) the estimated upper arm vector ( $\vec{\tilde{V}}_{\text{arm}}$ ) (which is inaccurate due to the perturbation of the marker position) is maximal.

A side effect of the marker position perturbation is that the marker  $m_i$  suffers modifications of scale and changes in the level of perspective distortion in the images of camera  $r_i$ , affecting the accuracy of the system. This situation can be observed in Figures 14(b), 15(b), 16(b), and 17(b), where translations of  $m_1$  along the  $y$ -axis of the elbow joint CS

should not produce variations in the orientation estimation error. However, on the contrary, slight variations in the accuracy of the orientation estimation are indeed present in the mentioned figures.

4.3.3. *Robustness of the Upper Arm Pose Estimation Method.* In Figures 14(c), 14(d), 15(c), 15(d), 16(c), 16(d), 17(c), and 17(d) one can observe that the position component of  $S_{q_j}^F$  increases faster than the orientation component of  $S_{q_j}^F$ . The behavior of  $S_{q_j}^F$  observed remains across the datasets used.

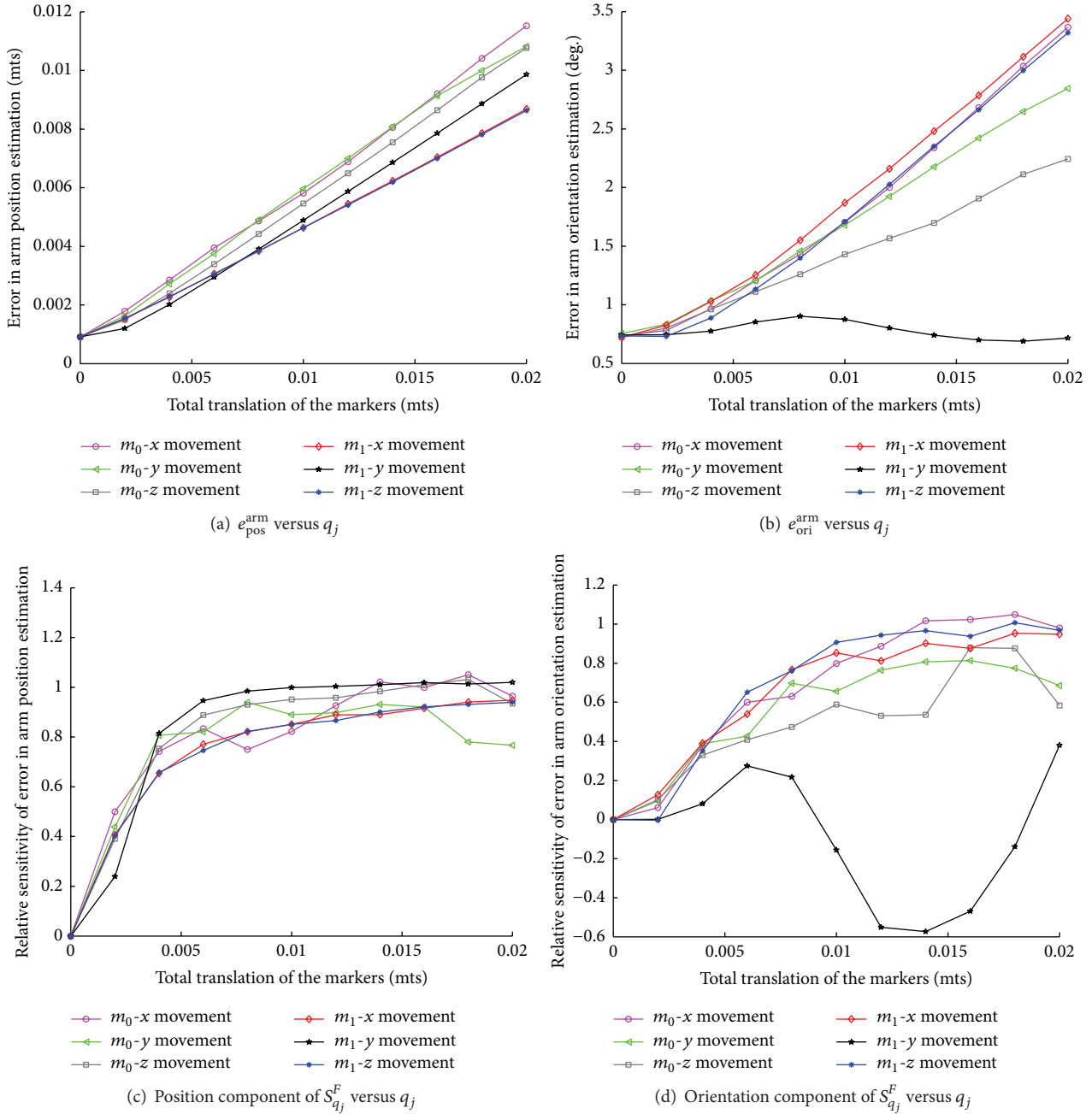


FIGURE 16: Results of the sensitivity analysis with the SIR movement dataset ( $q_j$ :  $m_0$ -x movement/ $m_0$ -y movement/ $m_0$ -z movement/ $m_1$ -x movement/ $m_1$ -y movement/ $m_1$ -z movement).

Hence, the orientation estimation of the upper arm is more robust than the position estimation w.r.t. errors in the translational components of matrices  $T_G^{m_0}$  and  $T_{elw}^{m_1}$ .

The results of the sensitivity analysis show that the assumption that transformations  $T_G^{m_0}$  and  $T_{elw}^{m_1}$  are rigid is reasonable. Even with marker drifts of 0.02 mts, the GH joint angles can be estimated with an accuracy (RMSE 3.6 deg.) appropriate for the mobility evaluation of patients (in the range of 3–5 deg.).

Marker drifts must be mitigated by the marker attachments to the human body. Furthermore, marker attachments

should be designed to minimize the effect of errors in  $T_G^{m_0}$  and  $T_{elw}^{m_1}$  on the method accuracy. For example, notice how the attachment of marker  $m_1$  (Figure 12(b)) locates marker  $m_1$  with an offset w.r.t. the elbow joint center along the direction which least affects the upper arm orientation estimation.

The results presented suggest that the method we implemented is a feasible alternative for estimating the GH joint angles in a RAR scenario.

4.4. Comparison to Related Works. The literature review provided no references other than [16–20] for upper limb

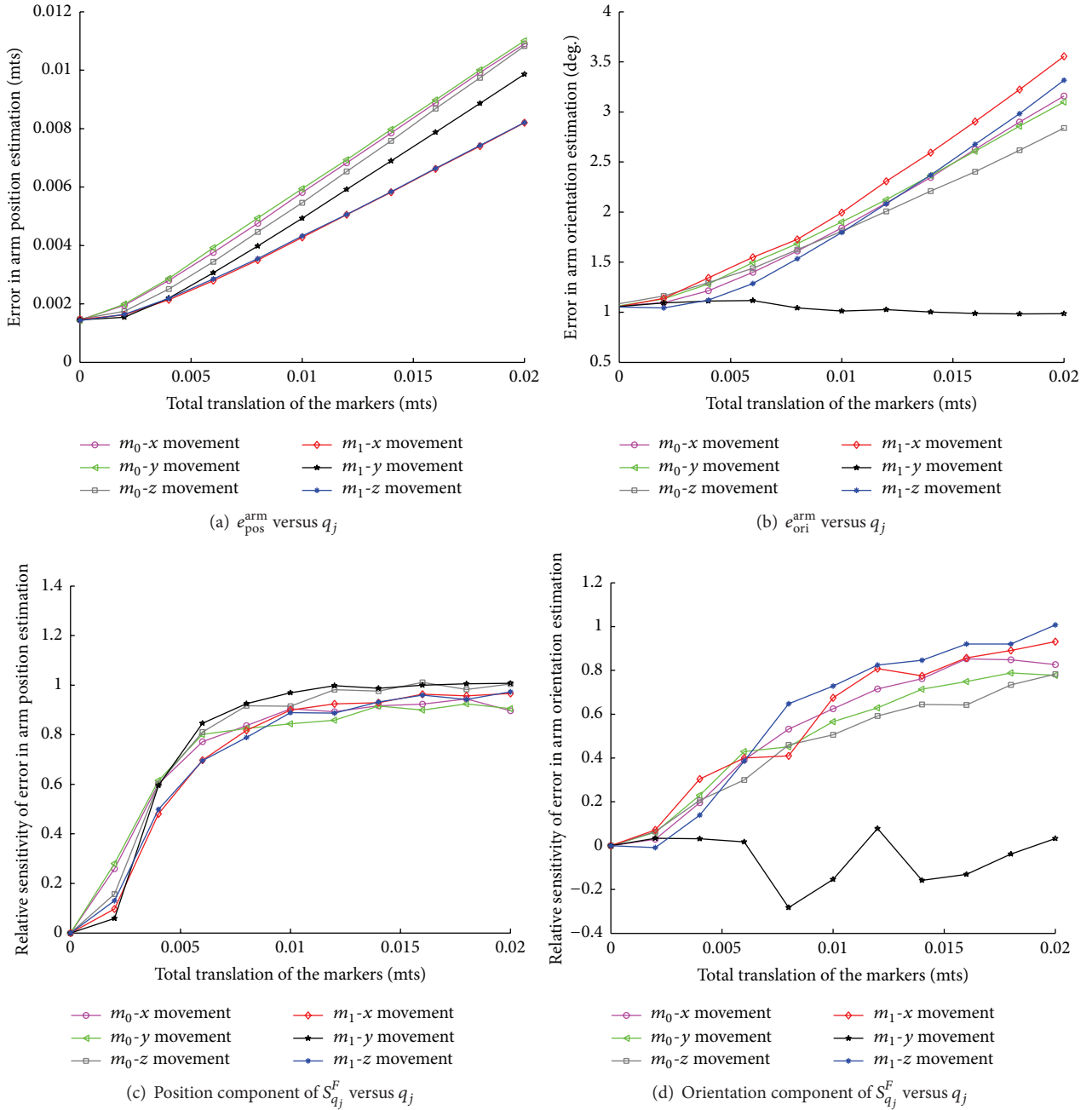


FIGURE 17: Results of the sensitivity analysis with the COMB movement dataset ( $q_j$ :  $m_0$ -x movement/ $m_0$ -y movement/ $m_0$ -z movement/ $m_1$ -x movement/ $m_1$ -y movement/ $m_1$ -z movement).

posture estimation (including the GH joint) in exoskeleton-based rehabilitation using computational methods. Among the mentioned works, only [20] reports the errors (mean RMSE 4.8 deg.) in the GH joint angles estimation. Reference [20] reports RMSE values of the GH joint angles only for the best-case scenario (swivel angle mean RMSE 5 deg.). For all the movement tasks tested, the method in [20] presents a mean RMSE of 10 deg. for the swivel angle estimations. Given that global errors of the swivel angle double those of the best-case scenario, a report of global errors of GH joint angle estimations of the method in [20] is required

to reach a conclusion regarding its suitability for clinical use.

Table 7 summarizes the comparison of our contributions w.r.t. comparable works (i.e., [20]).

## 5. Conclusions and Future Work

In the context of RAR, this paper presents the formulation, implementation, and assessment, in silico, of a novel accurate method to estimate the patient GH joint angles during therapy. Our method does not require redundant markers

TABLE 7: Contributions of this paper w.r.t. comparable works.

Work	Method	Method evaluation	Accuracy of GH joint angles
[20]	IK-based swivel angle estimation	(1) Studied angles: swivel angle plus the shoulder, elbow, and wrist joint angles (2) Reference angles: obtained from custom-made inertial MOCAP; homologation-calibration of the readings is not reported (3) Movements: compound movements (4) Sensitivity analysis: no	Mean RMSE: 4.8 deg. (best-case scenario)
This paper	Hybrid exoskeleton-optical MOCAP	(1) Studied angles: shoulder angles (2) Reference angles: simulated (3) Movements: 1-DOF and multi-DOF shoulder movements (4) Sensitivity analysis: method accuracy w.r.t. marker position errors produced by marker drift or calibration errors	(a) Mean RMSE: 0.9 deg. (assuming no marker drift or calibration errors) (b) Mean RMSE: 3.6 deg. (with marker drift or calibration errors up to 20 mm)

or cameras and relies on simple geometric relationships and tools of standard robotics and computer vision libraries. These characteristics make it economical and readily applicable in RAR.

The accuracy and the robustness of our method are evaluated using computer-generated human movement data corresponding to actual movement datasets of the Armeo Spring. We present a formal sensitivity analysis of the pose estimation accuracy w.r.t. marker position estimation errors produced by (a) system calibration errors and (b) marker drifts (due to skin artifacts). This analysis indicates that even in the presence of large marker position errors our method presents an accuracy that is acceptable for patient mobility appraisal.

Future work includes (a) implementation of the method using commercially available RGB-D vision sensors, (b) evaluation of the method accuracy with actual human movement data, (c) adaptation of the method using solely RGB cameras, and (d) extension of our method to address other limbs.

## Appendix

### Problem Statement

Given. Consider the following:

- (1) A human patient upper body with a kinematic model  $H(L^H, J^H)$  (Figure 2(a)). Consider the following remarks:
  - (a) The model is a simplified version of the spine, arm, and scapuloclavicular systems. However, since we focus on the study of the upper limb, we only describe in detail the kinematic model of the said limb.
  - (b) The set of links is  $L^H = \{l_0^H, \dots, l_{g+1}^H\}$ , containing the sternum, clavicle, upper arm, forearm, and hand ( $g = 4$ ).
  - (c) The set of joints is  $J^H = \{j_0^H, \dots, j_g^H\}$ , containing the sternoclavicular, GH, elbow, and wrist joints.

- (i)  $X_i$  denotes the number of DOFs of  $j_i^H$ .  $X_i = 1, 2$ , or  $3$  ( $i = 0, 1, \dots, g$ ).
  - (ii)  $v_i^H = (\theta_1, \dots, \theta_{X_i})$  is an  $X_i$ -tuple whose  $k$ th component is the angle of the  $k$ th DOF of joint  $i$ th,  $j_i^H$  ( $i = 0, 1, \dots, g$ ).
  - (iii)  $G$  is the index of the GH joint ( $0 \leq G \leq g$ ).  $X_G = 3$  since the GH joint has 3 DOFs.  $v_G^H$  is the 3-tuple containing the values of the DOF of the  $G$  (GH) joint.
  - (iv)  $v_G^H(t)$  registers the status, at time  $t$ , of the DOF of the GH joint.
  - (d)  $H$  is an open kinematic chain, and, therefore,  $l_i^H$  and  $l_{i+1}^H$  are connected by joint  $j_i^H$  ( $i = 0, 1, \dots, g$ ).
- (2) An exoskeleton with a kinematic model  $E(L^E, J^E)$ , which is attached to the patient's limb  $H$  and assists the patient when performing rehabilitation exercises (Figure 2(b)). Consider the following remarks:
    - (a) The set of links is  $L^E = \{l_0^E, \dots, l_{f+1}^E\}$ .
    - (b) The set of joints is  $J^E = \{j_0^E, \dots, j_f^E\}$ .
      - (i)  $Y_i$  denotes the number of DOFs of  $j_i^E$ .
      - (ii)  $v_i^E = (\theta_1, \dots, \theta_{Y_i})$  is a  $Y_i$ -tuple whose  $k$ th component is the angle of the  $k$ th DOF of joint  $i$ th,  $j_i^E$  ( $i = 0, 1, \dots, f$ ).
    - (c)  $E$  is modeled as an open kinematic chain, and, therefore,  $l_i^E$  and  $l_{i+1}^E$  are connected by joint  $j_i^E$  ( $i = 0, 1, \dots, f$ ).
    - (d) The  $v^E$   $b$ -tuple ( $b = \sum_{i=0}^f Y_i$ ) contains the set of independent coordinates which uniquely defines a configuration of  $E$ .
      - (i) Also  $v^E = (v_0^E, \dots, v_i^E, \dots, v_f^E)$ .
      - (ii)  $v^E(t)$  registers the state, at time  $t$ , of the DOF of  $E$ , which is known  $\forall t$ .
    - (e) The exoskeleton may be configured to impose specific motion constraints on the patient by blocking specific joints of the  $J^E$  set.

(3) A marker-based optical tracking system  $R$  composed of two RGB-D cameras and two planar markers (Figure 2(c)). Consider the following remarks:

(a) A set  $M = \{m_0, m_1\}$  of planar markers that are detected by the cameras of  $R$  and are installed on the patient upper limb.

(i) All  $m_i$  present the same 2D square geometry, with a disk in each corner. The position of each disk w.r.t. the marker CS is known. The set of disks is  $K = \{k_0, \dots, k_j, \dots, k_n\}$ .

(A)  $k_j$  presents a color  $s_j \in S$  that can be detected by  $R$  (Figure 2(c)).

(B) The set of colors of the disks mounted on each  $m_i$  is  $S = \{s_0, \dots, s_j, \dots, s_n\}$ . Each  $s_j \in \mathbb{R}^3$  is represented with a RGB color code.

(C)  $s_j \neq s_i \forall i, j \in [0, n] \wedge i \neq j$ .

(ii)  $m_0$  is mounted on the acromion with a 0-DOF coupling (Figure 2(d)). A rigid transformation matrix  $T_G^{m_0}$  defines the relative position and orientation of the GH joint CS w.r.t. the CS of  $m_0$ .

(iii)  $m_1$  is mounted on the upper arm with a 0-DOF coupling (Figure 2(d)). A rigid transformation matrix  $T_{elw}^{m_1}$  defines the relative position and orientation of the elbow joint CS w.r.t. the CS of  $m_1$ . Note that, to compute the GH joint angles, the calculation of the elbow joint angles is not necessary with this setup.

(iv) The rigid transformation matrices  $T_G^{m_0}$  and  $T_{elw}^{m_1} \in \mathbb{R}^{4 \times 4}$  are estimated during the calibration of the system.

(b) A set  $R = \{r_0, r_1\}$  of low-cost cameras is installed in the exoskeleton.

(i)  $r_0$  is mounted on exoskeleton link  $l_0^E$  with a 0-DOF coupling, such that the disks on  $m_0$  are inside its detection volume during the rehabilitation exercises. The rigid transformation matrix  $T_{r_0}^{l_0^E}$  defines the relative position and orientation of the CS of  $r_0$  w.r.t. the  $l_0^E$  CS.

(ii)  $r_1$  is mounted on the exoskeleton link  $l_8^E$  with a 0-DOF coupling, such that it can detect the disks on  $m_1$  (see Figure 2(c)). The rigid transformation matrix  $T_{r_1}^{l_8^E}$  defines the relative position and orientation of the CS of  $r_1$  w.r.t. the  $l_8^E$  CS.

(iii) The rigid transformation matrices  $T_{r_0}^{l_0^E}$  and  $T_{r_1}^{l_8^E} \in \mathbb{R}^{4 \times 4}$  are estimated during system calibration.

(iv) Remarks on each camera  $r_i$  are as follows:

(A)  $r_i$  renders RGB image  $I_i^c$  of  $A \times B$  pixels. The pixel coordinates  $(u, v)$  take values  $0 \leq u \leq A - 1$  and  $0 \leq v \leq B - 1$ .

(B)  $r_i$  renders a depth image associated with the scene in  $I_i^c$ , defined as  $I_i^d$ , of  $L \times N$  pixels;  $L \leq A$  and  $N \leq B$ . The pixel coordinates  $(u, v)$  in  $I_i^d$  take values  $0 \leq u \leq L - 1$  and  $0 \leq v \leq N - 1$ . The CS of images  $I_i^c$  and  $I_i^d$  is coincident.

(C)  $r_i$  presents a truncated square pyramid detection volume parametrized by the minimum and maximum detection distances and the horizontal and vertical field of view of  $r_i$ . Table 1 presents the model features of the vision sensors that have been used for the simulations.

(v) The system of cameras  $R$  produces the following array sequence of each  $r_i$ :

(A)  $C_i (1 \times 3 * A * B)$  contains the RGB color associated with each pixel  $(u, v) \in I_i^c$ .

(B)  $D_i (1 \times L * N * 3)$  contains the  $(X, Y, Z)$  coordinates of the object in each pixel  $(u, v) \in I_i^d$  w.r.t. the  $r_i$  CS.

### Goal

(1) Find the values of  $\tilde{v}_G^H(t) \in \mathbb{R}^3$ , which approximates  $v_G^H(t)$  such that  $e = \|v_G^H(t) - \tilde{v}_G^H(t)\|^2$  is minimum  $\forall t$ .

(a)  $\|x\|$  is the Euclidean norm of vector  $x$ .

### Glossary

Acromion:	Region of the scapula bone above the GH joint
Clavicle:	Bone of the shoulder girdle located at the root of the neck
CS(s):	Coordinate system(s)
COMB:	Combination of movements of the GH joint (SAbAd, SFE, and SIR)
DOF(s):	Degree(s) of freedom
GH:	Glenohumeral
Humerus:	Upper arm bone
MOCAP(s):	Motion capture system(s)
mts:	Meters
RAR:	Robot-Assisted Rehabilitation
RMS:	Root mean square
Scapula:	Bone that connects the humerus to the clavicle
SAbAd:	Shoulder horizontal abduction-adduction
SFE:	Shoulder flexion-extension
SIR:	Shoulder internal rotation
VR:	Virtual Reality
V-REP:	Virtual Robot Experimentation Platform
w.r.t.:	With respect to
$E$ :	Exoskeleton kinematic model
$H$ :	Human upper body kinematic model
$M = \{m_0, m_1\}$ :	Set of planar markers mounted on the patient

$p_G^E$ :	Position of the GH joint w.r.t. the $E$ CS
$p_{elw}^E$ :	Position of the elbow joint w.r.t. the $E$ CS
$R = \{r_0, r_1\}$ :	Set of vision sensors that compose the optical MOCAP
$v_G^H(t)$ :	3-tuple of joint angles of the GH joint at instant $t$
$v^E(t)$ :	Tuple of joint angles of the exoskeleton kinematic model at instant $t$
$T_{m_i}^E$ :	Transformation matrix of marker $m_i$ w.r.t. the $E$ base CS
$T_{m_i}^{r_i}$ :	Transformation matrix of marker $m_i$ w.r.t. the $r_i$ CS
$T_G^{m_0}$ :	Transformation matrix of the GH joint w.r.t. the $m_0$ marker
$T_{elw}^{m_1}$ :	Transformation matrix of the elbow joint w.r.t. the $m_1$ marker
Notation $x_z^y$ :	$x$ can be a position, transformation, and so forth, of object $z$ w.r.t. object $y$ CS.

## Competing Interests

The authors declare that there are no competing interests regarding the publication of this paper.

## Acknowledgments

This research is a part of the HYPER Project funded by CONSOLIDER-INGENIO 2010, Spanish Ministry for Science and Innovation.

## References

- [1] J. Patton, G. Dawe, C. Scharver, F. Mussa-Ivaldi, and R. Kenyon, "Robotics and virtual reality: a perfect marriage for motor control research and rehabilitation," *Assistive Technology*, vol. 18, no. 2, pp. 181–195, 2006.
- [2] M. Guidali, A. Duschau-Wicke, S. Broggi, V. Klamroth-Marganska, T. Nef, and R. Riener, "A robotic system to train activities of daily living in a virtual environment," *Medical and Biological Engineering and Computing*, vol. 49, no. 10, pp. 1213–1223, 2011.
- [3] A. Frisoli, C. Procopio, C. Chisari et al., "Positive effects of robotic exoskeleton training of upper limb reaching movements after stroke," *Journal of NeuroEngineering and Rehabilitation*, vol. 9, no. 1, article no. 36, 2012.
- [4] M. Gilliaux, T. Lejeune, C. Detrembleur, J. Sapin, B. Dehez, and G. Stoquart, "A robotic device as a sensitive quantitative tool to assess upper limb impairments in stroke patients: a preliminary prospective cohort study," *Journal of Rehabilitation Medicine*, vol. 44, no. 3, pp. 210–217, 2012.
- [5] H. Zhou and H. Hu, "Human motion tracking for rehabilitation—a survey," *Biomedical Signal Processing and Control*, vol. 3, no. 1, pp. 1–18, 2008.
- [6] K. Lebel, P. Boissy, M. Hamel, and C. Duval, "Inertial measures of motion for clinical biomechanics: comparative assessment of accuracy under controlled conditions—effect of velocity," *PLoS ONE*, vol. 8, no. 11, Article ID e79945, 2013.
- [7] J. D. Kertis, *Biomechanical evaluation of an optical system for quantitative human motion analysis [M.S. thesis]*, Marquette University, 2012.
- [8] R. Zhu and Z. Zhou, "A real-time articulated human motion tracking using tri-axis inertial/magnetic sensors package," *IEEE Transactions on Neural Systems and Rehabilitation Engineering*, vol. 12, no. 2, pp. 295–302, 2004.
- [9] Y. Tao, H. Hu, and H. Zhou, "Integration of vision and inertial sensors for 3D arm motion tracking in home-based rehabilitation," *International Journal of Robotics Research*, vol. 26, no. 6, pp. 607–624, 2007.
- [10] J. Zariffa, N. Kapadia, J. L. K. Kramer et al., "Relationship between clinical assessments of function and measurements from an upper-limb robotic rehabilitation device in cervical spinal cord injury," *IEEE Transactions on Neural Systems and Rehabilitation Engineering*, vol. 20, no. 3, pp. 341–350, 2012.
- [11] R. Riener and M. Harders, "Virtual reality for rehabilitation," in *Virtual Reality in Medicine*, pp. 161–180, Springer, Berlin, Germany, 2012.
- [12] H. Zhang, S. Balasubramanian, R. Wei et al., "RUPERT closed loop control design," in *Proceedings of the 32nd Annual International Conference of the IEEE Engineering in Medicine and Biology Society (EMBC '10)*, pp. 3686–3689, IEEE, Buenos Aires, Argentina, September 2010.
- [13] S. Kousidou, N. G. Tsagarakis, C. Smith, and D. G. Caldwell, "Task-orientated biofeedback system for the rehabilitation of the upper limb," in *Proceedings of the IEEE 10th International Conference on Rehabilitation Robotics (ICORR '07)*, pp. 376–384, Noordwijk, Netherlands, June 2007.
- [14] N. Nordin, S. Q. Xie, and B. Wünsche, "Assessment of movement quality in robot-assisted upper limb rehabilitation after stroke: a review," *Journal of NeuroEngineering and Rehabilitation*, vol. 11, no. 1, article 137, 2014.
- [15] J. Fong, V. Crocher, D. Oetomo, Y. Tan, and I. Mareels, "Effects of robotic exoskeleton dynamics on joint recruitment in a neurorehabilitation context," in *Proceedings of the 14th IEEE/RAS-EMBS International Conference on Rehabilitation Robotics (ICORR '15)*, pp. 834–839, IEEE, August 2015.
- [16] C. Cortés, A. Ardanza, F. Molina-Rueda et al., "Upper limb posture estimation in robotic and virtual reality-based rehabilitation," *BioMed Research International*, vol. 2014, Article ID 821908, 18 pages, 2014.
- [17] H. Kim and J. Rosen, "Predicting redundancy of a 7 dof upper limb exoskeleton toward improved transparency between human and robot," *Journal of Intelligent & Robotic Systems*, vol. 80, supplement 1, pp. 99–119, 2015.
- [18] H. Kim, L. M. Miller, N. Byl, G. M. Abrams, and J. Rosen, "Redundancy resolution of the human arm and an upper limb exoskeleton," *IEEE Transactions on Biomedical Engineering*, vol. 59, no. 6, pp. 1770–1779, 2012.
- [19] Z. Li, H. Kim, D. Milutinović, and J. Rosen, "Synthesizing redundancy resolution criteria of the human arm posture in reaching movements," in *Redundancy in Robot Manipulators and Multi-Robot Systems*, pp. 201–240, Springer, Berlin, Germany, 2013.
- [20] Q.-C. Wu, X.-S. Wang, and F.-P. Du, "Analytical inverse kinematic resolution of a redundant exoskeleton for upper-limb rehabilitation," *International Journal of Humanoid Robotics*, 2015.
- [21] J. Denavit and R. S. Hartenberg, "A kinematic notation for lower-pair mechanisms based on matrices," *Journal of Applied Mechanics*, vol. 22, pp. 215–221, 1955.

- [22] F. S. Grassia, “Practical parameterization of rotations using the exponential map,” *Journal of Graphics Tools*, vol. 3, no. 3, pp. 29–48, 1998.
- [23] D. Gijbels, I. Lamers, L. Kerkhofs, G. Alders, E. Knippenberg, and P. Feys, “The armeo spring as training tool to improve upper limb functionality in multiple sclerosis: a pilot study,” *Journal of NeuroEngineering and Rehabilitation*, vol. 8, article 5, 2011.
- [24] C. Rudhe, U. Albisser, M. L. Starkey, A. Curt, and M. Bolliger, “Reliability of movement workspace measurements in a passive arm orthosis used in spinal cord injury rehabilitation,” *Journal of NeuroEngineering and Rehabilitation*, vol. 9, article 37, 2012.
- [25] Hocoma AG, “ArmeoR spring—functional arm and hand therapy,” October 2015, <http://www.hocoma.com/products/armeo/armeospring/>.
- [26] M. Caimmi, E. Guanziroli, M. Malosio et al., “Normative data for an instrumental assessment of the upper-limb functionality,” *BioMed Research International*, vol. 2015, article 14, 2015.
- [27] Intel, “Intel realsense developer kit featuring sr 300,” March 2016, <http://click.intel.com/intelrrealsensetm-developer-kit-featuring-sr300.html>.
- [28] Pmdtechnologies Gmbh, Purchase order form, March 2016, [http://pmdtec.com/html/pdf/order\\_camboard\\_pico\\_s.pdf](http://pmdtec.com/html/pdf/order_camboard_pico_s.pdf).
- [29] Softkinetic, “Softkinetic store,” March 2016, <http://www.softkinetic.com/Store/ProductID/36>.
- [30] Softkinetic, “DepthSense cameras,” March 2016, <http://www.softkinetic.com/Products/DepthSenseCameras>.
- [31] Pmdtechnologies Gmbh, Reference design brief camboard picos71.19k, March 2016, [http://pmdtec.com/html/pdf/PMD\\_RD\\_Brief\\_CB\\_pico\\_71.19k\\_V0103.pdf](http://pmdtec.com/html/pdf/PMD_RD_Brief_CB_pico_71.19k_V0103.pdf).
- [32] Coppelia Robotics, “V-rep,” 2015, <http://www.coppeliarobotics.com/>.
- [33] T. F. Edgar, D. M. Himmelblau, and L. S. Lasdon, *Optimization of Chemical Processes*, McGraw-Hill, New York, NY, USA, 2001.
- [34] J. Nocedal and S. Wright, *Numerical Optimization*, Springer Series in Operations Research and Financial Engineering, Springer, New York, NY, USA, 2006.
- [35] A. V. Fiacco, *Introduction to Sensitivity and Stability Analysis in Nonlinear Programming*, Academic Press, 1983.
- [36] A. G. Cutti, A. Giovanardi, L. Rocchi, A. Davalli, and R. Sacchetti, “Ambulatory measurement of shoulder and elbow kinematics through inertial and magnetic sensors,” *Medical & Biological Engineering and Computing*, vol. 46, no. 2, pp. 169–178, 2008.
- [37] K. Lebel, P. Boissy, M. Hamel, and C. Duval, “Inertial measures of motion for clinical biomechanics: comparative assessment of accuracy under controlled conditions—changes in accuracy over time,” *PLoS ONE*, vol. 10, no. 3, Article ID e0118361, 2015.

## Research Article

# The Effect of Mechanical Vibration Stimulation of Perception Subthreshold on the Muscle Force and Muscle Reaction Time of Lower Leg

Huigyun Kim,<sup>1</sup> Kiyoung Kwak,<sup>1</sup> and Dongwook Kim<sup>2,3</sup>

<sup>1</sup>Department of Healthcare Engineering, Graduate School, Chonbuk National University, Jeonju 54896, Republic of Korea

<sup>2</sup>Department of Biomedical Engineering, College of Engineering, Chonbuk National University, Jeonju 54896, Republic of Korea

<sup>3</sup>Research Center of Healthcare and Welfare Instrument for the Aged, Chonbuk National University, Jeonju 54896, Republic of Korea

Correspondence should be addressed to Dongwook Kim; [biomed@jbnu.ac.kr](mailto:biomed@jbnu.ac.kr)

Received 15 January 2016; Accepted 10 May 2016

Academic Editor: Justin Keogh

Copyright © 2016 Huigyun Kim et al. This is an open access article distributed under the Creative Commons Attribution License, which permits unrestricted use, distribution, and reproduction in any medium, provided the original work is properly cited.

The objective of this study is to investigate the effect of mechanical vibration stimulation on the muscle force and muscle reaction time of lower leg according to perception threshold and vibration frequency. A vibration stimulation with perception threshold intensity was applied on the Achilles tendon and tibialis anterior tendon. EMG measurement and analysis system were used to analyze the change of muscle force and muscle reaction time according to perception threshold and vibration frequency. A root-mean-square (RMS) value was extracted using analysis software and Maximum Voluntary Contraction (MVC) and Premotor Time (PMT) were analyzed. The measurement results showed that perception threshold was different from application sites of vibration frequency. Also, the muscle force and muscle reaction time showed difference according to the presence of vibration, frequency, and intensity. This result means that the vibration stimulation causes the change on the muscle force and muscle reaction time and affects the muscles of lower leg by the characteristics of vibration stimulation.

## 1. Introduction

Decreased balance and muscle force with aging cause unstable gait, which often results in falls [1]. Gait is a continuous and repeated movement requiring ability to balance [2]. The ability to balance for gait requires integrated actions of sensory organs, central nerve system, ability to manage exercise, and muscle functions [3]. However, older adults have decreased speed of transferring signals in central nerve system as a response to stimuli for maintaining balance. And weakened muscle force of lower limb decreases the speed, stride, and step frequency and as a result, the risk of falls increases [4]. To prevent falls of the older adults, many studies have been conducted on the improvement of balance and strengthening of muscle force.

Somatosensory vibration stimulation has been proven to decrease the body sway and to increase the postural stability by some studies [5–9]. Eklund reported that the activation of muscles using vibration helped the stability of posture [10].

Also there are some studies that investigated the effect of vibration stimulation on the muscle functions. Curry and Clelland reported that the vibration stimulation increased MVC (Maximum Voluntary Contraction) [11], and Kang et al. reported that the systemic vibration exercise stimulated muscle nerves and shortened the muscle reaction time of the muscles [12].

However, many previous studies used only vibration stimulus with single characteristic and the different characteristics of individual vibration were not taken into consideration. Moreover, Pacinian corpuscle, a sensory receptor responding to vibration stimulation, was reported to respond sensitively at the frequency of 100 Hz–300 Hz [13–15]. However, such frequency range of vibration stimulation was too broad to investigate its effect on the muscle activities. As a result, a previous study was conducted to measure perception threshold to vibration stimulation and to investigate narrower frequency range to which sensory receptors respond more sensitively [16]. From the result of the study, this study will

analyze the effect of vibration on the muscle force and muscle reaction time of lower leg according to perception threshold using MVC and PMT.

## 2. Materials and Methods

**2.1. Subjects.** Ten adult males (age:  $26.9 \pm 1.5$ , height:  $171.2 \text{ cm} \pm 2$ , and weight:  $65.9 \text{ kg} \pm 5.3$ ) participated in this study. The subjects did not have any musculoskeletal diseases and neurological diseases. The subjects did not exercise regularly and have not had experienced special body and vibration exercise. The study was approved by the IRB of Chonbuk National University (IRB File number JBNU 2015-06-012).

**2.2. Equipment.** The small-linear actuator was used to apply vibration. A function generator was used to modify the intensity and frequency of vibration. To fix the small-linear actuator at the Achilles tendon and tibialis anterior tendon, we used rubber band. For EMG measurement, the electrodes (DELSYS Inc., Surface EMG Sensor) were attached on the tibialis anterior muscle and triceps surae and ground electrode was attached on the patella to obtain the muscle force and muscle reaction time. An auditory signal was prepared to measure PMT. The signal and vibration were applied simultaneously.

**2.3. Measurement and Extraction of Muscle Force and Muscle Reaction Time.** To investigate the change of muscle force and muscle reaction time by applying vibration stimulation, the MVC (Maximum Voluntary Contraction) and PMT (Premotor Time) were measured. For this purpose, EMG measurement system (Bagnoli™ Desktop EMG Systems, DELSYS Inc., USA) was used. The MVC is the maximum force which a subject can produce voluntarily. PMT is the time that takes to reach the motor end plate through the cortex of the cerebrum and motor neuron from the point of stimulation. Therefore, PMT refers to the reaction time by nerve element [17]. The subject performed the MVC at the same time as vibration applied and measured the peak value of RMS (root-mean-square) EMG. The subject performed the muscle contraction at the same time as auditory signal. The time to muscle activation start time from the apply point of the auditory signal was extracted from the RMS EMG (Figure 1).

**2.4. Protocol.** In order to investigate the change in the muscle force and muscle reaction time in accordance with the characteristics of the vibration stimulation (frequency, intensity), we made the vibration stimulation conditions. Based on previous studies that investigated vibration perceptible threshold according to vibration frequency, 180 Hz, 190 Hz, and 250 Hz were selected as the vibration stimulation frequency. Likewise, intensity of perception threshold (100%) and subthreshold (80%) was selected as the vibration stimulation intensity [16]. Seven vibration conditions were set by combining nonstimulation, frequency of vibration, and intensity of vibration. With MVC and PMT measured 3 times

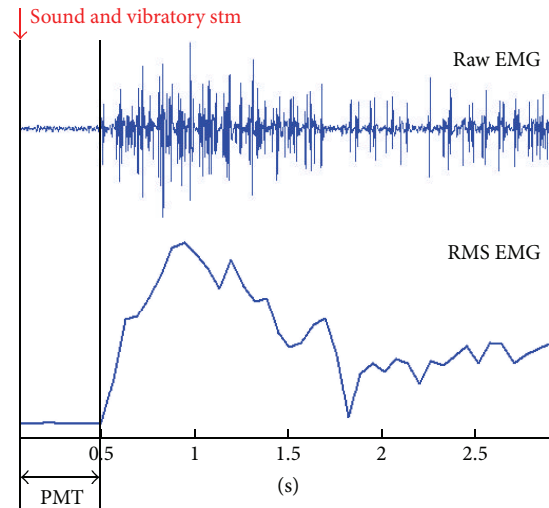


FIGURE 1: PMT extraction example.

in each condition, the stimulation was applied randomly, with 3 minutes of break time after each trial.

**2.5. Data Analysis.** Based on the MVC value of nonstimulation conditions, increase and decrease of change rate of MVC value of vibration stimulation condition were analyzed. PMT was analyzed by the same method. In this study, we conducted statistical analysis on the result using the Wilcoxon Signed Ranks Test of SPSS 18.0. The result was validated at the significance level of  $p < 0.05$ .

## 3. Results

**3.1. Change of Muscle Force according to the Characteristics of Vibration.** The following is the results of MVC according to the vibration stimulation applied to the muscles of the lower leg through the Achilles tendon and the tibialis anterior tendon. Table 1 shows the increase rate of muscle force [%] when the vibration was applied on the Achilles tendon and the tibialis anterior tendon to stimulate triceps surae and tibialis anterior muscle. The increase rate of muscle force [%] was obtained by comparing with the MVC data without stimulation.

Table 1 showed that the muscle force increased with the vibration stimulation for both the triceps surae and tibialis anterior muscle compared without stimulation. The strength of both triceps surae and tibialis anterior muscle significantly increased with the vibration applied on the Achilles tendon (Soleus  $p$  value = 0.022, Lateral Gastrocnemius  $p$  value = 0.049, Medial Gastrocnemius  $p$  value = 0.033, and tibialis anterior  $p$  value = 0.047). The strength of Medial Gastrocnemius muscle significantly increased with the vibration applied on the tibialis anterior tendon (Medial Gastrocnemius  $p$  value = 0.017). The strength of Soleus muscle, Lateral Gastrocnemius muscle, and tibialis anterior muscle increased compared to that without stimulation without showing statistical significance (Soleus  $p$  value =

TABLE 1: The increase rate of muscle force by vibration stimulation applied on the Achilles tendon and tibialis anterior tendon [%].

	Soleus	Lateral Gastrocnemius	Medial Gastrocnemius	Tibialis anterior
Achilles tendon	10.01* ± 7.03	11.97* ± 7.12	14.52* ± 7.99	10.51* ± 7.02
Tibialis anterior tendon	6.53 ± 5.30	9.83 ± 6.43	9.34* ± 5.41	5.74 ± 5.75

\*  $p < 0.05$ . Nonstimulation versus stimulation.

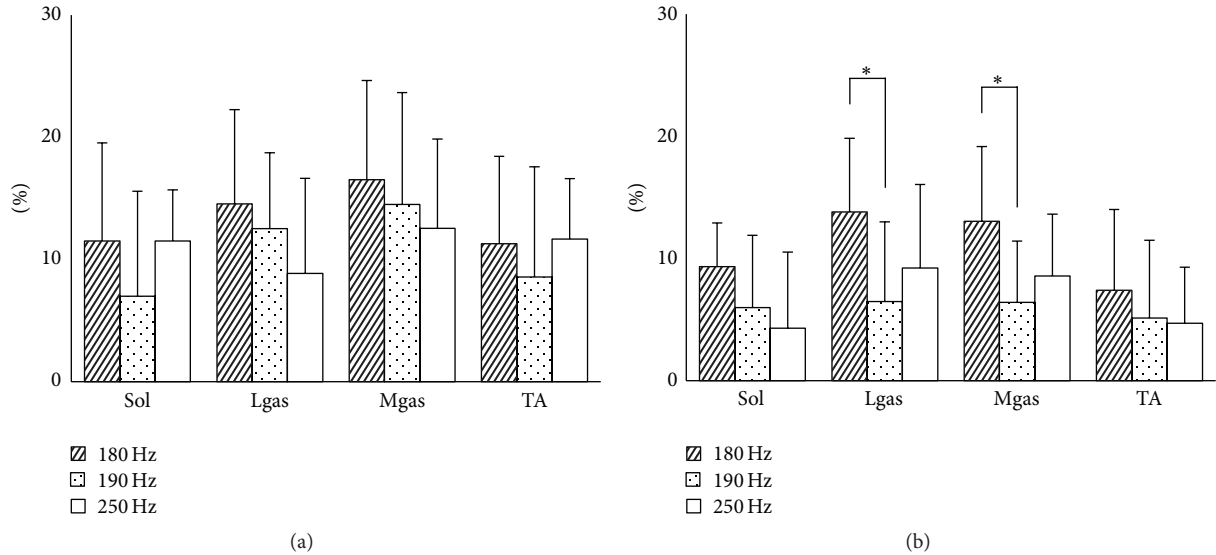


FIGURE 2: The increase rate of muscle force by the vibration frequency applied on the Achilles tendon and tibialis anterior tendon [%] (\*  $p < 0.05$ . 180 Hz versus 190 Hz). (a) Achilles tendon. (b) Tibialis anterior tendon.

0.678, Lateral Gastrocnemius  $p$  value = 0.102, and tibialis anterior  $p$  value = 0.221).

Figures 2(a) and 2(b) show the increase rate of muscle force [%] by the vibration frequency applied on the Achilles tendon and tibialis anterior tendon.

The increase rate of muscle force was the greatest at 12% and 11% with the vibration frequency of 180 Hz and the smallest at 7% and 9% with the frequency of 190 Hz when the vibration was applied on the Soleus muscle and tibialis anterior muscle, respectively (Figure 2(a)). The increase rate of muscle force was the greatest at 15% and 17% with the vibration frequency of 180 Hz and the smallest at 9% and 13% with the frequency of 250 Hz when the vibration was applied on the Lateral Gastrocnemius muscle and Medial Gastrocnemius muscle, respectively. (Figure 2(b)) The increase rate of muscle force was the greatest at 9 and 7% with the vibration frequency of 180 Hz and the smallest at 4 and 5% with the frequency of 250 Hz when the vibration was applied on the Soleus muscle and tibialis anterior muscle, respectively. The increase rate of muscle force was the greatest at 14 and 13% with the vibration frequency of 180 Hz and the smallest at 6 and 6% with the frequency of 190 Hz when the vibration was applied on the Lateral Gastrocnemius muscle and Medial Gastrocnemius muscle, respectively. The increase rate of muscle force was the greatest at the frequency of 180 Hz (Figure 2(b) Lateral Gastrocnemius: 180 Hz–190 Hz  $p$  value = 0.007; Medial Gastrocnemius: 180 Hz–190 Hz  $p$  value = 0.019).

In Table 2, the increase rate of muscle force showed difference by the intensity of vibration, between the intensity of perception threshold (100%) and subthreshold (80%) on the Achilles tendon to stimulate triceps surae and tibialis anterior muscle but the difference was not statistically significant.

In Table 3, the increase rate of muscle force showed difference by the intensity of vibration, between the intensity of perception threshold (100%) and subthreshold (80%) on the Achilles tendon to stimulate triceps surae and tibialis anterior muscle but the difference was not statistically significant.

**3.2. Change in Muscle Reaction Time according to the Characteristics of Vibration.** The following is the results of PMT according to the vibration applied to the muscles of the lower leg through the Achilles tendon and the tibialis anterior tendon. Table 4 shows the muscle reaction time [Sec] when the vibration was applied on the Achilles tendon and the tibialis anterior tendon to stimulate triceps surae and tibialis anterior muscle. The increase rate of muscle force was obtained by comparing the PMT data without stimulation.

Table 4 showed that the muscle reaction time decreased with the vibration stimulation for both the triceps surae and tibialis anterior muscle compared with those without stimulation. The muscle reaction time of both triceps surae and tibialis anterior muscle significantly decreased with the vibration applied on the Achilles tendon (Soleus  $p$  value = 0.005, Lateral Gastrocnemius  $p$  value = 0.009, Medial Gastrocnemius  $p$  value = 0.005, and Tibialis Anterior  $p$  value

TABLE 2: The increase rate of muscle force according to the intensity of vibration, perception threshold (100%) and subthreshold (80%) on the Achilles tendon [%].

		Lower leg muscles								
		Soleus		Lateral Gastrocnemius		Medial Gastrocnemius		Tibialis anterior		
		%	<i>p</i> value	%	<i>p</i> value	%	<i>p</i> value	%	<i>p</i> value	
Achilles tendon	180 Hz	100%	16.04 ± 8.02	0.445	15.43 ± 7.71	0.386	16.25 ± 8.13	0.059	14.29 ± 7.15	0.241
		80%	6.58 ± 12.54		13.11 ± 12.99		10.37 ± 8.43		20.17 ± 17.89	
	190 Hz	100%	17.18 ± 8.59	0.386	12.44 ± 6.22	0.285	18.31 ± 9.16	0.878	18.04 ± 9.02	0.333
		80%	10.9 ± 11.57		17.78 ± 15.3		14.3 ± 10.42		15.8 ± 17.58	
	250 Hz	100%	8.37 ± 4.19	0.594	15.58 ± 7.79	0.285	14.65 ± 7.33	0.878	9.93 ± 4.97	0.139
		80%	14.78 ± 9.43		13.68 ± 19.92		13.5 ± 9.85		18.7 ± 11.39	

TABLE 3: The increase rate of muscle force according to the intensity of vibration, perception threshold (100%) and subthreshold (80%) on the tibialis anterior tendon [%].

		Lower leg muscles								
		Soleus		Lateral Gastrocnemius		Medial Gastrocnemius		Tibialis anterior		
		%	<i>p</i> value	%	<i>p</i> value	%	<i>p</i> value	%	<i>p</i> value	
Tibialis anterior tendon	180 Hz	100%	7.14 ± 3.57	0.799	12.04 ± 6.02	0.386	12.22 ± 6.11	0.575	13.22 ± 6.61	0.878
		80%	9.06 ± 10.75		9.89 ± 7.76		11.06 ± 7.12		8.93 ± 6.52	
	190 Hz	100%	11.84 ± 5.92	0.575	13.06 ± 6.53	0.646	10.04 ± 5.02	0.799	12.74 ± 6.37	0.959
		80%	6.23 ± 13.04		8.15 ± 14.61		5.72 ± 8.52		6.28 ± 5.99	
	250 Hz	100%	12.48 ± 6.24	0.508	13.68 ± 6.84	0.386	10.11 ± 5.06	0.386	9.18 ± 4.59	0.114
		80%	5.82 ± 20.19		15.18 ± 19.52		7.63 ± 8.24		3.11 ± 6.86	

TABLE 4: The muscle reaction time by the vibration stimulation applied to the Achilles tendon and the tibialis anterior tendon [Sec].

	Soleus	Lateral Gastrocnemius	Medial Gastrocnemius	Tibialis anterior
Nonstimulation	0.285* ± 0.060	0.281* ± 0.060	0.262* ± 0.059	0.193* ± 0.072
Achilles tendon stimulation	0.199* ± 0.069	0.203* ± 0.072	0.188* ± 0.071	0.124* ± 0.069
Tibialis anterior tendon stimulation	0.196* ± 0.081	0.198* ± 0.087	0.187* ± 0.087	0.125* ± 0.079

\*  $p < 0.05$ . Nonstimulation versus stimulation.

= 0.009). The muscle reaction time of both triceps surae and tibialis anterior muscle significantly decreased with the vibration applied on the tibialis anterior tendon (Soleus  $p$  value = 0.005, Lateral Gastrocnemius  $p$  value = 0.013, Medial Gastrocnemius  $p$  value = 0.005, and tibialis anterior  $p$  value = 0.012).

Figures 3(a) and 3(b) show the muscle reaction time [Sec] according to the vibration frequency applied on the Achilles tendon and tibialis anterior tendon. The muscle reaction time was significantly shorter with the vibration stimulation on the Achilles tendon at 180 Hz frequency compared with that without stimulation (Figure 3(a)). Moreover, the muscle reaction time at the frequency of 180 Hz was the shortest compared with the other frequencies.

In Table 5, the reaction time showed difference by the intensity of vibration, the intensity of perception threshold (100%) and subthreshold (80%) on the Achilles tendon to stimulate triceps surae and tibialis anterior muscle, but the difference was not statistically significant.

In Table 6, the reaction time showed difference by the intensity of vibration, the intensity of perception threshold (100%) and subthreshold (80%) on the Achilles tendon to

stimulate triceps surae and tibialis anterior muscle, but the difference was not statistically significant.

## 4. Discussion

*4.1. Change of Muscle Force according to the Characteristics of Vibration.* This study analyzed the change of muscle force according to the characteristics of vibration using MVC. The muscle force significantly increased with the vibration stimulation compared to that without any stimulation. This result could be assumed that the vibration applied on the Achilles tendon and tibialis anterior tendon improved the muscle force of the triceps surae and tibialis anterior muscle which, in turn, improve the stability of the lower leg during gait. The vibration stimulation applied on the Achilles tendon rather than the tibialis anterior tendon proved to be more effective, which meant the vibration applied to the Achilles tendon had a greater effect on the muscle force increase. A vibration stimulation with different vibration frequency on the Achilles tendon and tibialis anterior tendon was applied. The results showed that the vibration frequency of 180 Hz had the greatest increase of muscle force for both

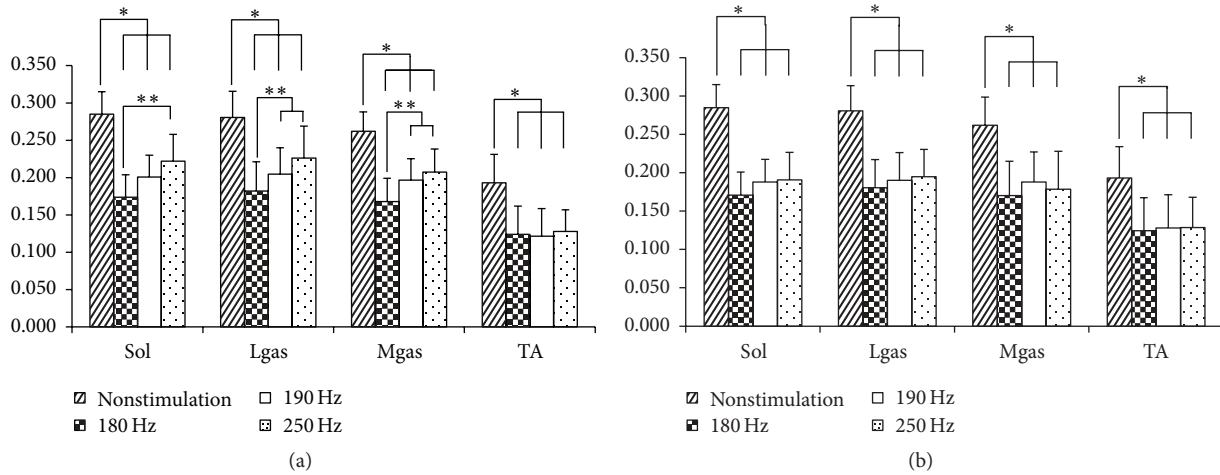


FIGURE 3: The muscle reaction time by the vibration stimulation applied on the Achilles tendon and tibialis anterior tendon according to vibration frequency [Sec] (\*  $p < 0.05$ . nonstimulation versus other frequencies, \*\*  $p < 0.05$ . 180 Hz versus other frequencies). (a) Achilles tendon. (b) Tibialis anterior tendon.

TABLE 5: The muscle reaction time according to the intensity of vibration, perception threshold (100%) and subthreshold (80%) on the Achilles tendon [Sec].

		Lower leg muscles								
		Soleus		Lateral Gastrocnemius		Medial Gastrocnemius		Tibialis anterior		
		Sec	$p$ value	Sec	$p$ value	Sec	$p$ value	Sec	$p$ value	
Achilles tendon	180 Hz	100%	$0.174 \pm 0.038$	0.123	$0.182 \pm 0.038$	0.112	$0.168 \pm 0.037$	0.085	$0.124 \pm 0.029$	0.672
		80%	$0.191 \pm 0.038$		$0.194 \pm 0.041$		$0.182 \pm 0.039$		$0.124 \pm 0.037$	
	190 Hz	100%	$0.201 \pm 0.026$	0.905	$0.205 \pm 0.031$	0.858	$0.197 \pm 0.029$	0.406	$0.122 \pm 0.031$	0.293
		80%	$0.208 \pm 0.036$		$0.210 \pm 0.034$		$0.191 \pm 0.035$		$0.115 \pm 0.033$	
	250 Hz	100%	$0.222 \pm 0.035$	0.176	$0.226 \pm 0.039$	0.176	$0.207 \pm 0.035$	0.236	$0.128 \pm 0.043$	0.676
		80%	$0.201 \pm 0.033$		$0.201 \pm 0.034$		$0.180 \pm 0.038$		$0.132 \pm 0.034$	

the Achilles tendon and tibialis anterior tendon. It could be assumed that the change of muscle force is dependent on the frequency from this result. The vibration stimulation with the intensity of perception threshold and subthreshold (80%) was applied on the Achilles tendon and tibialis anterior tendon. The results showed that the increase rate of muscle force was different from the vibration intensity when the vibration stimulation was applied on the triceps surae and tibialis anterior muscle via the Achilles tendon. The increase rate of muscle force was also different from the vibration intensity when the vibration stimulation was applied on the triceps surae and tibialis anterior muscle via the tibialis anterior tendon. However, the difference was not statistically significant for both the Achilles tendon and tibialis anterior tendon stimulation. This result means that the vibration with the intensity of perception threshold and subthreshold affects the muscle force at the same extent.

4.2. Change in Muscle Reaction Time according to the Characteristics of Vibration. The change on the muscle reaction time according to the characteristics of vibration was analyzed using PMT. The muscle reaction time significantly decreased with the vibration stimulation compared to that without any stimulation. From this result, the vibration stimulation

applied to the muscles of the lower leg shortened the muscle reaction time from the sensory system, CNS to the muscular system. In other words, this result could be assumed that the efficiency in transmitting/processing nerve impulses improved. A vibration stimulation with different vibration frequency on the Achilles tendon and tibialis anterior tendon was applied. The results showed that the muscle reaction time was significantly shorter at the frequency of 180 Hz for both the Achilles tendon and tibialis anterior tendon stimulation compared to those of other frequencies. It means that the reaction time is dependent on the vibration frequency. The vibration stimulation with the intensity of perception threshold and subthreshold (80%) was applied on the Achilles tendon and tibialis anterior tendon. The results showed that the muscle reaction time was different from the intensity but statistically insignificant. The results mean that the vibration with the intensity of perception threshold and subthreshold equally affects the muscle reaction time.

### 5. Conclusion

This study investigated the effect of mechanical vibration stimulation applied on the Achilles tendon and tibialis anterior tendon according to the characteristics of vibration

TABLE 6: The muscle reaction time according to the intensity of vibration, perception threshold (100%) and subthreshold (80%) on the tibialis anterior tendon [Sec].

		Lower leg muscles								
		Soleus		Lateral Gastrocnemius		Medial Gastrocnemius		Tibialis anterior		
		Sec	<i>p</i> value	Sec	<i>p</i> value	Sec	<i>p</i> value	sec	<i>p</i> value	
Tibialis anterior tendon	180 Hz	100%	0.171 ± 0.033	0.859	0.181 ± 0.036	0.574	0.170 ± 0.036	0.944	0.124 ± 0.036	0.071
		80%	0.204 ± 0.051		0.203 ± 0.052		0.189 ± 0.054		0.107 ± 0.028	
	190 Hz	100%	0.188 ± 0.037	0.549	0.190 ± 0.045	0.513	0.188 ± 0.039	0.959	0.128 ± 0.049	0.302
		80%	0.191 ± 0.043		0.197 ± 0.046		0.191 ± 0.044		0.118 ± 0.038	
	250 Hz	100%	0.191 ± 0.041	0.514	0.195 ± 0.043	0.476	0.178 ± 0.043	0.906	0.128 ± 0.040	0.291
		80%	0.203 ± 0.039		0.207 ± 0.039		0.188 ± 0.045		0.143 ± 0.047	

including the presence of vibration, frequency, and intensity on the muscles of the lower leg and the following results were obtained. The change of muscle force and muscle reaction time according to the characteristics of vibration showed that both improved with the vibration stimulation compared to those without any stimulation. The frequency of 180 Hz showed the best results and the changes of muscle force and reaction time were dependent on the vibration frequency. The effect of vibration with the intensity of perception threshold and subthreshold on the muscle force and muscle reaction time was the same. In conclusion, a local tendon stimulation using vibration of 180 Hz frequency and perception subthreshold intensity would improve the muscle force and muscle reaction time and contribute the stability of the lower leg during gait.

## Competing Interests

The authors declare that there is no conflict of interests regarding the publication of this paper.

## Acknowledgments

This work was supported by the Research Foundation of Korea (NRF) grant funded by the Korea government (MSIP) (NRF-2014R1A2A1A11053073) and research funds of Chonbuk National University in 2015.

## References

- [1] M. E. Tinetti, S. K. Inouye, T. M. Gill, and J. T. Doucette, "Shared risk factors for falls, incontinence, and functional dependence: unifying the approach to geriatric syndromes," *The Journal of the American Medical Association*, vol. 273, no. 17, pp. 1348–1353, 1995.
- [2] J. P. Perry, *Gait Analysis: Normal and Pathological Function*, SIACK, Downey, Calif, USA, 1992.
- [3] J. O. Judge, "Balance training to maintain mobility and prevent disability," *American Journal of Preventive Medicine*, vol. 25, no. 3, pp. 150–156, 2003.
- [4] D. M. Buchner, E. B. Larson, E. H. Wagner, T. D. Koepsell, and B. J. De Lateur, "Evidence for a non-linear relationship between leg strength and gait speed," *Age and Ageing*, vol. 25, no. 5, pp. 386–391, 1996.
- [5] H. Issever, C. Aksoy, H. Sabuncu, and A. Karan, "Vibration and its effects on the body," *Medical Principles and Practice*, vol. 12, no. 1, pp. 34–38, 2003.
- [6] H. J. So, K. Y. Kim, S. H. Kim, N. G. Kim, and D. W. Kim, "The Analysis of GRF and joint angles of young and older adult by vibration stimulation on the ankle-joint in stair-descent activity," *Journal of Biomedical Engineering Research*, vol. 32, no. 1, pp. 61–73, 2011.
- [7] K. Kwak, H. So, S. Kim, Y. Yang, N. Kim, and D. Kim, "Effects of somatosensory stimulation on lower-limb joint kinetic of older adult during stair descent," *Journal of Biomedical Engineering Research*, vol. 32, no. 2, pp. 93–104, 2011.
- [8] D. C. Gravelle, C. A. Laughton, N. T. Dhruv et al., "Noise-enhanced balance control in older adults," *NeuroReport*, vol. 13, no. 15, pp. 1853–1856, 2002.
- [9] R. Dickstein, Y. Laufer, and M. Katz, "TENS to the posterior aspect of the legs decreases postural sway during stance," *Neuroscience Letters*, vol. 393, no. 1, pp. 51–55, 2006.
- [10] G. Eklund, "General features of vibration-induced effects on balance," *Upsala Journal of Medical Sciences*, vol. 77, no. 2, pp. 112–124, 1972.
- [11] E. L. Curry and J. A. Clelland, "Effects of the asymmetric tonic neck reflex and high-frequency muscle vibration on isometric wrist extension strength in normal adults," *Physical Therapy*, vol. 61, no. 4, pp. 487–495, 1981.
- [12] S. R. Kang, G. Y. Jeong, J. J. Bae et al., "Effect of muscle function and muscular reaction of knee joint in the twenties on the whole body vibration exercise," *Journal of the Korean Society for Precision Engineering*, vol. 30, no. 7, pp. 762–768, 2013.
- [13] O. Handy and M. Volker, *Vibration Thresholds and Equal Vibration Levels at the Human Fingertip and Palm*, ICA, Kyoto, Japan, 2004.
- [14] A. Picu, "Study about evaluation of human exposure to hand-transmitted vibration," *Journal of Science and Arts*, vol. 2, pp. 355–360, 2010.
- [15] T. Sakurai, M. Konyo, S. Okamoto, and S. Tadokoro, "Research of conditions of stimulus for inducing grasping force control reflex," in *Proceedings of the IEEE/SICE International Symposium on System Integration (SII '10)*, pp. 408–413, Sendai, Japan, December 2010.
- [16] K. Kwak, H. Kim, and D. Kim, "Variation of ankle biomechanical property according to vibro-perception threshold and

vibration frequency," *Biomedical Engineering Letters*, vol. 6, no. 1, pp. 16–25, 2016.

- [17] J.-W. Kim, H.-Y. Jeong, H.-H. Kim et al., "Comparison of reaction times of ankle joint muscles in the elderly men and women," *Journal of Biomedical Engineering Research*, vol. 33, no. 4, pp. 163–168, 2012.

## Research Article

# Robust Sliding Mode Control Based on GA Optimization and CMAC Compensation for Lower Limb Exoskeleton

Yi Long, Zhi-jiang Du, Wei-dong Wang, and Wei Dong

State Key Laboratory of Robotics and System, Harbin Institute of Technology, Harbin 150001, China

Correspondence should be addressed to Wei Dong; [dongwei@hit.edu.cn](mailto:dongwei@hit.edu.cn)

Received 16 January 2016; Accepted 17 February 2016

Academic Editor: Huapeng Wu

Copyright © 2016 Yi Long et al. This is an open access article distributed under the Creative Commons Attribution License, which permits unrestricted use, distribution, and reproduction in any medium, provided the original work is properly cited.

A lower limb assistive exoskeleton is designed to help operators walk or carry payloads. The exoskeleton is required to shadow human motion intent accurately and compliantly to prevent incoordination. If the user's intention is estimated accurately, a precise position control strategy will improve collaboration between the user and the exoskeleton. In this paper, a hybrid position control scheme, combining sliding mode control (SMC) with a cerebellar model articulation controller (CMAC) neural network, is proposed to control the exoskeleton to react appropriately to human motion intent. A genetic algorithm (GA) is utilized to determine the optimal sliding surface and the sliding control law to improve performance of SMC. The proposed control strategy (SMC\_GA\_CMAC) is compared with three other types of approaches, that is, conventional SMC without optimization, optimal SMC with GA (SMC\_GA), and SMC with CMAC compensation (SMC\_CMAC), all of which are employed to track the desired joint angular position which is deduced from Clinical Gait Analysis (CGA) data. Position tracking performance is investigated with cosimulation using ADAMS and MATLAB/SIMULINK in two cases, of which the first case is without disturbances while the second case is with a bounded disturbance. The cosimulation results show the effectiveness of the proposed control strategy which can be employed in similar exoskeleton systems.

## 1. Introduction

The lower extremity exoskeleton, which began in the late 1960s, is an electromechanical structure worn by human users as an intelligent device for performance assistance and enhancement. In recent years, wearable robots have attracted interests of many researchers widely. The Berkeley Lower Extremity Exoskeleton (BLEEX) was designed to assist people in walking for carrying load, which could walk at the speed of 0.9 m/s while carrying 34 kg payload [1]. A mechanical leg has seven DOFs (three at the hip, one at the knee, and three at the ankle), of which four DOFs are actuated by valve-based hydraulic actuation systems [2]. However, these many active DOFs make the system complex and heavy, weighing 38 kg. The latter exoskeletons, that is, ExoHiker, ExoClimber, and HULC, simplify mechanical structure and reduce the number of active DOFs while carrying more payloads up to 68 kg–90 kg [3]. Hybrid Assistive Limb (HAL), proposed by the University of Tsukuba in Japan, has two active DOFs at the hip joint and knee joint, which are controlled according to

collected electrical signals from muscles [4]. HAL is used to help users carry load and assist disabled people in walking [5, 6]. An underactuated exoskeleton system is designed based on appropriate criteria to help infantry soldiers walk on different terrain, where active joints are applied to the knee joints while other joints are passive [7]. Moreno et al. studied and analyzed the human interaction with wearable lower limb exoskeleton, where the robot gathered information from the sensors in order to detect human actions and subjects also modified their gait patterns to obtain the desired responses from the exoskeleton [8].

Although many kinds of lower limb exoskeleton robots are studied, the human-exoskeleton collaborative movement is quite complex and difficult due to nonlinear characteristics of dynamic model and uncertainties, for example, external disturbance and involuntary movements. To achieve the goal of making exoskeletons providing assistance for human beings, a consistent dynamic tracking performance is required to maneuver exoskeletons in an efficient, smooth, and continuous manner [9]. The control procedure can be

divided into two steps, acquiring human motion intent with human-robot interaction (HRI) and following the human motion intent accurately.

When the wearer wants to move, the central controller sends control signals to enforce the exoskeleton to follow commanded signals, during which HRI decreases. A crucial issue of control is to follow the estimated human motion intent accurately. The more accurate the intention tracking is, the more compliantly the exoskeleton works. The precise motion control of robotic manipulators has received considerable attention from many robotics researchers and its challenges continue to limit overall control performance because of structured and unstructured uncertainties [10]. In exoskeletons, the structured uncertainties contain payload variations, while unstructured uncertainties contain sensor noises, joint friction, and external disturbances. There are many approaches for position control approaches to deal with uncertainties such as robust control [11, 12], adaptive control [13, 14], intelligent control [15], and sliding mode control [16].

SMC is a robust control approach that drives state trajectory to predefined sliding surface by using discontinuous control inputs [17], which is used to improve control performance for robotic manipulators with model uncertainties such as parameter perturbations, unknown joint frictions and inertias, and external disturbances [18]. It is notable that its overall performance is superior to general PID control algorithm [19]. The process of designing a SMC controller has two steps: defining suitable sliding surfaces and designing discontinuous control laws [13]. Parameters of SMC should be chosen suitably to obtain optimal performance. Some common optimization methods are provided and applied in robots, for example, GA [20], particle swarm optimization (PSO) [21], ant colony optimization (ACO) [22], and evolutionary algorithm (EA) [23]. GA is simple to be implemented and is capable of locating global optimal solutions [24], which is utilized to optimize the structure of intelligent methods [25, 26]. The decoupled SMC as a supervisory controller is applied in accordance with PID control, whose parameters are tuned using GA, to enhance tracking performance and eliminate the chattering problem [27]. The gain switch and sliding surface constant parameters are selected by GA so that the designed SMC can achieve satisfactory performance [28]. However, GA is only used to optimize parameters of sliding surfaces or SMC control laws. In this work, we use GA to optimize all parameters of the sliding surface and the control law at the same time.

The optimal SMC can deal with uncertainties to achieve satisfactory performance. To improve tracking performance, CMAC is added as a compensation item with property of fast learning capability. The CMAC proposed first by Albus [29] is similar to the mode of human cerebellum, which is an autoassociative memory feed-forward neural network. Compared with other feed-forward neural networks, it has faster convergence speed [30]. The approach which uses CMAC as a compensation item with SMC is applied in position control of robotic manipulators [31]. In this work, we propose to combine optimal SMC using GA and CMAC compensation to form the hybrid position control strategy.

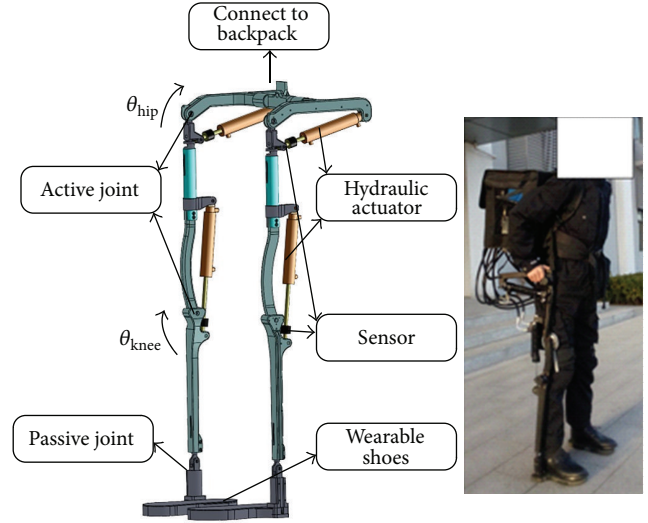


FIGURE 1: Prototype of lower limb powered exoskeleton. There are two active joints of each leg in walking direction, which are represented as  $\theta_{hip}$  and  $\theta_{knee}$ . All auxiliary facilities are packaged in the backpack.

The remainder of this paper is organized as follows. The specific system under study is given in the second section. In Section 3, the proposed control strategy is explained in details. Cosimulations using the proposed approach and results analysis are presented in the fourth section. Conclusions are drawn in the final section.

## 2. Problem Formulations

**2.1. Exoskeleton Configuration.** Based on principles in biological design, the designed exoskeleton is required to retain adaptability to multifunctionality of human lower limbs. An available powerful tool when designing an assistive exoskeleton is the enormous Clinical Gait Analysis (CGA) data on human walking [32]. With CGA data [33], our designed exoskeleton is shown in Figure 1. As Figure 1 shows, there are two active joints of a single leg in sagittal plane, which are knee joint and hip joint actuated by hydraulic actuation system.

**2.2. Mathematical Model of Exoskeleton.** For multirigid system, Euler-Lagrange is a frequently used method for modeling of robotic manipulators. The exoskeleton is a typical human-robot collaboration system, which includes the user's lower limbs and mechanical limbs which are tied together at the interaction cuffs. Mathematical model of a single leg of exoskeleton is obtained because of its symmetry structure. Without loss of generality, the dynamic equation of the swing leg of exoskeleton robot can be expressed as follows:

$$\mathbf{M}(\mathbf{q}) \ddot{\mathbf{q}} + \mathbf{C}(\mathbf{q}, \dot{\mathbf{q}}) \dot{\mathbf{q}} + \mathbf{G}(\mathbf{q}) + \mathbf{D} = \mathbf{T}, \quad (1)$$

where  $\mathbf{M}(\mathbf{q}) \in R^{n \times n}$  is the symmetric definite inertial matrix;  $\mathbf{C}(\mathbf{q}, \dot{\mathbf{q}}) \in R^{n \times n}$  is the Coriolis and centrifugal force matrix;  $\mathbf{G}(\mathbf{q}) \in R^{n \times 1}$  is the gravitational force matrix;  $\mathbf{T} \in R^{n \times 1}$

is the control input vector;  $\mathbf{D} \in R^{n \times 1}$  denotes unmodeled dynamics and external disturbances.

For dynamics model in (1), several properties are presented as the following [34].

*Property 1.* Matrix  $\mathbf{M}(\mathbf{q})$  is symmetric and positive definite.

*Property 2.* Matrix  $\dot{\mathbf{M}}(\mathbf{q}) - 2\mathbf{C}(q, \dot{q})$  is a skew-symmetric matrix if  $\forall \varepsilon \in R^n, \varepsilon^T(\dot{\mathbf{M}}(\mathbf{q}) - 2\mathbf{C}(q, \dot{q}))\varepsilon = 0$ .

*Property 3.* There exist finite scalars  $\delta_i > 0, i = 1, \dots, 4$  such that  $\|\mathbf{M}(\mathbf{q})\| \leq \delta_1, \|\mathbf{C}(\mathbf{q}, \dot{\mathbf{q}})\| \leq \delta_2, \|\mathbf{G}(\mathbf{q})\| \leq \delta_3$ , and  $\|D\| \leq \delta_4$ , which means all items in dynamic model are bounded.

In the position control of robotic manipulators, we define trajectory tracking error as

$$\mathbf{e} = \mathbf{q}_d - \mathbf{q}, \quad (2)$$

where  $\mathbf{e}$  is the tracking error,  $\mathbf{q}_d$  is reference trajectory, and  $\mathbf{q}$  is actual trajectory. Based on (2), we can obtain

$$\begin{aligned} \dot{\mathbf{e}} &= \dot{\mathbf{q}}_d - \dot{\mathbf{q}}, \\ \ddot{\mathbf{e}} &= \ddot{\mathbf{q}}_d - \ddot{\mathbf{q}}, \end{aligned} \quad (3)$$

where  $\dot{\mathbf{e}}$  and  $\ddot{\mathbf{e}}$  is the first and second derivative of  $\mathbf{e}$ ,  $\dot{\mathbf{q}}_d$  and  $\ddot{\mathbf{q}}_d$  are angular velocity and acceleration vector of command input, and  $\dot{\mathbf{q}}$  and  $\ddot{\mathbf{q}}$  are that of actual output, respectively, all of which are bounded.

### 3. Control Strategy Design

*3.1. Sliding Mode Control.* A general SMC design consists of two steps: the sliding surface design and the control law construction. The purpose of the SMC is to track the trajectory specified by human intention and maintain system trajectory in the sliding surfaces [18]. Considering that there exist uncertainties including unmodeled frictions, variation of parameters, and external disturbances, the robustness should be an important concern in the controller design for exoskeleton system. The general sliding surface is defined as  $\mathbf{s} = \dot{\mathbf{e}} + \mathbf{A}\mathbf{e}$ . To improve robustness of controller, a designed integral sliding surface is represented as follows [35]:

$$\mathbf{s} = \dot{\mathbf{e}} + \mathbf{A}\mathbf{e} + \mathbf{H} \int_0^{ts} \mathbf{e} dt, \quad (4)$$

where  $\mathbf{A}$  and  $\mathbf{H}$  are positive definite matrix. Then  $\dot{\mathbf{s}}$  can be derived:

$$\dot{\mathbf{s}} = \ddot{\mathbf{e}} + \mathbf{A}\dot{\mathbf{e}} + \mathbf{H}\mathbf{e}. \quad (5)$$

As the second design stage of SMC, the control laws should be chosen, which should be satisfied with the existence condition of SMC [36]:

$$\mathbf{s}^T \dot{\mathbf{s}} < 0. \quad (6)$$

For the exoskeleton system under study, we define the SMC control law as follows:

$$\begin{aligned} \mathbf{u} &= \mathbf{M}(q) \ddot{\mathbf{q}}_d - (\mathbf{T}_d - \mathbf{C}(q, \dot{q}) \dot{\mathbf{q}}) + \mathbf{M}(q) \mathbf{A}\dot{\mathbf{e}} \\ &+ \mathbf{M}(q) \mathbf{H}\mathbf{e} + \mathbf{C}(q, \dot{q}) \mathbf{s} + \varepsilon \operatorname{sgn}(\mathbf{s}) + \mathbf{K}\mathbf{s}, \end{aligned} \quad (7)$$

where  $\mathbf{T}_d = \mathbf{D} - \mathbf{G}(\mathbf{q})$ ,  $\varepsilon$  and  $\mathbf{K}$  are positive definite matrices, and  $\operatorname{sgn}(\mathbf{s})$  is a symbolic function which is shown as follows:

$$\operatorname{sgn}(\mathbf{s}) = \begin{cases} 1, & \mathbf{s} > 0, \\ 0, & \mathbf{s} = 0, \\ -1, & \mathbf{s} < 0. \end{cases} \quad (8)$$

The SMC algorithm has chattering phenomena, which affects the accuracy of position control much. In order to eliminate chattering, the continuous function  $\theta(\mathbf{s})$  with relay characteristics is used to replace the function of symbolic function  $\operatorname{sgn}(\mathbf{s})$  to restrict the trajectory in a boundary layer of ideal sliding mode [37]. Then (7) can be rewritten as

$$\begin{aligned} \mathbf{u} &= \mathbf{M}(q) \ddot{\mathbf{q}}_d - (\mathbf{T}_d - \mathbf{C}(q, \dot{q}) \dot{\mathbf{q}}) + \mathbf{M}(q) \mathbf{A}\dot{\mathbf{e}} \\ &+ \mathbf{M}(q) \mathbf{H}\mathbf{e} + \mathbf{C}(q, \dot{q}) \mathbf{s} + \varepsilon \theta(\mathbf{s}) + \mathbf{K}\mathbf{s}, \end{aligned} \quad (9)$$

where  $\theta(\mathbf{s}) = \mathbf{s}/(\|\mathbf{s}\| + \sigma)$ ,  $\sigma > 0$ . Before stability analysis, *Barbalat lemma* is shown as the following [38].

**Barbalat Lemma.** *If a differentiable function  $f(t)$  has a limit as  $t \rightarrow \infty$ , and if  $\dot{f}(t)$  is uniformly continuous, then  $f(t) \rightarrow 0$  as  $t \rightarrow \infty$ .*

**Theorem 1.** *The proposed controller (9) guarantees asymptotic convergence to zero, both of the trajectory tracking errors and sliding surfaces. Namely, the system is globally stable; that is, when  $t \rightarrow \infty, e \rightarrow 0, s \rightarrow 0$ .*

*Proof.* Lyapunov function is defined as

$$\mathbf{V} = \frac{1}{2} \mathbf{s}^T \mathbf{M}(q) \mathbf{s}. \quad (10)$$

Differentiating  $\mathbf{V}$  with respect to time yields

$$\dot{\mathbf{V}} = \mathbf{s}^T \mathbf{M}(q) \dot{\mathbf{s}} + \frac{1}{2} \mathbf{s}^T \dot{\mathbf{M}}(q) \mathbf{s}. \quad (11)$$

Considering Property 2, then

$$\mathbf{s}^T \left( \frac{1}{2} \dot{\mathbf{M}}(q) - \mathbf{C}(q, \dot{q}) \right) \mathbf{s} = 0. \quad (12)$$

Combining (10)–(12), one can get

$$\begin{aligned} \dot{\mathbf{V}} &= \mathbf{s}^T (\mathbf{M}(q) \dot{\mathbf{s}} + \mathbf{C}(q, \dot{q}) \mathbf{s}) = \mathbf{s}^T (\mathbf{M}(q) (\ddot{\mathbf{q}}_d - \ddot{\mathbf{q}}) \\ &+ \mathbf{M}(q) \mathbf{A}\dot{\mathbf{e}} + \mathbf{M}(q) \mathbf{H}\mathbf{e} + \mathbf{C}(q, \dot{q}) \mathbf{s}). \end{aligned} \quad (13)$$

And  $\ddot{\mathbf{q}}$  can be solved by

$$\ddot{\mathbf{q}} = \mathbf{M}(q)^{-1} (\mathbf{T} + \mathbf{T}_d - \mathbf{C}(q, \dot{q}) \dot{\mathbf{q}}). \quad (14)$$

Substituting (14) into (13), then

$$\begin{aligned} \dot{\mathbf{V}} &= \mathbf{s}^T (\mathbf{M}(q) \ddot{\mathbf{q}}_d - (\mathbf{T} + \mathbf{T}_d - \mathbf{C}(q, \dot{q}) \dot{\mathbf{q}}) + \mathbf{M}(q) \mathbf{A}\dot{\mathbf{e}} \\ &+ \mathbf{M}(q) \mathbf{H}\mathbf{e} + \mathbf{C}(q, \dot{q}) \mathbf{s}). \end{aligned} \quad (15)$$

Substituting (7) into (15), we can obtain

$$\dot{\mathbf{V}} = \mathbf{s}^T (-\boldsymbol{\varepsilon}\theta(\mathbf{s}) - \mathbf{K}\mathbf{s}). \quad (16)$$

It is easy to know that  $\mathbf{K}$  and  $\boldsymbol{\varepsilon}$  are positive definite matrices; therefore  $\mathbf{s}^T \mathbf{K}\mathbf{s} > 0$ ,  $\mathbf{s}^T \theta(\mathbf{s}) > 0$ ; then  $\dot{\mathbf{V}} < 0$ . Hence, the system is globally stable. With the *Barbalat lemma*,  $\mathbf{s} \rightarrow 0$  as  $t \rightarrow \infty$ ; then one knows  $\mathbf{e} \rightarrow 0$  and  $\dot{\mathbf{e}} \rightarrow 0$  as  $t \rightarrow \infty$ . This control law could realize convergence of the trajectory tracking error to zero.  $\square$

**3.2. Genetic Algorithm.** In SMC, those constant parameters existing in sliding surfaces and control laws, which are  $\mathbf{A}$ ,  $\mathbf{H}$ ,  $\mathbf{K}$ , and  $\boldsymbol{\varepsilon}$  in (9), determine the overall performance. Hence, it is necessary to find the optimal values of them using optimization algorithm. GA is an adaptive heuristic search algorithm that mimics the process of natural selection and uses biological evolution to develop a series of search space points toward an optimal solution. There are five components that are required to implement GA: representation, initialization, fitness function, genetic operators, and genetic parameters [39].

A simple GA involves three types of operator: selection, crossover, and mutation [40]. Selection is a probabilistic process for selecting chromosomes in the population using their fitness values. The chromosome with larger fitness value is likely to be selected to reproduce. Crossover is the process of randomly choosing a locus and swaps the characters either left or right of this locus between two chromosomes to create two offspring. The probability of crossover occurring for the parent chromosomes is usually set to a large value (e.g., 0.8). Mutation is to randomly flip some of the bits by changing “0” to “1” or vice versa, with a small probability (e.g., 0.001) which maintains genetic diversity to guarantee that GA can come to better solution. The process of GA optimization is shown in Figure 2. As Figure 2 shows, there are parameters such as the size of population and generation and the length of code that should be initialized; then the process of selection, crossover, and mutation is preceded until the convergence conditions are satisfied.

**3.3. SMC with GA Optimization.** Based on that discussed above, the fitness function should be confirmed before implementing GA to SMC. The goal of SMC is to achieve precise trajectory tracking for robotic manipulators; that is, the smaller the trajectory errors are, the more effective the controller is. Those parameters to be optimized are relevant to trajectory error; hence the fitness function is defined as follows:

$$J(\mathbf{A}, \mathbf{H}, \mathbf{K}, \boldsymbol{\varepsilon}) = \sum_{k=0}^{\infty} \|\mathbf{e}(k)\|^2. \quad (17)$$

With the fitness function, those parameters can be found with the minimization of tracking errors during the trajectory tracking using the designed control law. In the search space of GA, the SMC will have optimal parameters when the fitness function has minimum values. The algorithm of SMC optimized by GA is shown as Algorithm 1 in Appendix A.

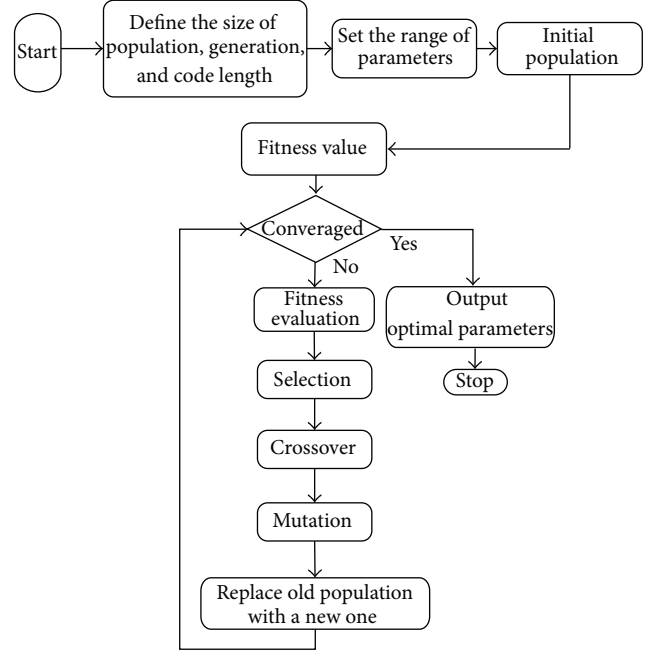


FIGURE 2: The process of GA optimization, when the convergence condition is satisfied, the optimal parameters will be obtained.

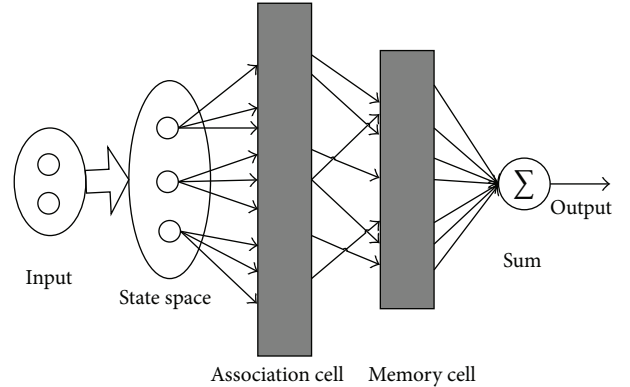


FIGURE 3: Structure of CMAC neural network.

**3.4. CMAC Neural Network.** The CMAC neural network has three steps: projecting an input into association area, compressing memory cell through Hash coding, and calculating the output as a scalar product of the memory area [41], which is shown in Figure 3. The output of CMAC can be expressed as follows [42]:

$$\begin{aligned} \mathbf{y}_s &= \mathbf{C}_s^T \mathbf{H} \mathbf{W} \\ &= [c_{s,1} \ c_{s,2} \ \cdots \ c_{s,N_h}] \begin{bmatrix} h_{1,1} & \cdots & h_{1,M_p} \\ \vdots & & \vdots \\ h_{N_h,1} & \cdots & h_{N_h,M_p} \end{bmatrix} \begin{bmatrix} \omega_1 \\ \omega_2 \\ \vdots \\ \omega_{M_p} \end{bmatrix}, \quad (18) \end{aligned}$$

```

G = 200, Size = 30, CodeL = 10, parameters definition
input vector  $X_k = [q_{hd}(k), q_{kd}(k)]^T$ , the length of optimized parameters Len = 8
initialize population  $E = \text{round}(\text{rand}(\text{Size}, \text{Siez} * \text{CodeL}))$ 
for  $g = 1, 2, \dots, G$  do
  for  $s = 1, 2, \dots, \text{Size}$  do
    for  $l = 1, 2, \dots, \text{Len}$  do
       $F(s, l) = (\text{Max}(l) - \text{Min}(l)) * \text{Code}(j)/1023 + \text{Min}(l)$ ;  $F(s, l)$  will be used for fitness
    end for
  end for
  Selection and reproduction
  sort the fitness value and obtain the sequence number index
  for  $s = 1, 2, \dots, \text{Size}$  do
     $\text{TempE}(jj, :) = E(\text{index}(i), :)$ ;  $jj = jj + 1$ 
  end for
  Crossover and select the probability  $p_c = 0.8$ 
  for  $s = 1, 2, \dots, \text{Size}$  do
    temp = rand
    If  $p_c > \text{temp}$  do
      for  $t = 1, 1, \dots, \text{Num}$  do
         $\text{TempE}(s, t) = E(s + 1, t)$ 
         $\text{TempE}(s + 1, t) = E(s, t)$ 
      end for
    end if
  end for
  Mutation and select the probability
   $p_m = 0.001 - [1 : 1 : \text{Size}] * (0.001)/\text{Size}$ , temp = rand
  for  $s = 1, 2, \dots, \text{Size}$  do
    for  $j = 1, 2, \dots, \text{Len}$  do
      if  $p_m > \text{temp}$  do
        if  $\text{TempE}(s, j) == 0$  do
           $\text{TempE}(s, j) = 1$ 
        else
           $\text{TempE}(s, j) = 0$ 
        end if
      end if
    end for
  end for
  replace old generation with new one
end for
Obtain optimal parameters

```

ALGORITHM 1: Optimize SMC with GA. (Notation:  $q_{hd}(k)$  and  $q_{kd}(k)$  represent desired trajectory of hip joint and knee joint, resp.)

where  $\mathbf{C}_s$  is an association vector projected by input vector,  $\mathbf{W}$  is the weight vector,  $\mathbf{H}$  is the matrix of Hash coding,  $\mathbf{M}_p$  is the number of Hash vector,  $N_h$  is the number of association vector, and  $h_{ij} = 1$  represents  $i$ th association unit response to  $j$ th Hash unit.

Similar to other neural networks, the weight parameters should be updated using Least Square Method (LSM). The updating process is expressed as follows:

$$\Delta \mathbf{W} = \frac{\eta}{N_h} \mathbf{A}_{s-1} (\hat{\mathbf{y}}_{s-1} - \mathbf{A}_{s-1}^T \mathbf{W}_{s-1}), \quad (19)$$

$$\mathbf{W}(k+1) = \mathbf{W}(k) + \Delta \mathbf{W} + \alpha (\mathbf{W}(k+1) - \mathbf{W}(k)),$$

where  $\Delta \mathbf{W}$  is the weight vector increment,  $\eta$  is the learning rate,  $\mathbf{A}_{s-1}^T = \mathbf{C}_{s-1}^T \mathbf{H}$ ,  $\hat{\mathbf{y}}_{s-1}$  is the target output, and  $\alpha$  is the inertial parameter.

CMAC was originally proposed to be applied into control problems by Miller III et al. [43]. The CMAC control loop is usually added to traditional control loops, where the traditional controller actuates the plant stably and the CMAC helps to improve control preciseness without affecting the traditional control loop [44, 45]. In other words, the CMAC control is usually added as a compensation item of traditional control method. The algorithm of the hybrid control strategy combining SMC and CMAC is shown as Algorithm 2 in Appendix B.

3.5. *Combination of GA Optimization-Based SMC and CMAC Neural Network.* Based on discussion above, we can combine SMC, GA, and CMAC neural network into a hybrid control strategy, which is called SMC.GA.CMAC.

```

input vector  $s = [s_1, s_2]$ , determine the range of  $s$  as  $s_{\max 1}, s_{\min 1}, s_{\max 2}, s_{\min 2}$ 
initialize CMAC, the range of quantization  $M$ , storage of association  $N$ , storage of memory  $C$ 
Input quantization:
 $s_1 = \text{round}((s_1 - s_{\min 1}) * M / (s_{\max 1} - s_{\min 1})), s_2 = \text{round}((s_2 - s_{\min 2}) * M / (s_{\max 2} - s_{\min 2}))$ 
Hash coding and obtain output of CMAC
for  $k = 1, 2, \dots, C$  do
     $\text{add}_1 = \text{mod}(s_1 + k, N) + 1, \text{add}_2 = \text{mod}(s_2 + k, N) + 1$ 
     $\text{Sum}_1 = w_1(\text{add}_1(k), \text{add}_2(k)), \text{Sum}_2 = w_2(\text{add}_2(k), \text{add}_2(k))$ 
end for
Weight update
for  $i = 1, 2, \dots, C$  do
    for  $j = 1, 2, \dots, C$  do
         $dw_1(i, j) = \eta e_1 / C, dw_2(i, j) = \eta e_2 / C$ 
    end for
end for
 $w_1 = w_{1,1} + dw_1 + \alpha(w_{1,1} - w_{1,2}), w_2 = w_{2,1} + dw_2 + \alpha(w_{2,1} - w_{2,2})$ 
 $w_{1,2} = w_{1,1}, w_{1,1} = w_1, w_{2,2} = w_{2,1}, w_{2,1} = w_2$ 

```

ALGORITHM 2: The process of CMAC neural network. (Notation: the input is sliding surface and the output is the compensation control vector.)

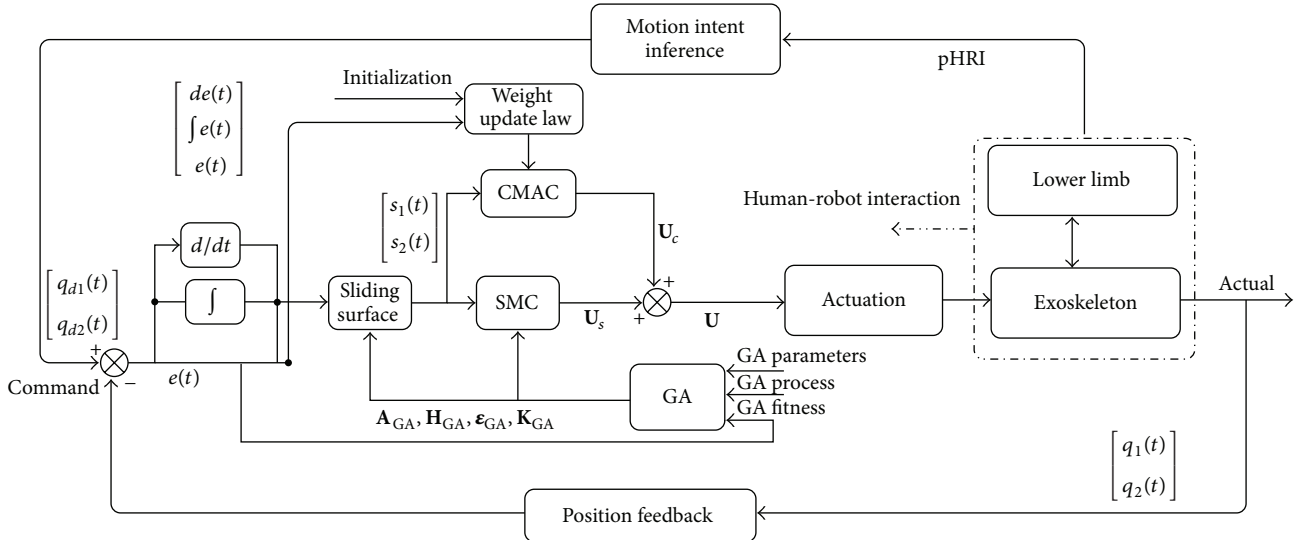


FIGURE 4: The control diagram of the proposed method for the exoskeleton system.

We can write the proposed control law based on (9) as follows:

$$\begin{aligned}
 \mathbf{u} = & \mathbf{K}_c \mathbf{U}_c + \mathbf{M}(q) \ddot{\mathbf{q}}_d - (\mathbf{T}_d - \mathbf{C}(q, \dot{q}) \dot{\mathbf{q}}) \\
 & + \mathbf{M}(q) \mathbf{A}_{GA} \dot{\mathbf{e}} + \mathbf{M}(q) \mathbf{H}_{GA} \mathbf{e} + \mathbf{C}(q, \dot{q}) \mathbf{s} \\
 & + \boldsymbol{\varepsilon}_{GA} \theta(\mathbf{s}) + \mathbf{K}_{GA} \mathbf{s},
 \end{aligned} \quad (20)$$

where  $\mathbf{U}_c$  represents the output of CMAC neural network,  $\mathbf{K}_c \in \mathbb{R}^{n \times 1}$  is a positive definite matrix, and  $\mathbf{A}_{GA}$ ,  $\mathbf{H}_{GA}$ ,  $\boldsymbol{\varepsilon}_{GA}$ , and  $\mathbf{K}_{GA}$  are matrices optimized using GA. With the reaching condition (6), the output of CMAC  $\mathbf{U}_c$  has constraint as the following:

$$\mathbf{U}_c = \begin{cases} \mathbf{U}_c, & \text{if } \mathbf{s}^T \mathbf{U}_c \geq 0, \\ -\mathbf{U}_c, & \text{if } \mathbf{s}^T \mathbf{U}_c < 0. \end{cases} \quad (21)$$

For the exoskeleton system, the control diagram is illustrated as Figure 4 shows. As Figure 4 shows, GA is employed to obtain the optimal parameters  $\mathbf{A}_{GA}$ ,  $\mathbf{K}_{GA}$ ,  $\mathbf{H}_{GA}$ , and  $\boldsymbol{\varepsilon}_{GA}$  to construct optimized SMC. The CMAC's input is the sliding surface and its weight updating is derived from minimizing the tracking error. The output of the proposed control law is  $\mathbf{U} = \mathbf{U}_s + \mathbf{K}_c \mathbf{U}_c$ , of which  $\mathbf{U}_s$  is the main output provided by SMC. GA and  $\mathbf{U}_c$  is the compensation output provided by CMAC.

#### 4. Simulations with the Proposed Control Strategy

In this section, the proposed method is examined through simulations. The simulation results, which are from

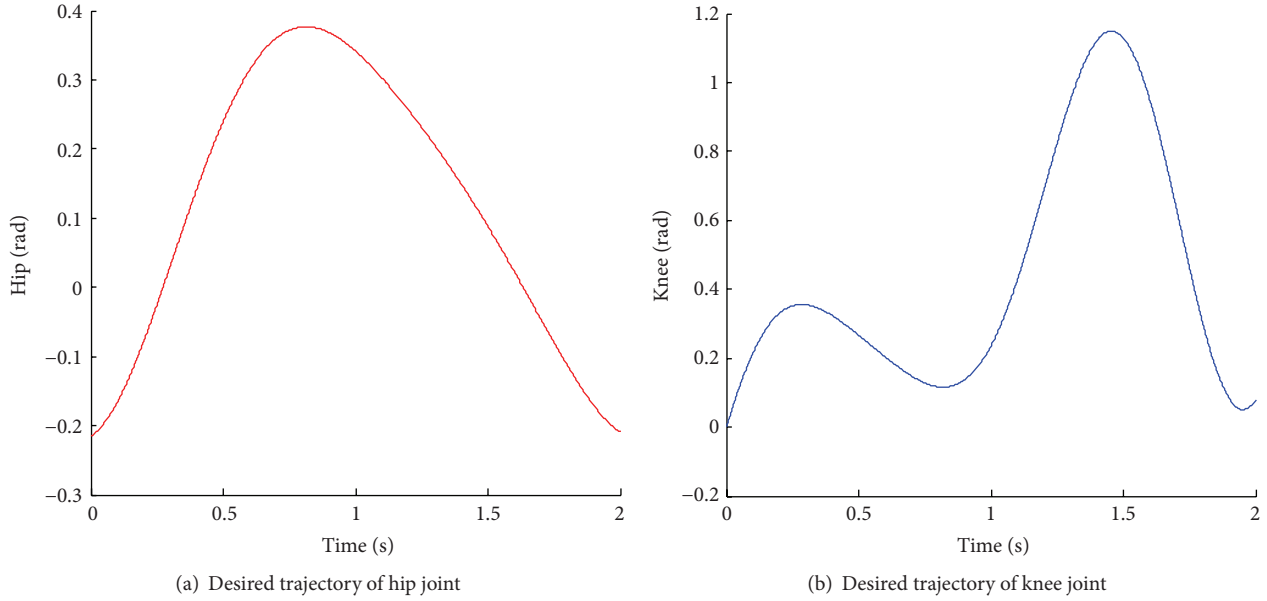


FIGURE 5: The desired joint trajectory of human lower limb movement. The initial posture is in the vertical direction.

application into controlling the swing leg of the exoskeleton using the proposed algorithms, are presented. As Figure 1 shows, the active DOFs are hip joint and knee joint, while the ankle joint is passive. Based on (1), the dynamics model of swing leg can be expressed as

$$\mathbf{M}(q)_{\text{exo}} \ddot{\mathbf{q}} + \mathbf{C}(q, \dot{q})_{\text{exo}} \dot{\mathbf{q}} + \mathbf{G}(q)_{\text{exo}} = \mathbf{T}, \quad (22)$$

where  $\mathbf{M}(q)_{\text{exo}} \in \mathbb{R}^{2 \times 2}$ ,  $\mathbf{C}(q, \dot{q})_{\text{exo}} \in \mathbb{R}^{2 \times 2}$ ,  $\mathbf{G}(q)_{\text{exo}} \in \mathbb{R}^{2 \times 1}$ ,  $\ddot{\mathbf{q}} \in \mathbb{R}^{2 \times 1}$ ,  $\dot{\mathbf{q}} \in \mathbb{R}^{2 \times 1}$ , and  $\mathbf{T} \in \mathbb{R}^{2 \times 1}$ . In simulations, the desired angular position of lower limb joints stems from the CGA data as Figure 5 shows. The period of the cyclical gait is 2 seconds and we will obtain the fitting expression with respect to time

$$\begin{aligned} q_{\text{hip}}(t) &= 3.85 \cos(0.330t + 2.14) \\ &\quad + 71.6 \cos(3.49t - 1.88) \\ &\quad + 41.0 \cos(4.68t - 0.3), \\ q_{\text{knee}}(t) &= 40.9 \cos(1.04t - 0.208) \\ &\quad + 157 \cos(5.82 - 0.047) \\ &\quad + 82.3 \cos(7.49t - 4.13), \end{aligned} \quad (23)$$

where  $q_{\text{hip}}(t)$  and  $q_{\text{knee}}(t)$  are the desired angular position of hip joint and knee joint, respectively.

To investigate the effectiveness and robustness of the proposed scheme, two simulation cases are considered: without disturbances (Case One) and with bounded disturbances (Case Two). The external disturbance  $D(t)$  is a function of time which is assumed to have an upper bound:

$$D(t) = a \sin(\pi t), \quad \|a\| \leq 1. \quad (24)$$

For recording the respective performances, the root mean square error (RSME) is defined to examine control performance as follows:

$$\text{RSME} = \sqrt{\frac{\sum_{k=1}^N \|e(k)\|^2}{N}}, \quad (25)$$

where  $N$  is the size of error vector. We integrate ADAMS and MATLAB/SIMULINK to control the exoskeleton using the proposed control strategy, which is shown in Figure 6. As Figure 6 shows, there are six output variables from ADAMS model which are angular position, velocity, and acceleration of knee joint and hip joint of a swing leg while the designed controller in MATLAB outputs two control torques into ADAMS model. Figure 6(a) shows the exoskeleton model in ADAMS and Figure 6(b) shows the control scheme in SIMULINK. The designed controller produces control signals transferred to ADAMS while the kinematics information of exoskeleton joints is measured in ADAMS and returned back to MATLAB workspace. Through creating a communication block between MATLAB and ADAMS, the dynamics movements in gait cycles are shown in Figure 7, which illustrates the level ground walking for the lower extremity exoskeleton.

The comparisons between the proposed control scheme and conventional SMC, SMC with CMAC (SMC\_CMAC) neural network, and optimal SMC with GA (SMC\_GA) are conducted. The simulated comparisons, containing tracking positions and tracking errors of SMC, SMC\_GA, SMC\_CMAC, and SMC\_GA\_CMAC in Case One and Case Two, are depicted in Figures 8 and 9. As Figure 8 shows, Figures 8(a) and 8(c) represent the joint trajectory tracking of hip joint and knee joint while Figures 8(b) and 8(d) show tracking error comparisons of those two joints using

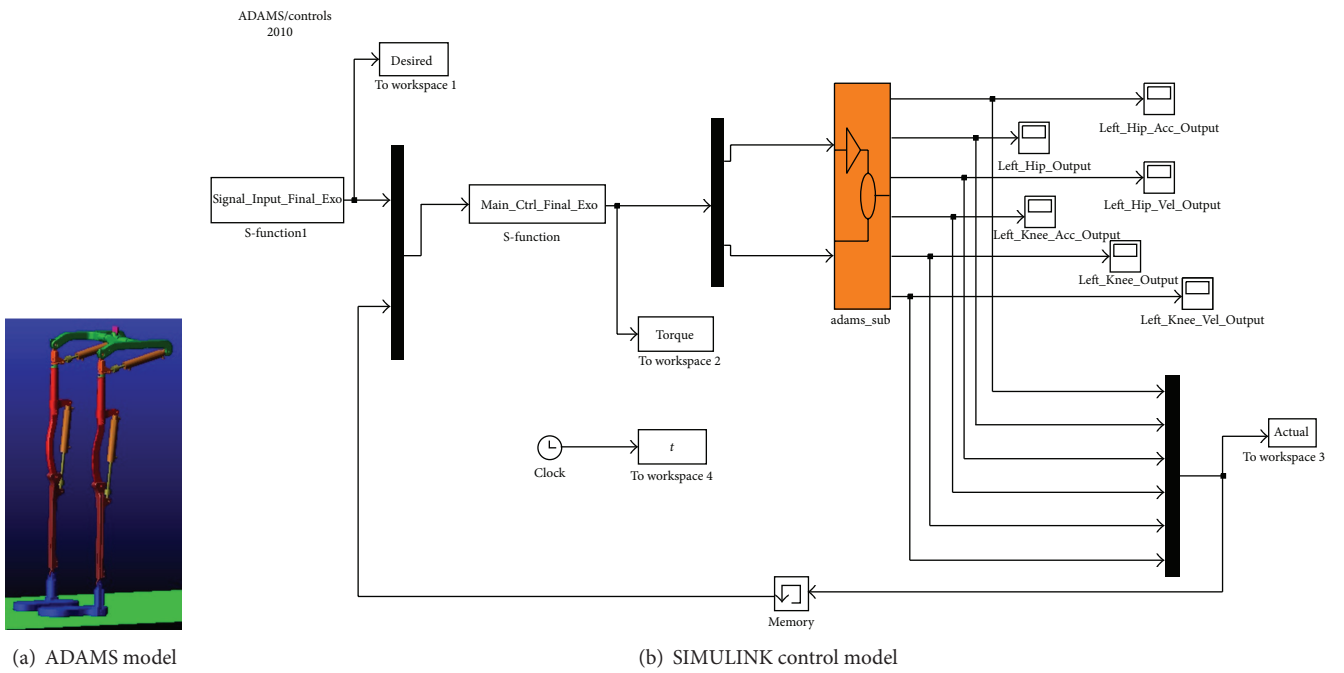


FIGURE 6: Cosimulation using ADAMS and MATLAB for exoskeleton robot.

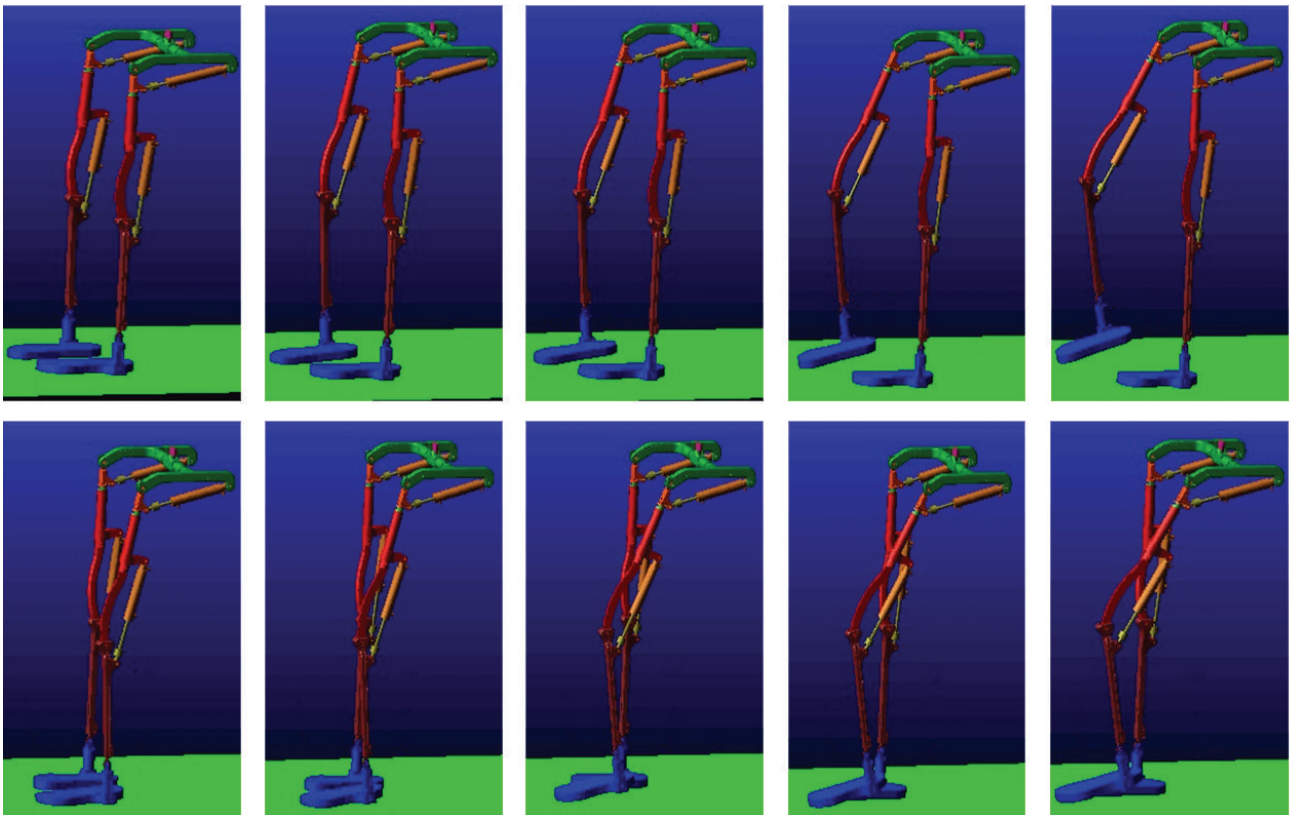


FIGURE 7: ADAMS effect pictures of gait cycles for lower extremity exoskeleton.

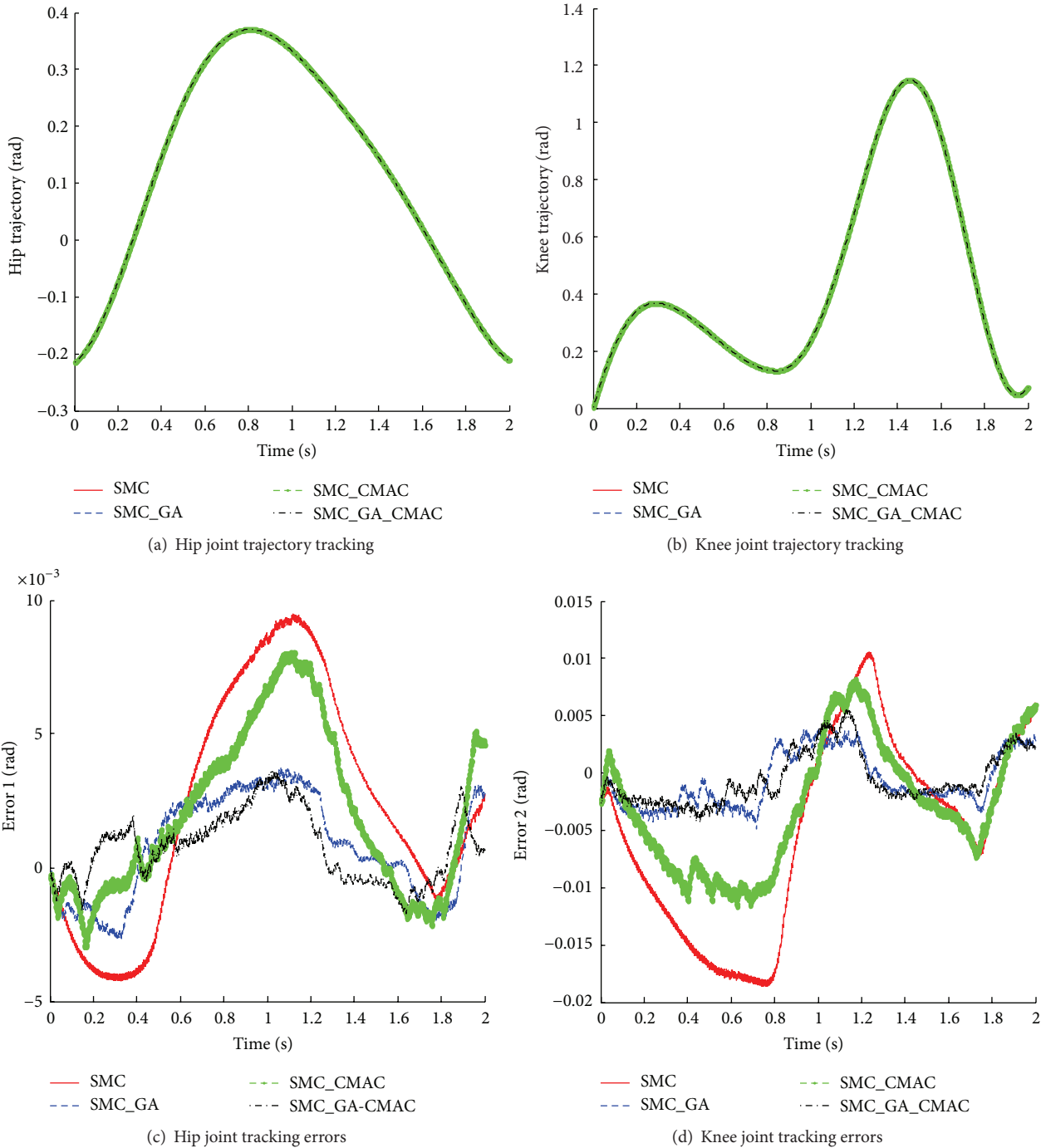


FIGURE 8: The performance comparisons using four methods in Case One.

four kinds of controllers separately. It can be seen that all of controllers can achieve good tracking performance and the conventional SMC without optimization has the largest tracking errors. Similarly, the angular position tracking and tracking errors comparisons in Case Two are depicted in Figures 9(a)–9(d). As Figure 9 shows, the desired joint angular trajectory also can be tracked well. To evaluate the control performances of Case One and Case Two, RSME comparisons using four controllers are depicted in

Figures 10 and 11. Figure 10(a) gives RSME of two joint tracking errors in Case One while Figure 10(b) describes that in Case Two. In two cases, the performance sequence from worse to better should be SMC, SMC\_CMAC, SMC\_GA, and SMC\_GA\_CMAC. Figure 11(a) illustrates the RSME comparison of hip joint while Figure 11(b) illustrates that of knee joint. In Figures 10 and 11, the RSME do not change much; hence the proposed control strategy still works when there exists external disturbance.

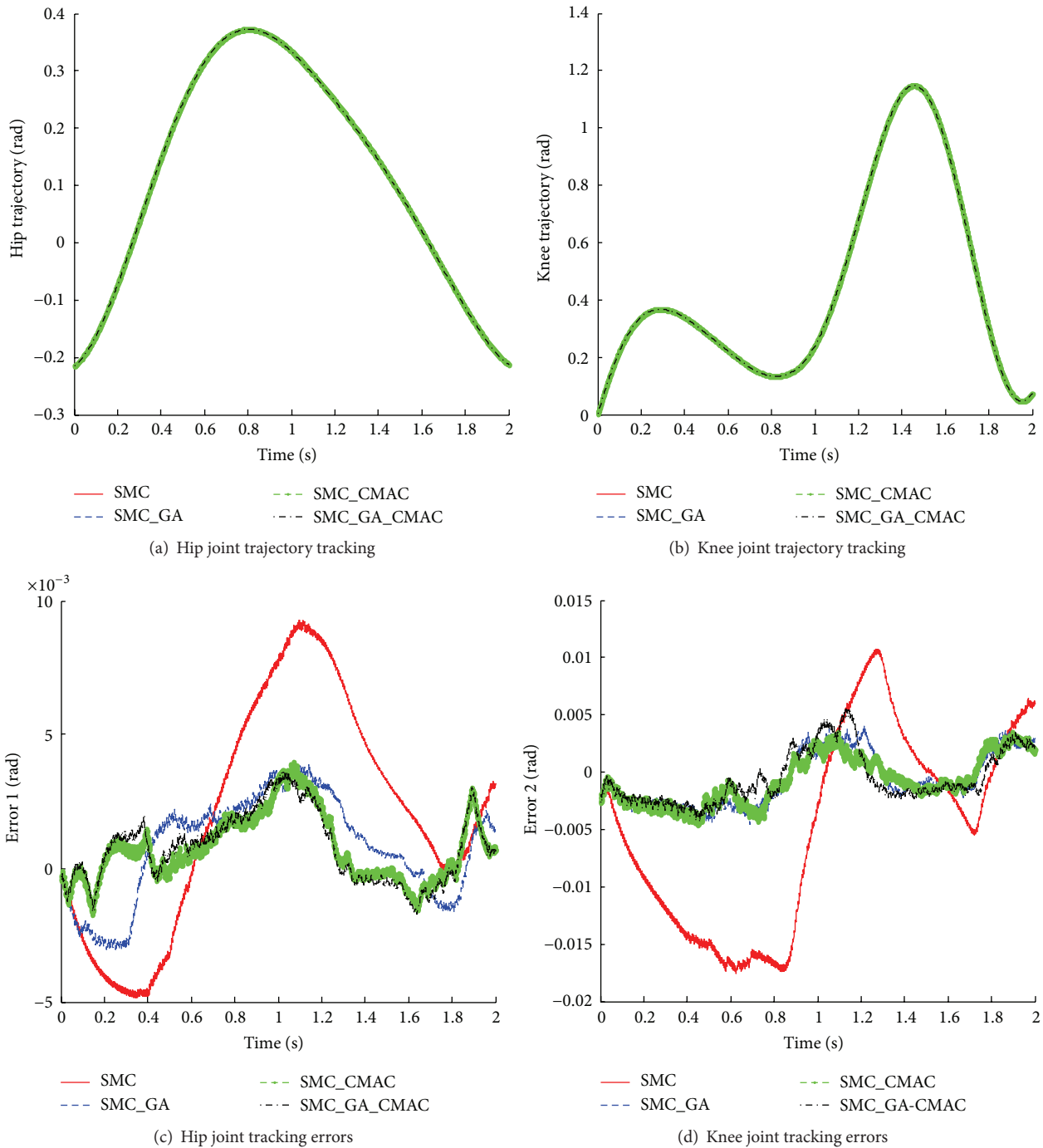


FIGURE 9: The performance comparisons using four methods in Case Two.

If the RSME is treated as a benchmark, the improvement percent (IMP) of performance with four kinds of controllers in Case One and Case Two is displayed in Tables 1 and 2. As the two tables show, the proposed control strategy will gain the highest improvement percentages of 69.4% and 76.8% for hip joint and knee joint separately in Case One while they change to be 68.1% and 76.8% in Case Two. Tables 1 and 2 illustrate that the SMC\_GA is inferior to SMC\_GA\_CMAC but has better performance than SMC\_CMAC, while

the SMC\_CMAC is superior to SMC. Therefore, the proposed control strategy is robust and effective whether the exoskeleton system dynamics suffer from bounded external disturbance or not.

### 5. Conclusions

For lower limb assistive exoskeletons, precise position control is very important for the human-exoskeleton

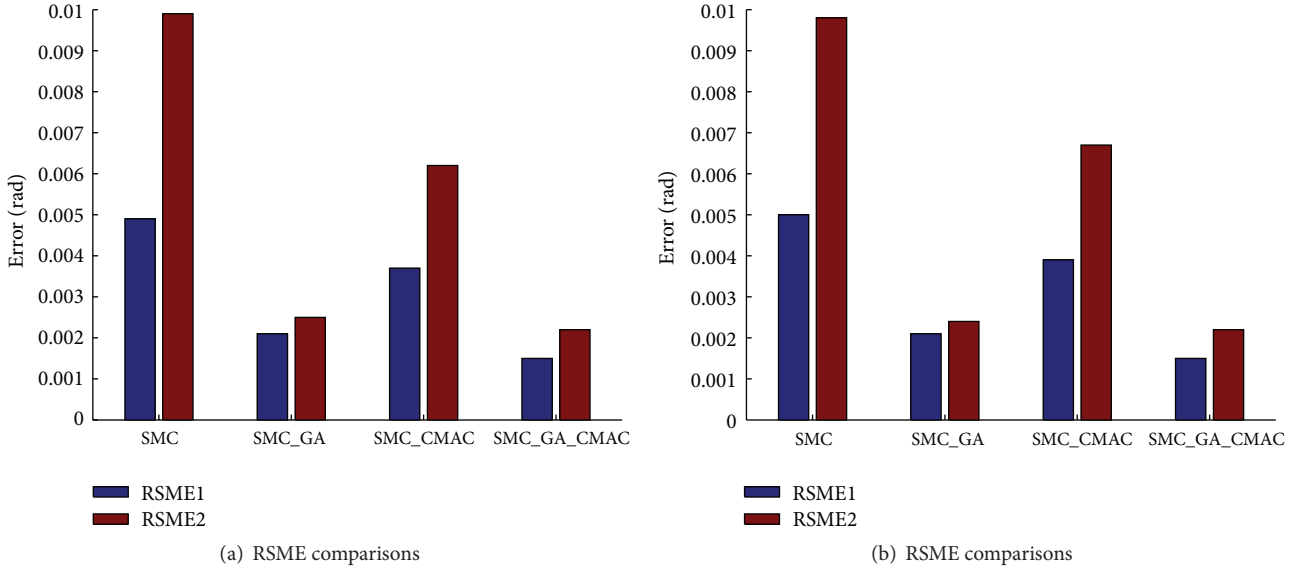


FIGURE 10: RSME comparisons in Case One (without disturbance) and Case Two (with bounded disturbance), respectively. RSME1 is for the hip joint while RSME2 is for the knee joint.

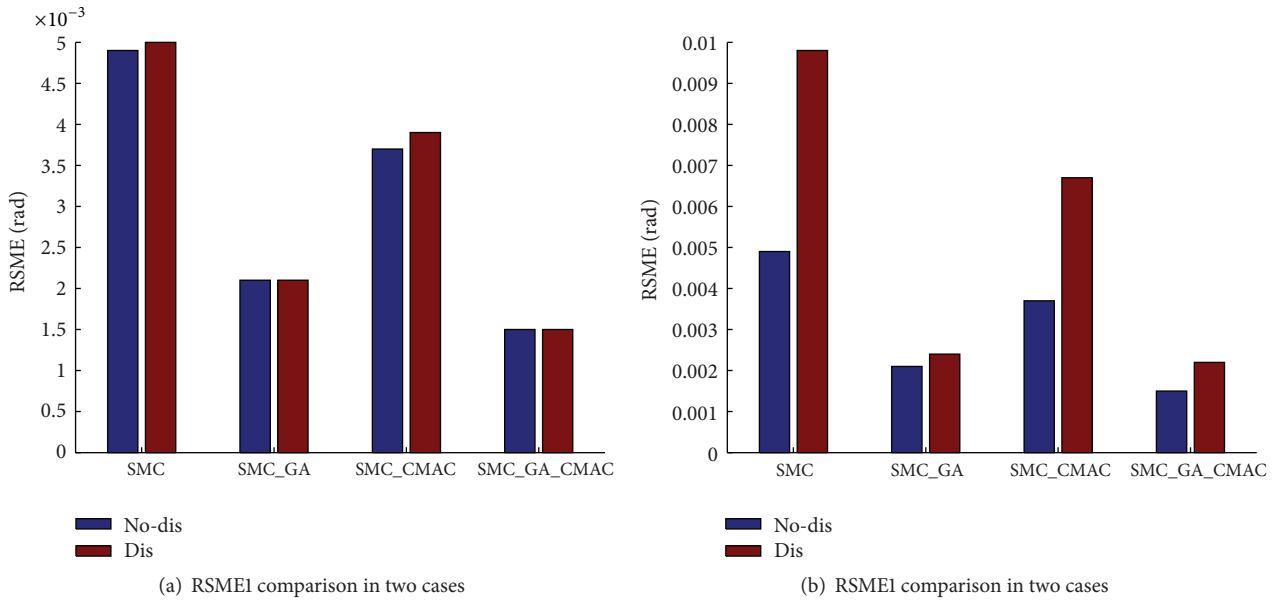


FIGURE 11: RSME1 and RSME2 comparisons in two cases. Icon “No-dis” means Case One and “Dis” means Case Two, respectively.

TABLE 1: Accuracy improvement comparison (Case One).

Control methods	IMP for hip joint (%)	IMP for knee joint (%)
SMC	0	0
SMC_GA	57.1%	74.5%
SMC_CMAC	24.5%	37.4%
SMC_GA_CMAC	69.4%	76.8%

TABLE 2: Accuracy improvement comparison (Case Two).

Control methods	IMP for hip joint (%)	IMP for knee joint (%)
SMC	0	0
SMC_GA	55.3%	75.2%
SMC_CMAC	17.4%	31.7%
SMC_GA_CMAC	68.1%	76.8%

collaboration. In this paper, a hybrid position control strategy SMC\_GA\_CMAC is proposed to follow human limb joints trajectory for the exoskeleton. GA is used to find

the optimal structure of SMC and CMAC neural network is implemented as the compensation to improve tracking performance. The proposed SMC\_GA\_CMAC control

strategy is proven to be stable with Lyapunov function and features better tracking performance compared with SMC, SMC\_GA, and SMC\_CMAC. The proposed control algorithm has guaranteed the requirement for high accuracy of position control for robotic manipulators suffering from dynamics uncertainties. The hybrid control strategy SMC\_GA\_CMAC is more suitable to control the exoskeleton to follow human motion intent under the occurrence of uncertainties. In addition, the proposed method will be investigated and explored in the real exoskeleton prototype in the near future.

Future study will be focused on the optimization of CMAC to overcome its drawbacks because of the binary input mapping character, which can be addressed by intelligent approaches such as fuzzy logic in cosimulation. The human motion intent estimation is also a crucial challenge, which will be investigated using machine learning methods.

## Appendix

### A. SMC Optimization Using GA

See Algorithm 1.

### B. CMAC Neural Network Compensation

See Algorithm 2.

## Competing Interests

The authors declare that they have no competing interests.

## References

- [1] H. Kazerooni, R. Steger, and L. Huang, "Hybrid control of the Berkeley Lower Extremity Exoskeleton (BLEEX)," *International Journal of Robotics Research*, vol. 25, no. 5-6, pp. 561-573, 2006.
- [2] A. Zoss, H. Kazerooni, and A. Chu, "On the mechanical design of the Berkeley Lower Extremity Exoskeleton (BLEEX)," in *Proceedings of the IRS/RSJ International Conference on Intelligent Robots and Systems (IROS '05)*, pp. 3132-3139, August 2005.
- [3] <http://bleex.me.berkeley.edu/research/exoskeleton/hulc/>.
- [4] H. Kawamoto and Y. Sankai, "Power assist method based on Phase Sequence and muscle force condition for HAL," *Advanced Robotics*, vol. 19, no. 7, pp. 717-734, 2005.
- [5] A. Zelinsky, "Robot suit hybrid assistive limb," *IEEE Robotics and Automation Magazine*, vol. 16, no. 4, pp. 98-102, 2009.
- [6] S. Maeshima, A. Osawa, D. Nishio et al., "Efficacy of a hybrid assistive limb in post-stroke hemiplegic patients: a preliminary report," *BMC Neurology*, vol. 11, no. 1, article 116, 6 pages, 2011.
- [7] S. Yu, C. Han, and I. Cho, "Design considerations of a lower limb exoskeleton system to assist walking and load-carrying of infantry soldiers," *Applied Bionics & Biomechanics*, vol. 11, no. 3, pp. 119-134, 2014.
- [8] J. C. Moreno, F. Brunetti, E. Navarro, A. Forner-Cordero, and J. L. Pons, "Analysis of the human interaction with a wearable lower-limb exoskeleton," *Applied Bionics & Biomechanics*, vol. 6, no. 2, pp. 245-256, 2009.
- [9] M. H. Rahman, M. Saad, J.-P. Kenné, and P. S. Archambault, "Control of an exoskeleton robot arm with sliding mode exponential reaching law," *International Journal of Control, Automation and Systems*, vol. 11, no. 1, pp. 92-104, 2013.
- [10] X. T. Tran and H. J. Kang, "Adaptive hybrid high-order terminal sliding mode control of MIMO uncertain nonlinear systems and its application to robot manipulators," *International Journal of Precision Engineering and Manufacturing*, vol. 16, no. 2, pp. 255-266, 2015.
- [11] T. Hsiao and M.-C. Weng, "Robust joint position feedback control of robot manipulators," *Journal of Dynamic Systems, Measurement and Control*, vol. 135, no. 3, Article ID 031010, pp. 815-826, 2013.
- [12] H. G. Sage, M. F. de Mathelin, and E. Ostertag, "Robust control of robot manipulators: a survey," *International Journal of Control*, vol. 72, no. 16, pp. 1498-1522, 1999.
- [13] H. C. Cho, M. S. Fadali, K. S. Lee, and N. H. Kim, "Adaptive position and trajectory control of autonomous mobile robot systems with random friction," *IET Control Theory & Applications*, vol. 4, no. 12, pp. 2733-2742, 2010.
- [14] S. A. M. Dehghan, M. Danesh, and F. Sheikholeslam, "Adaptive hybrid force/position control of robot manipulators using an adaptive force estimator in the presence of parametric uncertainty," *Advanced Robotics*, vol. 29, no. 4, pp. 209-223, 2015.
- [15] R.-J. Wai, Y.-C. Huang, Z.-W. Yang, and C.-Y. Shih, "Adaptive fuzzy-neural-network velocity sensorless control for robot manipulator position tracking," *IET Control Theory & Applications*, vol. 4, no. 6, pp. 1079-1093, 2010.
- [16] J. Y. Cheong, S. I. Han, and J. M. Lee, "Adaptive fuzzy dynamic surface sliding mode position control for a robot manipulator with friction and deadzone," *Mathematical Problems in Engineering*, vol. 2013, Article ID 161325, 15 pages, 2013.
- [17] V. Utkin, J. Guldner, and J. Shi, *Sliding Mode Control in Electromechanical Systems*, CRC Press, New York, NY, USA, 2009.
- [18] F. G. Rossomando, C. Soria, and R. Carelli, "Sliding mode neuro adaptive control in trajectory tracking for mobile robots," *Journal of Intelligent & Robotic Systems*, vol. 74, no. 3-4, pp. 931-944, 2014.
- [19] M. Taherkhorsandi, M. J. Mahmoodabadi, M. Talebipour, and K. K. Castillo-Villar, "Pareto design of an adaptive robust hybrid of PID and sliding control for a biped robot via genetic algorithm optimization," *Nonlinear Dynamics*, vol. 79, no. 1, pp. 251-263, 2014.
- [20] B. S. K. K. Ibrahim, R. Ngadengon, and M. N. Ahmad, "Genetic algorithm optimized integral sliding mode control of a direct drive robot arm," in *Proceedings of the International Conference on Control, Automation and Information Sciences (ICCAIS '12)*, pp. 328-333, Ho Chi Minh City, Vietnam, November 2012.
- [21] M. R. Soltanpour and M. H. Khooban, "A particle swarm optimization approach for fuzzy sliding mode control for tracking the robot manipulator," *Nonlinear Dynamics*, vol. 74, no. 1-2, pp. 467-478, 2013.
- [22] Y.-H. Chang, C.-W. Chang, C.-W. Tao, H.-W. Lin, and J.-S. Taur, "Fuzzy sliding-mode control for ball and beam system with fuzzy ant colony optimization," *Expert Systems with Applications*, vol. 39, no. 3, pp. 3624-3633, 2012.
- [23] C. Su, G. Lii, and H. Hwung, "Position control employing fuzzy-sliding mode and genetic algorithms with a modified evolutionary direction operator," *International Journal of Cybernetics & Systems*, vol. 30, pp. 873-891, 2010.
- [24] E. Fuchs and M. A. S. Masoum, *Power Quality in Power Systems and Electrical Machines*, Academic Press, New York, NY, USA, 2011.

- [25] S. J. Got, M. C. Lee, and M. K. Park, "Fuzzy-sliding mode control of a polishing robot based on genetic algorithm," *Journal of Mechanical Science & Technology*, vol. 15, pp. 580–591, 2001.
- [26] M. J. Kharaajoo and H. Rouhani, *Advances in Artificial Intelligence*, Springer, Berlin, Germany, 2004.
- [27] M. J. Mahmoodabadi, M. Taherkhorsandi, M. Talebipour, and K. K. Castillo-Villar, "Adaptive robust PID control subject to supervisory decoupled sliding mode control based upon genetic algorithm optimization," *Transactions of the Institute of Measurement & Control*, vol. 37, no. 4, pp. 505–514, 2015.
- [28] A. R. Firdaus and A. S. Rahman, "Genetic algorithm of sliding mode control design for manipulator robot," *Telecommunication Computing Electronics and Control*, vol. 10, pp. 645–654, 2012.
- [29] J. S. Albus, "A new approach to manipulator control: the cerebellar model articulation controller (CMAC)," *Journal of Dynamic Systems, Measurement, and Control*, vol. 97, pp. 220–227, 1975.
- [30] W. Yu, M. A. Moreno-Armendariz, and F. O. Rodriguez, "Stable adaptive compensation with fuzzy CMAC for an overhead crane," *Information Sciences*, vol. 181, no. 21, pp. 4895–4907, 2011.
- [31] H. Duan and D. Gu, "Sliding mode adaptive control for flying robot based on recurrent CMAC algorithm," in *Proceedings of the IEEE International Conference on Mechatronics and Automation (ICMA '11)*, pp. 440–445, Beijing, China, August 2011.
- [32] A. Chu, *Design of the Berkley lower extremity exoskeleton (BLEEX) [Ph.D. thesis]*, University of California, Berkeley, Calif, USA, 2005.
- [33] C. Kirtley, CGA Normative Gait Database, <http://www.clinical-gaitanalysis.com/data/>.
- [34] M. W. Spong, S. Hutchinson, and M. Vidyasagar, *Robot Modeling and Control*, John Wiley & Sons, New York, NY, USA, 2006.
- [35] J.-H. Lee, "Highly robust position control of BLDDSM using an improved integral variable structure systems," *Automatica*, vol. 42, no. 6, pp. 929–935, 2006.
- [36] J. J. Slotine and W. Li, *Applied Nonlinear Control*, Prentice-Hall, Englewood Cliffs, NJ, USA, 1991.
- [37] Y. Long and X.-J. Yang, "Robust adaptive fuzzy sliding mode synchronous control for a planar redundantly actuated parallel manipulator," in *Proceedings of the IEEE International Conference on Robotics and Biomimetics (ROBIO '12)*, pp. 2264–2269, Guangzhou, China, December 2012.
- [38] M. Krstic, I. Kanellakopoulos, and P. V. Kokotovic, *Nonlinear and Adaptive Control Design*, John Wiley & Sons, New York, NY, USA, 1995.
- [39] E. Köse, K. Abacı, H. Kızmaz, S. Aksoy, and M. A. Yalçın, "Sliding mode control based on genetic algorithm for WSCC systems include of SVC," *Electronics and Electrical Engineering*, vol. 19, no. 4, pp. 25–28, 2013.
- [40] M. Mitchell, *An Introduction to Genetic Algorithms*, MIT Press, Cambridge, Mass, USA, 5th edition, 1999.
- [41] G. Horváth, "Kernel CMAC: an efficient neural network for classification and regression," *Acta Polytechnica Hungarica*, vol. 3, no. 1, pp. 5–20, 2006.
- [42] X. J. Yang and Y. Long, "Synchronous trajectory tracking control and simulation of CMAC neural network based on computed torque control," *Journal of Harbin Institute of Technology*, vol. 45, no. 7, pp. 85–89, 2013.
- [43] W. T. Miller III, R. P. Hewes, F. H. Glanz, and L. G. Kraft, "Real-time dynamic control of an industrial manipulator using a neural network-based learning controller," *IEEE Transactions on Robotics and Automation*, vol. 6, no. 1, pp. 1–9, 1990.
- [44] F.-C. Chen and C.-H. Chang, "Practical stability issues in CMAC neural network control systems," *IEEE Transactions on Control Systems Technology*, vol. 4, no. 1, pp. 86–91, 1996.
- [45] K. Mohajeri, G. Pishehvar, and M. Seifi, "CMAC neural networks structures," in *Proceedings of the IEEE International Symposium on Computational Intelligence in Robotics and Automation (CIRA '09)*, pp. 39–45, Daejeon, Republic of Korea, December 2009.

## Research Article

# Kinematics and Mechanical Properties of Knees following Patellar Replacing and Patellar Retaining Total Knee Arthroplasty

Rongying Huang, Yanqiang Liu, and Jun Zhu

*School of Mechanical Engineering and Automation, Beihang University, Beijing 100191, China*

Correspondence should be addressed to Yanqiang Liu; [liuyanqiang@buaa.edu.cn](mailto:liuyanqiang@buaa.edu.cn)

Received 2 August 2015; Revised 9 November 2015; Accepted 10 November 2015

Academic Editor: Fan Gao

Copyright © 2015 Rongying Huang et al. This is an open access article distributed under the Creative Commons Attribution License, which permits unrestricted use, distribution, and reproduction in any medium, provided the original work is properly cited.

Knee injury is a common medical issue. A full understanding of the kinematics and mechanical properties of knees following total knee arthroplasty (TKA) repair utilizing patellar replacement (only the base of the patella is replaced) versus patellar retaining surgical techniques is still lacking. In the current paper, we investigated magnetic resonance (MR) imaging data from knees repaired by these two methods and evaluated total knee models created using imaging reconstruction technology that simulated gait conditions. Results revealed that patellar replacement had little influence on tibiofemoral kinematics, although the tibia-surface equivalent stress increased slightly. By contrast, patellar replacement had a significant influence on the patellofemoral joint; patellar internal rotation, external rotation, and medial-lateral translation were all increased. Moreover, the stress distribution on patellar prostheses was altered, resulting in an increased surface maximal equivalent stress on the corresponding area. Moreover, during the gait cycle, we found that the area with maximal equivalent stress shifted its position. Finally, the patellofemoral joint showed decreased motion stability. From the view of kinematics and mechanics, this paper suggests that patella should be retained during TKA if it is possible. The present study presented approaches and technologies for evaluating kinematics and mechanical properties of total knee joint after TKA under gait loads.

## 1. Introduction

As a major supporting joint of human movement, the knee is prone to damage. Ultimately, the best treatment method for repairing knee articular surface damage is total knee arthroplasty (TKA), which replaces the articular surface with knee prosthesis, thereby restoring knee joint functions. With the constant improvement in knee surgery techniques and the demanding requirements of joint prostheses to accurately mimic the knee function, the problems concerning knee kinematics under gait dynamic loading and contact properties following TKA have come under close scrutiny.

For instance, in 2002, Godest et al. [1] first introduced the finite element method and studied the mechanical properties of femoral and tibial implants under gait loads in TKA knees. Subsequently, in 2005, Halloran et al. [2] conducted finite element analyses of knees following TKA, the results

of which closely predicted the results from a concurrent experimental study. In 2007, Knight et al. [3] extended the application of finite element method to biomechanical issues by investigating implant wear following TKA. As such, in 2012, Wachowski et al. [4] examined the effects of knee prostheses with roll back characteristics on patellofemoral joint forces and showed that the prosthesis alleviated joint pain in TKA patients and elongated the service life of the prosthetic. On a similar note, in 2011, Walker et al. [5] established criteria for evaluating knee prosthesis through studying the kinematics of three different knee prostheses.

The knee joint is a very complex structure. The complicated coupling and coordinating relationship between the tibiofemoral and patellofemoral joints during movement/gait makes it difficult to study the kinematics and mechanical characteristics of TKA-repaired knees under dynamic gait loading conditions. In this study, we analyzed and compared

the total knee joint kinematics and mechanical properties during gait cycle following patellar replacement versus patellar retaining TKA. Then the influence of patellar replacement and patellar retaining TKA on total knee functions was assessed. The research steps include knee joint modeling, mechanical simulation of patellar retaining or replacement PS-type prostheses under dynamic gait loads, and the comparison of tibiofemoral and patellofemoral kinematics and contact stresses of knees with PS-type prostheses. The results of this study will provide novel techniques and methods for evaluating the effects of replacement surgery on knee kinematics and mechanical properties.

## 2. Methods

*2.1. TKA Knee Joint Modeling.* The knee joint model contained two parts.

(1) *PS Prosthesis Modeling.* The PS prosthesis was provided by Beijing Chunlizhengda Medical Apparatus Inc. A MicroScribe G2 three-dimensional scanner was employed to scan every structure of the total knee prosthesis to obtain geometry, which was then imported into Geomagic Studio 8.0 for further optimization and also into Solidworks for model repair simplification and reconstruction.

(2) *Knee Modeling after TKA.* Following TKA, the knee model consisted of either a patellar retaining or PS prosthesis replacing knee joint model. Initially, a normal knee joint model was created based on CT and MR data of the normal knee. Subsequently, the femur and tibia were cut according to the surgery procedure [6]. Finally, the remaining femur, tibia, and PS prostheses were assembled to create the total knee model. The normal knee joint MR data was acquired by scanning a student volunteer under the supervision of a doctor.

*2.2. Total Knee Model after TKA.* The simulation of the total knee joint after TKA consisted primarily of model simplification, finite element modeling, and definition of dynamic gait loading.

(1) *Knee Model Simplification.* According to [7–11], the ligaments (anterior cruciate (ACL), posterior cruciate (PCL), medial collateral (MCL), and lateral collateral (LCL)) and surrounding muscles were represented by springs; specifically, the quadriceps femoris and patellar ligament were represented by 2 bundles of spring elements with stiffness coefficients of 2000 N/mm and 1142 N/mm, respectively. The MCL was represented by three bundles of spring elements (i.e., anterior bundle, deep bundle, and oblique bundle), while the LCL was comprised of a single bundle of nonlinear spring elements. The medial/lateral springs' stiffness coefficients and deformations were from [9–11] and shown in Table 1.

(2) *Total Knee Finite Element Model.* The finite element model was created by using ABAQUS 6.11 [5, 10–14], including the definition of material properties, connection relation, boundary conditions and constraints, and grid generation.

TABLE 1: The stiffness coefficients of MCL and LCL.

Ligament	$K_1$	$K_2$
MCL anterior bundle	10	91.25
MCL deep bundle	5	21.07
MCL oblique bundle	5	27.86
LCL	10	72.11

The bone tissue is simplified as isotropic linear elastic material with the elastic modulus of 17 GPa and Poisson's ratio of 0.3. Femoral prosthesis is cobalt-molybdenum alloy with the elastic modulus of 79 GPa and Poisson's ratio of 0.3. The tibial tray prosthesis is titanium alloy with the elastic modulus of 70 GPa and Poisson's ratio of 0.3. The UHMWPE (ultra-high-molecular-weight polyethylene) tibial insert and the patellar prosthesis use nonlinear elastoplastic deformable material properties.

Different coupling relationship between the components of the knee prosthesis is defined. The relationships between the femoral prosthesis and the femoral condyle section, tibial prosthesis and tibial section, and tibial prosthesis and tibial liner are defined as consolidation. The contacts between the femoral prosthesis and polyethylene insert, patella cartilage, and femoral prosthesis were defined as sliding friction, with a friction coefficient of 0.004 [1, 2, 9].

The definition of the boundary conditions and constraints is as follows: the patella is not limited, the movement of femoral with prosthesis is limited to flexion and extension, the tibial with prosthesis is only limited with the outer flexion and extension, and turning and shift movement on the other directions are not limited.

C3D10 tetrahedron grid elements were employed to achieve free mesh generation, and the models of patella retaining and replacement TKA were divided into 81052 and 78397 elements, respectively. The total knee after TKA and the corresponding finite element models are shown in Figure 1.

(3) *Applying Dynamic Loading.* There were three main processes utilized when the gait dynamic loads were applied.

- (1) According to the standard ISO 14243-1, the gait cycles were divided into four main states [12, 13, 15–19]: heel strike (HS), single limb stance 1 (SLS1), single limb stance 2 (SLS2), and toe off (TO). The gait loading curve was also divided into four areas (as shown in Figure 2) to analyze the movement and mechanical characteristics of the human gait cycle after TKA.
- (2) The loading curve was transferred into discrete data by using piecewise polynomial fitting techniques to actualize the human knee gait cycle motion simulation of dynamic loading after TKA. The gait flexion and gait load were controlled by fitting functions programmed with Matlab, including gait flexion function, axial force loading function, anteroposterior force loading function, and the internal and external rotation torque loading function.
- (3) A gait dynamic load was applied to the total knee after TKA. The line connecting the rotational centers

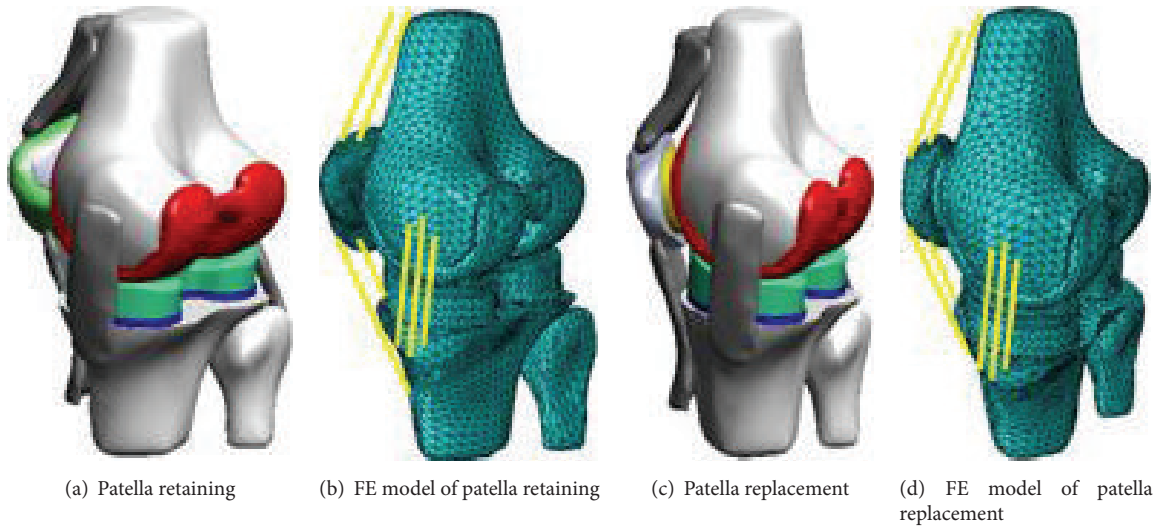


FIGURE 1: 3D and FE model following TKA with prosthesis.

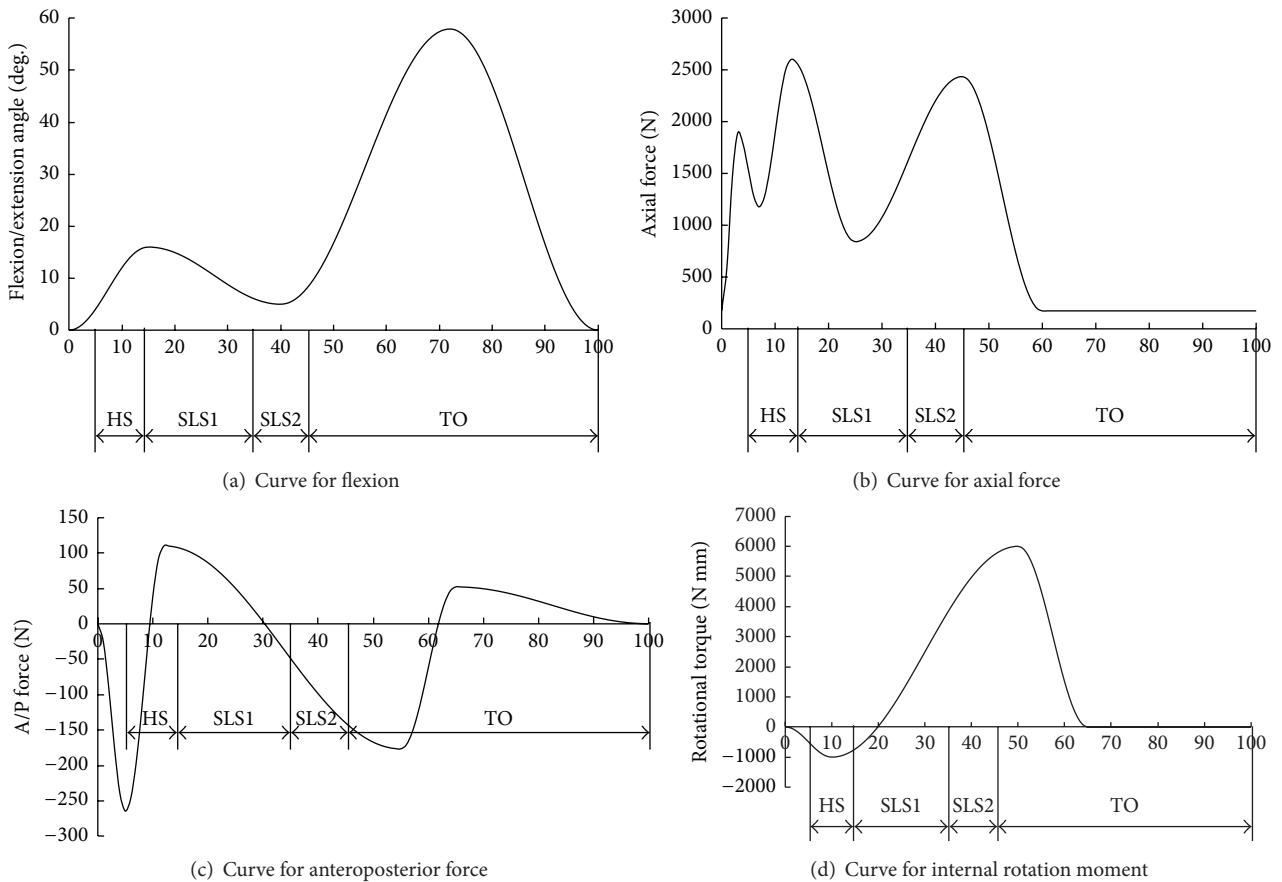


FIGURE 2: The distribution of gait loading curves during gait cycle.

of the femoral lateral and medial epicondyles was defined as the axis for femur flexion (Figure 2(a)), and axis force was applied to the centers of each of the femoral lateral and medial epicondyles based on the axis force loading function (Figure 2(b)), where

60% axis force was applied to the center of the medial epicondyle and 40% axis force was applied to the lateral epicondyle [20]. The anteroposterior force (Figure 2(c)) and internal rotation moment (Figure 2(d)) were applied to the tibia implant based

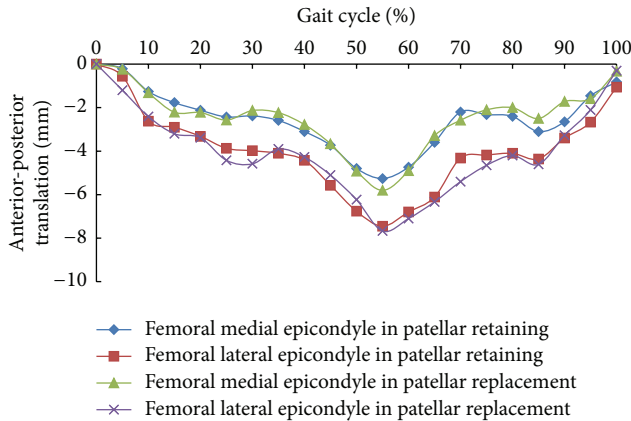


FIGURE 3: Anterior-posterior translation of femoral lateral and medial epicondyles during the gait cycle.

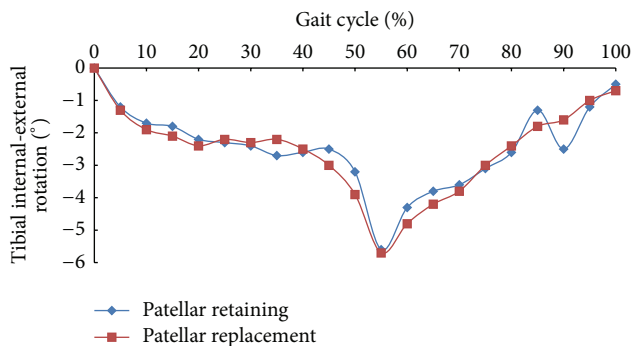


FIGURE 4: Tibial internal-external rotation for patellar retaining and replacement models.

on the anteroposterior force function and internal-external rotation function. All the  $x$ -axes of Figures 2(a)–2(d) are percentage of gait cycle time.

**2.3. Dynamic Simulation of the Total Knee with Patellar Retaining and Replacement under Gait Loading.** The dynamic simulation of the total knee with patellar retaining and replacement during gait loading was performed in ABAQUS 6.11 by means of explicit dynamic finite element analyses. The data were collected at a 5% gait cycle interval. The effects of the patellar treatment method on joint function were analyzed by comparing the equivalent contact stress value on the articular surface and motion characteristics of the tibiofemoral joint and patellofemoral joint.

### 3. Results

#### 3.1. Kinematics of Total Knee Joint after Patellar Retaining and Replacement TKA

**3.1.1. Kinematics of the Tibiofemoral Joint under Gait Loads.** The relative movement curves of the tibiofemoral joint from simulation results of both models are shown in Figures 3 and 4. Results revealed that both patellar retaining and patellar

replacement had little influence on femoral anteroposterior translation. Similar value and tendency could be observed for the two models in terms of anteroposterior translation of the medial and lateral epicondyle center. During the entire gait cycle, both the lateral and medial femoral epicondyle translated posteriorly, peaking at about 55% of the gait cycle. For the patellar retaining model, the posterior translations of the femoral lateral and medial epicondyles were 5.3 mm and 7.5 mm, respectively, while in the patellar replacement model, the values were 5.8 mm and 7.7 mm, respectively. These results are similar to that found previously by Halloran et al. [2] who reported a maximal posterior translation of 5.1 mm at 60% of gait cycle.

For both models, both the tibial internal and external rotations and variations thereof showed similar results. At 0%–20% of the gait cycle, the tibia rotated internally by  $2.2^\circ$  and remained stable from 20% to 45% of the gait cycle, peaking at 55% ( $6^\circ$ ), at which point the internal rotation began to gradually decrease. These results are consistent with a previous report [1] that observed a maximal internal rotation of  $5^\circ$ .

The peak femoral posterior translation and tibial internal rotation both occurred at about 55% to 60% of the gait cycle, when the foot was lifted off of the ground and the tibial axis force was small. The body's center of gravity transferred, and the knee joint was subject to a moment of high internal rotation and posterior force.

#### 3.1.2. Kinematics of the Patellofemoral Joint under Gait Loads.

Figure 5 shows the patellofemoral kinematics during the gait cycle for patellar retaining and replacement TKA knees. Patellar replacement TKA significantly increased patellar movements compared to patellar retaining TKA. Moreover, patellar tilting, internal rotation, and medial/lateral translation were all significantly higher. Patellar flexion was unchanged. Therefore, the patellofemoral joint motion stability was decreased following patellar replacement TKA. The patellar flexion variation curve revealed that the tibiofemoral joint flexion variation was slightly greater in the patellar replacement versus the patellar retaining model, with a maximal flexion angle of  $39^\circ$  and  $46.3^\circ$ , respectively, observed at 70% of the gait cycle.

For both models, the second highest and maximal patellar tilting occurred at 20% and 50% of gait cycle, respectively, which were equal to  $1.8^\circ$  and  $4.6^\circ$  for the patellar retaining model and  $2.8^\circ$  and  $8.4^\circ$  for the patellar replacement model. Patellar internal rotation showed a similar tendency as tilting; the second highest and maximal internal rotation at 20% and 55% of gait cycle were  $0.6^\circ$  and  $1.5^\circ$  for the patellar retaining model and  $1^\circ$  and  $2.8^\circ$  for the patellar replacement model.

The patellar lateral-medial translation showed evident differences between the two models, though the variation tendency was similar. The patellar first moved medially to the maximal value and then laterally till the minimal value was achieved before it moved medially to the maximal value once again. The peak, minimal, and maximal values occurred at 20% (1.7 mm), 35% (0.3 mm), and 55% (2.4 mm) of the gait cycle, respectively. For the patellar replacement model, the peak, minimal, and maximal values occurred at 15%

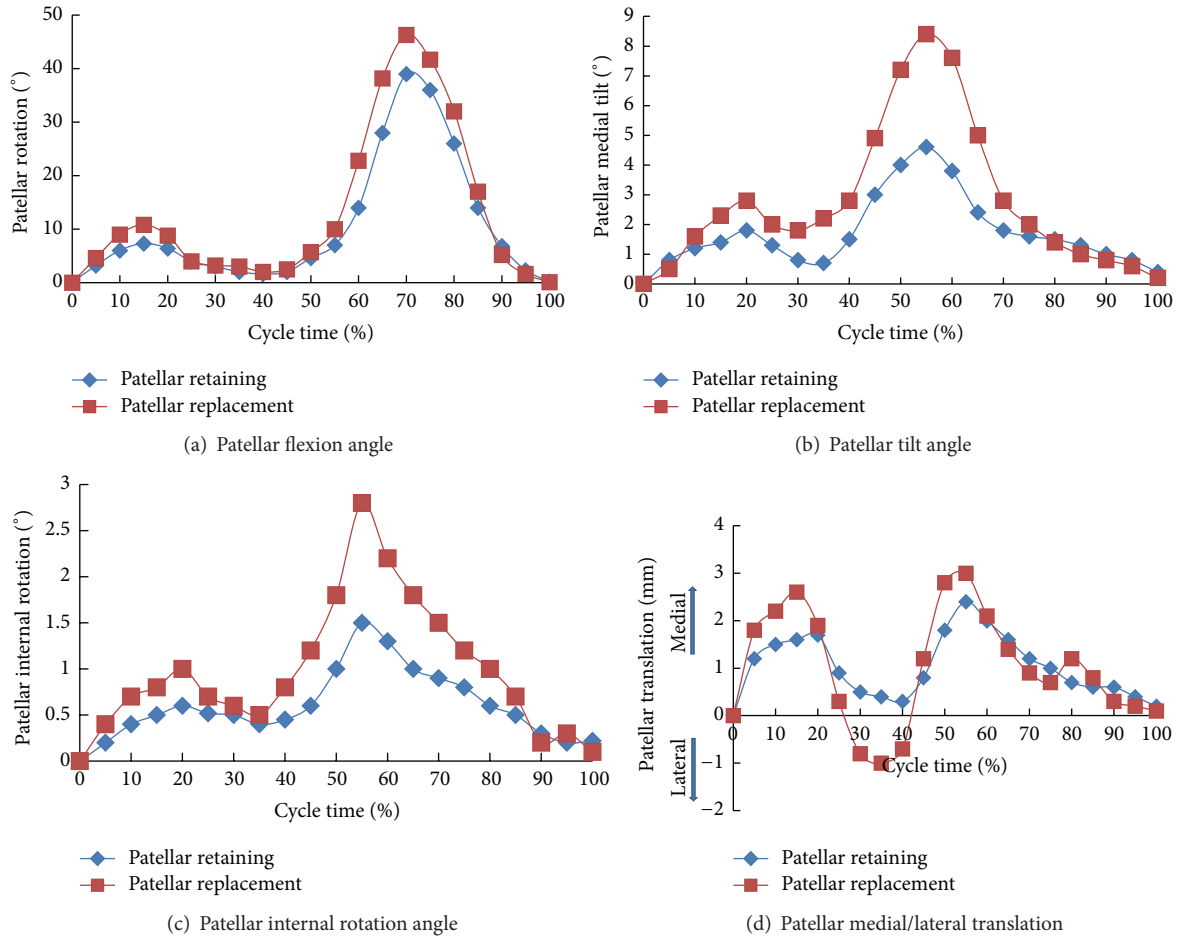


FIGURE 5: Kinematics of the patellofemoral joint.

(2.6 mm), 35% (1 mm), and 55% (3 mm) of the gait cycle, respectively, values significantly higher than those in the patellar retaining model indicating a decreased knee joint stability.

3.2. Mechanical Properties of TKA Knee Joint under Gait Loads

3.2.1. Mechanical Properties of Tibiofemoral Joint under Gait Loads. The mechanical properties of the tibiofemoral joint under gait loads were investigated by analyzing the stress contour and maximal stress variations of the UHMWPE tibial tray during the gait cycle, thereby illustrating the mechanical differences between the tibiofemoral joints of two models.

The stress distributions of the UHMWPE tibial tray were represented by the stress contour at typical states, HS, SLS, and TO (Figure 6). Results revealed that the stress distributions of the two models are similar. During the gait cycle, high stress mainly concentrates on the tibial medial condyle (used dominantly during gait) at SLS2 and TO. In addition, the equivalent stress and equivalent stress area of the lateral condyle slightly increased probably due to the displacement of the center of gravity.

A histogram of the maximal equivalent peak contact stress of the UHMWPE tibial tray during the gait cycle

is shown in Figure 7. Combining Figures 6 and 7, the mechanical properties of the tibial tray are listed in Table 2. Table 2 suggested that although the stress distribution of tibial tray was similar for the two models, patellar replacement resulted in elevated stress, which may aggravate the tibial tray wear.

Figure 8 shows the variation curve of tibial tray contact stress under gait loads. Results show that the two models demonstrated similar variation, peaking at 50% of the gait cycle and gaining a second maximal stress value at 20%. However, the stress was consistently higher in the patellar replacement model than in the patellar retaining model. For both models, during 0%–10% of the gait cycle, the heel strike imposed an increasing tibial axial force. Meanwhile, the tibial tray stress reached 17.1 MPa and 18.6 MPa for internal rotation movement and tibial anterior force, respectively. When the entire foot made contact with the ground the tibial axial force was slightly reduced due to forward body movement. As such, at 30% of the gait cycle the tibial tray contact stresses decreased correspondingly, with values of 13.4 MPa and 14.77 MPa for internal rotation movement and tibial anterior force, respectively. Then, as the foot began to push off of the ground and separation occurred, we found that the axial force increased, reaching maximal contact stress values

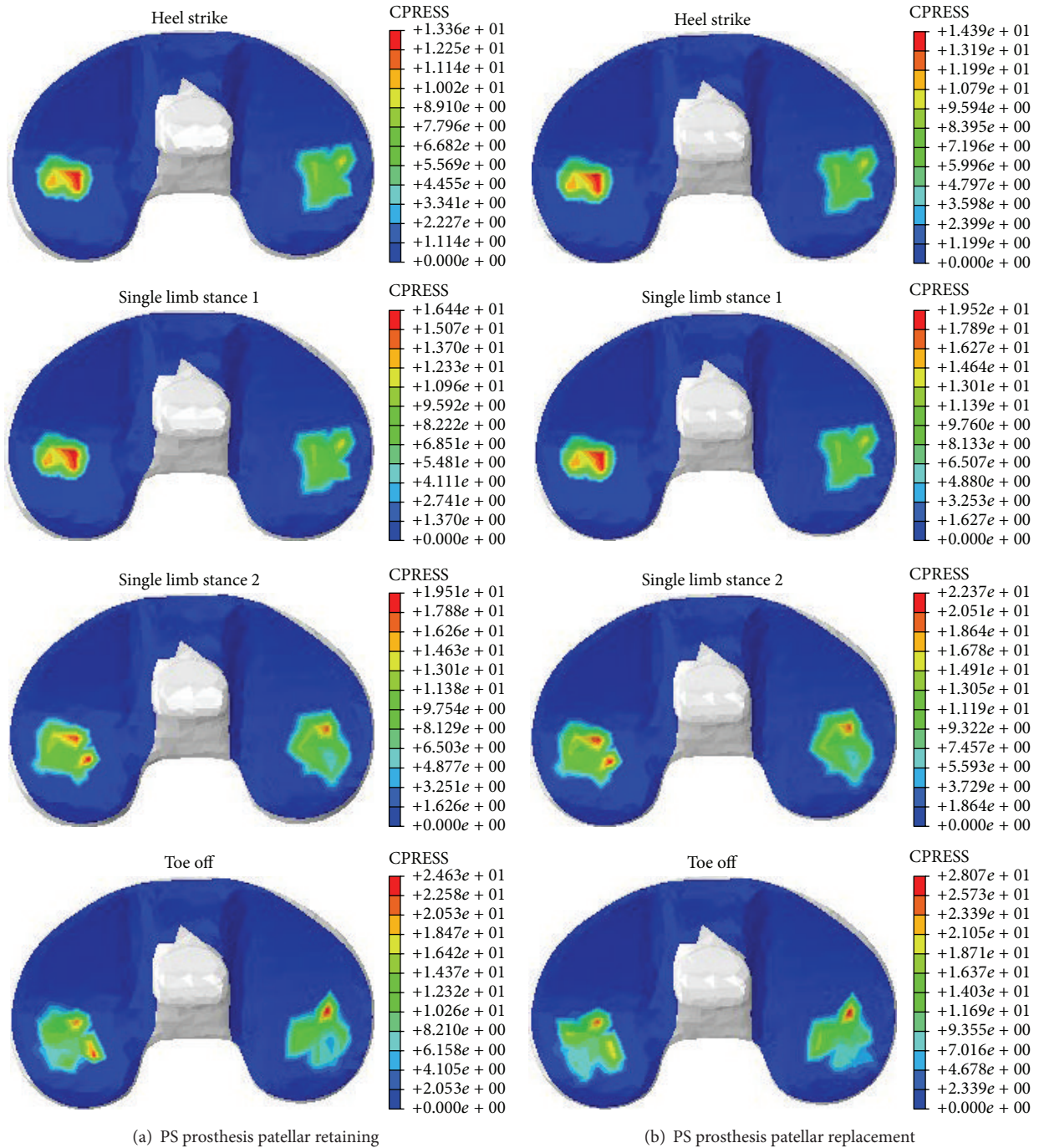


FIGURE 6: Stress contour of tibial tray during gait cycle.

of 26.35 MPa and 29.23 MPa for tibial movement and anterior force, respectively. After the foot lifted from the ground, the tibial axial force and tibial tray contact stress both decreased substantially. Taken together, these results reveal that the variation in the contact stress reflects the changes in the knee supporting force during gait.

**3.2.2. Mechanical Properties of Patellofemoral Joint after TKA.** The mechanical properties of the patellofemoral joint were described by using a surface patellar stress contour,

a histogram of maximal equivalent stress, and a maximal equivalent stress variation curve. Figure 9 shows the stress contours of the patellar surface or patellar prosthesis surface. Considering the fact that the flexion angle can affect the patellar maximal equivalent stress, the toe off state was divided into two states: TO1 and TO2. At TO1, the tibiofemoral flexion angle was  $8^\circ$  and the axial force was 2434 N. Meanwhile, at TO2, when the foot is separated from the ground, the axial force reached 168 N with  $56^\circ$  flexion. It can be seen that compared to patellar retaining TKA, patellar replacement

TABLE 2: Knee tibial tray mechanical properties during the gait cycle.

	Gait cycle (patellar retaining)				Gait cycle (patellar replacement)			
	Heel strike	Single limb stance 1	Single limb stance 2	Toe off	Heel strike	Single limb stance 1	Single limb stance 2	Toe off
Flexion angle	4°	16°	6°	8°	4°	16°	6°	8°
Axial force (N)	1531	2482	1636	2434	1531	2482	1636	2434
Peak contact stress (MPa)	13.36	16.35	19.51	24.63	14.39	19.43	22.37	28.07
Stress increment					7.71%	18.84%	14.66%	13.97%
High stress area	Medial	Medial	Medial and lateral	Medial and lateral	Medial	Medial	Medial and lateral	Medial and lateral

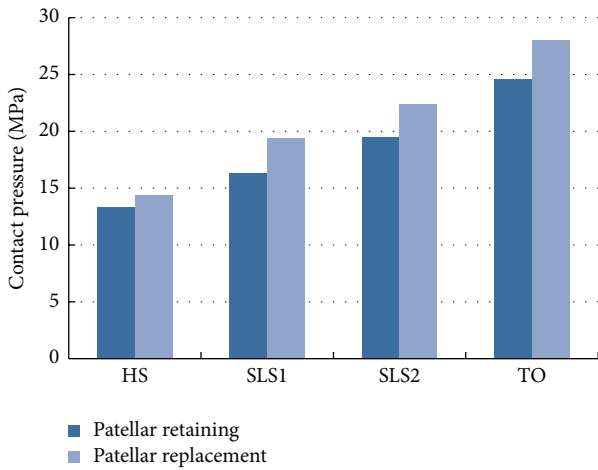


FIGURE 7: Histogram of the maximal contact stress of the UHMWPE tibial tray during the gait cycle.

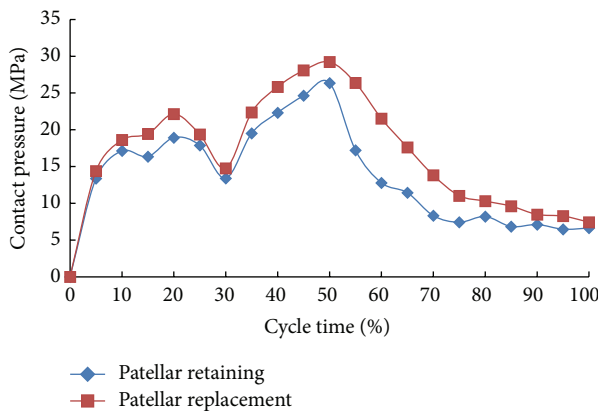


FIGURE 8: Variation in the peak contact stress of the tibial tray during the gait cycle for the patellar retaining versus patellar replacement TKA models.

altered the stress distribution of the patellofemoral joint surface, resulting in an increased peak stress area, a maximal equivalent stress, and a significantly varying peak stress area.

Combining Figures 9 and 10, the stress distribution of the patella and patellar implant was found to be related to the knee axial force and the tibiofemoral flexion angle in addition

to the patellar treatment method. At higher axial force and tibiofemoral joint flexion, an increase in the peak equivalent stress was observed. Following patellar replacement TKA, the patellar implant showed significantly higher peak equivalent stresses, presumably due to changes in the contact surface and a loss of patellar cartilage for protective buffering. Specifically, at HS, the peak equivalent stress was 8.31 MPa and 11.44 MPa for the patellar retaining and patellar replacement model, respectively, an increase of 37.67%. At SLS1, the peak equivalent stress for the two models was 13.67 MPa and 15.41 MPa, respectively, an increase of 12.73%. At SLS2, the values were 9.35 MPa and 12.25 MPa, respectively, an increase of 31.02%. At TO1, the peak equivalent stress was 14.97 MPa and 17.33 MPa, respectively, an increase of 15.75%. Finally, at TO2, the peak equivalent stress was 19.87 MPa and 23.5 MPa, respectively, an increase of 18.27%. These results clearly reveal increased peak equivalent stresses in the patellar replacement model.

It can be seen from Figure 11 that the patella and patellar implant exhibited a similar variation in the peak equivalent stress during the gait cycle. However, the patellar implant stress was significantly higher. At 45% of the gait cycle the foot was separated from the ground, but due to the high tibiofemoral flexion angle the adjustment in the body's center of gravity resulted in an altered joint moment and a peak stress between 55% and 75% of the gait cycle at a time where stresses alter significantly. Then, as the gait cycle proceeded into next one and the center of gravity was successfully transferred, the tibiofemoral flexion angle gradually decreased, thereby resulting in a reduced patellar equivalent stress.

#### 4. Conclusions

In this study, the kinematics and equivalent stress of two knee models (patellar retaining and patellar replacement) were compared during the gait cycle. Results showed the following: (1) patellar replacement has little influence on tibiofemoral kinematics and mechanical properties, although it produced a slightly increased tibial tray stress; (2) patellar replacement significantly reduced the kinematics and mechanical performances in the patellofemoral joint during the gait cycle; patellar tilting, internal rotation, and anterior-posterior translation were all significantly increased compared to the

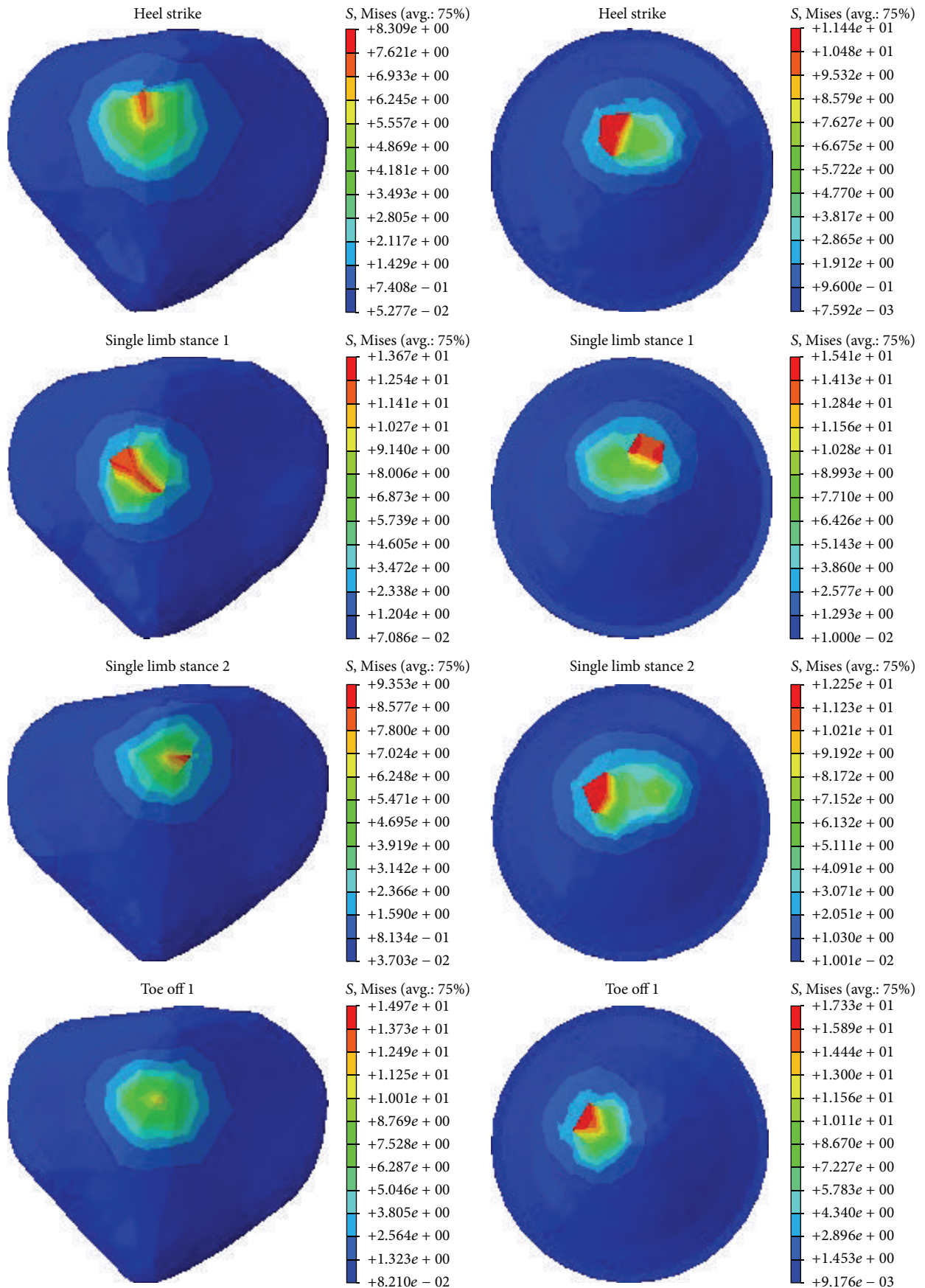


FIGURE 9: Continued.

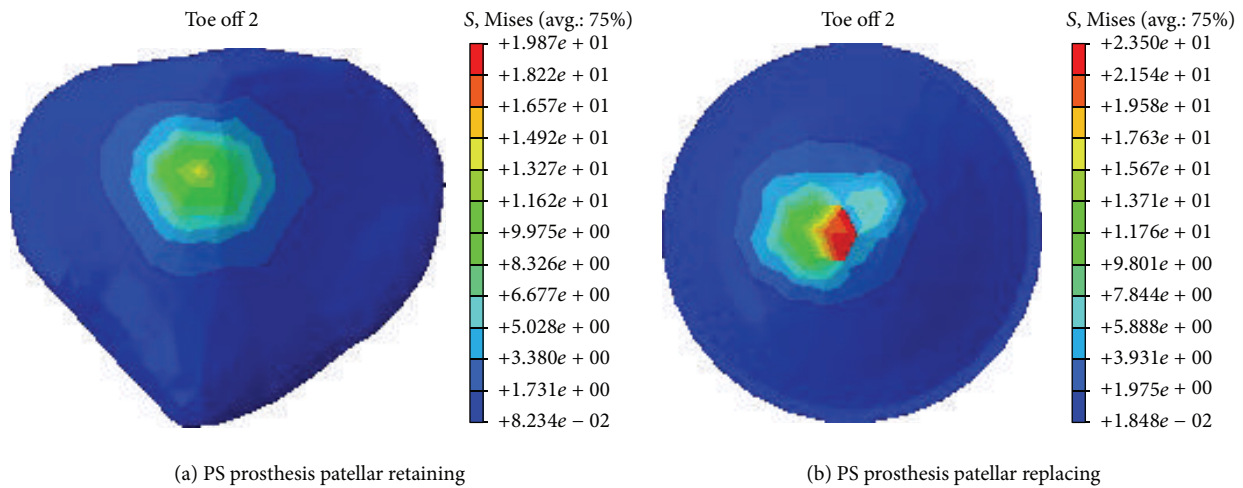


FIGURE 9: Contours of equivalent stress in patella and patellar implants during the gait cycle.

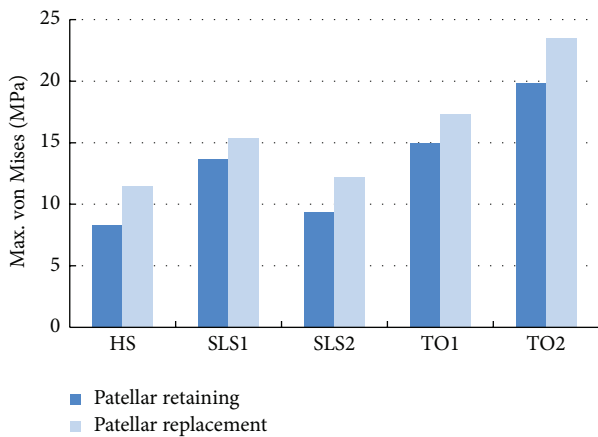


FIGURE 10: Bar diagram of peak equivalent stress of patella and patellar implant during gait cycle.

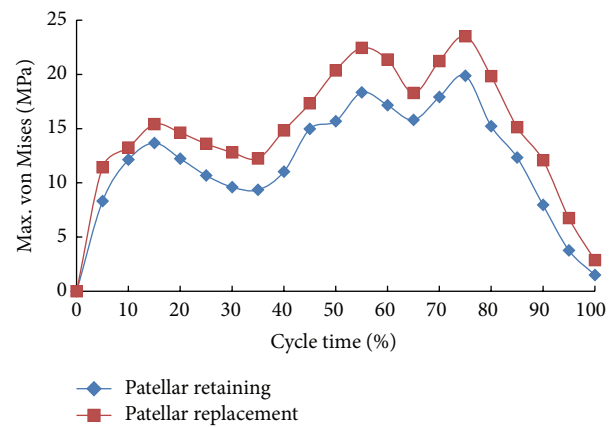


FIGURE 11: Peak equivalent stress curve of patella and patellar implant during gait cycle.

patellar retaining method; meanwhile, patellar replacement altered the stress distribution in the patellofemoral joint, resulting in an increased high-stress area; finally (3) compared to patellar retaining TKA, patellar replacement has less influence both on kinematic variations in the tibiofemoral and patellofemoral joints and on the variations in the joint peak equivalent stress during the gait cycle. In conclusion, TKA was shown to preserve human knee tissue following surgery. Moreover, the results here indicate that the patellar retaining method has more beneficial long-term effects compared to patellar replacement.

But this paper only analyzes the kinematics and mechanics with simplified knee models; this is only part of properties of total knee after TKA surgery. Furthermore, if the result is verified by some experiment, the paper will be more meaningful.

**Conflict of Interests**

The authors declare that there is no conflict of interests regarding the publication of this paper.

**Acknowledgment**

This paper has been supported by NSFC (National Natural Science Foundation of China) funds (Grant no. 50975013).

**References**

- [1] A. C. Godest, M. Beaugonin, E. Haug, M. Taylor, and P. J. Gregson, "Simulation of a knee joint replacement during a gait cycle using explicit finite element analysis," *Journal of Biomechanics*, vol. 35, no. 2, pp. 267–275, 2002.
- [2] J. P. Halloran, A. J. Petrella, and P. J. Rullkoetter, "Explicit finite element modeling of total knee replacement mechanics," *Journal of Biomechanics*, vol. 38, no. 2, pp. 323–331, 2005.
- [3] L. A. Knight, S. Pal, J. C. Coleman et al., "Comparison of long-term numerical and experimental total knee replacement wear during simulated gait loading," *Journal of Biomechanics*, vol. 40, no. 7, pp. 1550–1558, 2007.
- [4] M. M. Wachowski, T. A. Walde, P. Balcarek et al., "Total knee replacement with natural rollback," *Annals of Anatomy*, vol. 194, no. 2, pp. 195–199, 2012.

- [5] P. S. Walker, Y. Heller, D. J. Cleary, and G. Yildirim, "Preclinical evaluation method for total knees designed to restore normal knee mechanics," *The Journal of Arthroplasty*, vol. 26, no. 1, pp. 152–160, 2011.
- [6] M. Marcacci, L. Nofrini, F. Iacono, A. Di Martino, S. Bignozzi, and M. Lo Presti, "A novel computer-assisted surgical technique for revision total knee arthroplasty," *Computers in Biology and Medicine*, vol. 37, no. 12, pp. 1771–1779, 2007.
- [7] P. S. M. Barbour, D. C. Barton, and J. Fisher, "The influence of contact stress on the wear of UHMWPE for total replacement hip prostheses," *Wear*, vol. 181–183, no. 1, pp. 250–257, 1995.
- [8] M. A. Wimmer and T. P. Andriacchi, "Tractive forces during rolling motion of the knee: implications for wear in total knee replacement," *Journal of Biomechanics*, vol. 30, no. 2, pp. 131–137, 1997.
- [9] E. M. Abdel-Rahman and M. S. Hefzy, "Three-dimensional dynamic behaviour of the human knee joint under impact loading," *Medical Engineering and Physics*, vol. 20, no. 4, pp. 276–290, 1998.
- [10] Y.-L. Liu, K.-J. Lin, C.-H. Huang et al., "Anatomic-like polyethylene insert could improve knee kinematics after total knee arthroplasty—a computational assessment," *Clinical Biomechanics*, vol. 26, no. 6, pp. 612–619, 2011.
- [11] Y.-L. Liu, W.-C. Chen, W.-L. Yeh et al., "Mimicking anatomical condylar configuration into knee prosthesis could improve knee kinematics after TKA—a computational simulation," *Clinical Biomechanics*, vol. 27, no. 2, pp. 176–181, 2012.
- [12] P. S. Walker, G. W. Blunn, D. R. Broome et al., "A knee simulating machine for performance evaluation of total knee replacements," *Journal of Biomechanics*, vol. 30, no. 1, pp. 83–89, 1997.
- [13] M. J. M. Ploegmakers, B. Ginsel, H. J. Meijerink et al., "Physical examination and in vivo kinematics in two posterior cruciate ligament retaining total knee arthroplasty designs," *The Knee*, vol. 17, no. 3, pp. 204–209, 2010.
- [14] A. Abdelgaied, F. Liu, C. Brockett, L. Jennings, J. Fisher, and Z. Jin, "Computational wear prediction of artificial knee joints based on a new wear law and formulation," *Journal of Biomechanics*, vol. 44, no. 6, pp. 1108–1116, 2011.
- [15] H. Iwaki, V. Pinskerova, and M. A. R. Freeman, "Tibiofemoral movement 1: the shapes and relative movements of the femur and tibia in the unloaded cadaver knee," *The Journal of Bone and Joint Surgery—British Volume*, vol. 82, no. 8, pp. 1189–1195, 2000.
- [16] P. F. Hill, V. Vedi, A. Williams, H. Iwaki, V. Pinskerova, and M. A. R. Freeman, "Tibiofemoral movement 2: the loaded and unloaded living knee studied by MRI," *The Journal of Bone & Joint Surgery—British Volume*, vol. 82, no. 8, pp. 1196–1198, 2000.
- [17] S. Nakagawa, Y. Kadoya, S. Todo et al., "Tibiofemoral movement 3: full flexion in the living knee studied by MRI," *The Journal of Bone & Joint Surgery—British Volume*, vol. 82, no. 8, pp. 1199–1200, 2000.
- [18] R. Willing and I. Y. Kim, "A holistic numerical model to predict strain hardening and damage of UHMWPE under multiple total knee replacement kinematics and experimental validation," *Journal of Biomechanics*, vol. 42, no. 15, pp. 2520–2527, 2009.
- [19] R. Willing and I. Y. Kim, "Quantifying the competing relationship between durability and kinematics of total knee replacements using multiobjective design optimization and validated computational models," *Journal of Biomechanics*, vol. 45, no. 1, pp. 141–147, 2012.
- [20] D. A. Dennis, M. R. Mahfouz, R. D. Komistek, and W. Hoff, "In vivo determination of normal and anterior cruciate ligament-deficient knee kinematics," *Journal of Biomechanics*, vol. 38, no. 2, pp. 241–253, 2005.